

Log# 01631U

PSI-3031/
TR-970

IFELS PROGRAM
DRAFT FINAL REPORT

Prepared by:

G.A. Simons, Principal Investigator

P.E. Nebolsine, J.C. Person,
D. Resendes, A.W. Bailey, and N.D. Humer
Physical Sciences Inc.
(508) 475-9030

Under Contract No. T-2346(8936)-1308

for the Period
2 May 1989 through 30 September 1989

Sponsored by
U.S. Army Missile Command
"Analysis of Free Electron Laser Effects Data"
Issued by U.S. Army Missile Command Under
Contract No. DAAH01-88-D-0068

Prepared for:

Battelle Columbus Laboratories
505 King Avenue
Columbus, Ohio 43201-2693

October 1989

UNCLASSIFIED

SECURITY CLASSIFICATION OF THIS PAGE

REPORT DOCUMENTATION PAGE

1a. REPORT SECURITY CLASSIFICATION UNCLASSIFIED			1b. RESTRICTIVE MARKINGS N/A		
2a. SECURITY CLASSIFICATION AUTHORITY N/A since Unclassified			3. DISTRIBUTION/AVAILABILITY OF REPORT Unclassified/Unlimited		
2b. DECLASSIFICATION/DOWNGRADING SCHEDULE N/A since Unclassified					
4. PERFORMING ORGANIZATION REPORT NUMBER(S) PSI-3031/TR-970			5. MONITORING ORGANIZATION REPORT NUMBER(S)		
6a. NAME OF PERFORMING ORGANIZATION Physical Sciences Inc.		6b. OFFICE SYMBOL (if applicable)	7a. NAME OF MONITORING ORGANIZATION Battelle Columbus Laboratories		
6c. ADDRESS (City, State, and ZIP Code) Research Park, P.O. Box 3100 Andover, MA 01810			7b. ADDRESS (City, State, and ZIP Code) 505 King Avenue Columbus, OH 43201-2693		
8a. NAME OF FUNDING/SPONSORING ORGANIZATION U.S. Army Missile Command		8b. OFFICE SYMBOL (if applicable)	9. PROCUREMENT INSTRUMENT IDENTIFICATION NUMBER DAAH01-88-D-0068		
8c. ADDRESS (City, State, and ZIP Code)			10. SOURCE OF FUNDING NUMBERS		
			PROGRAM ELEMENT NO.	PROJECT NO.	TASK NO.
11. TITLE (Include Security Classification) IFELS Program					
12. PERSONAL AUTHOR(S) Simons, G.A.; Nebolsine, P.E.; Person, J.C.; Resendes, D.; Bailey, A.W.; and Humer, N.D.					
13a. TYPE OF REPORT Draft Final		13b. TIME COVERED FROM 890502 TO 890930		14. DATE OF REPORT (Year, Month, Day) 1989 October 23	
15. PAGE COUNT 97					
16. SUPPLEMENTARY NOTATION					
17. COSATI CODES			18. SUBJECT TERMS (Continue on reverse if necessary and identify by block number)		
FIELD	GROUP	SUB-GROUP			
19. ABSTRACT (Continue on reverse if necessary and identify by block number)					
20. DISTRIBUTION/AVAILABILITY OF ABSTRACT <input checked="" type="checkbox"/> UNCLASSIFIED/UNLIMITED <input type="checkbox"/> SAME AS RPT. <input type="checkbox"/> DTIC USERS			21. ABSTRACT SECURITY CLASSIFICATION Unclassified		
22a. NAME OF RESPONSIBLE INDIVIDUAL			22b. TELEPHONE (Include Area Code)		22c. OFFICE SYMBOL

UNCLASSIFIED

SECURITY CLASSIFICATION OF THIS PAGE

UNCLASSIFIED

SECURITY CLASSIFICATION OF THIS PAGE

TABLE OF CONTENTS

<u>Section</u>	<u>Page</u>
1 INTRODUCTION	1
2 SURFACE/SUBSURFACE	2
2.1 Black Materials	2
2.2 Translucent Materials	3
2.3 Extension of Equilibrium Calculations	26
2.3.1 Introduction	26
2.3.2 Approximation to Free Energy and Formation Enthalpy	26
2.3.3 Comparison with Existing Information	27
2.3.4 When Are the Large Molecular Clusters Important?	33
2.3.5 Conclusions	40
3 PLUME DEBRIS/BEAM INTERACTION	41
3.1 Scattering by Particulates	41
3.2 Gas Heating and Laser Absorption	53
3.2.1 Introduction	53
3.2.2 Self-Consistent Calculation of Gas Heating by Laser Absorption	57
3.2.3 Absorption Line Width Estimation	63
3.2.4 Calculation of C ₂ Phillips Band System Spectra	64
3.2.5 Estimation of C ₃ Absorption Spectrum	77
3.2.6 Absorption Spectra of Other Plume Species	82
3.2.7 Equilibrium Calculation of Significant Species in the Ablation Plume	82
4 REFERENCES	87

LIST OF ILLUSTRATIONS

<u>Figure</u>		<u>Page</u>
1	Fluence and Pulse Duration Dependence of the Minimum Surface Temperature	4
2	Minimum Surface Temperature Between Pulses	5
3	Front Surface Temperature Between Pulses One and Three	6
4	Front Surface Temperature Between Pulses 37 and 39	7
5	Extrapolated Pyrolysis Rates	9
6	Post-Irradiation Optical Properties	11
7	Determination of λ_{∞} from Surface Temperature Data	12
8	Determination of λ_{∞} from Mass Loss Data	13
9	Determination of \bar{T} from Surface Temperature Data	15
10	Determination of \bar{T} from Mass Loss Data	16
11	Sensitivity of Surface Temperature to Pyrolysis Rate	17
12	Sensitivity of Mass Loss to Pyrolysis Rate	18
13	Sensitivity of Mass Loss to Pyrolysis Gas Enthalpy	19
14	Sensitivity of Surface Temperature to Absorptance	21
15	Sensitivity of Mass Loss to Absorptance	22
16	Free Energy for C_1 - C_{10}	28
17	Formation Enthalpy at 298 K for C_1 - C_{10}	29
18	Mole Fraction of C_{10} at $P = 1$ atm in Graphite Epoxy under Equilibrium (Solid Curve) and Constrained Equilibrium (Dashed Curve)	34
19	Graphite Epoxy Equilibrium Composition (1 atm)	35
20	Graphite Epoxy Equilibrium Enthalpy (1 atm)	36
21	Pressure Dependence on Temperature for 20 Percent Mole Fraction of C_{10}	38

LIST OF ILLUSTRATIONS (CONTINUED)

<u>Figure</u>		<u>Page</u>
22	Cross Section per Unit Volume	43
23	HeNe Transmission for Material 130 at 124 kW/cm^2	45
24	Scattering Cloud Transmissivity	49
25	Q^* Enhancement via Scattering	50
26	FELS-5 HeNe Transmission for Material 110	52
27	Probe Beam Transmission for $D_S f/V = 1$	54
28	Probe Beam Transmission for $D_S f/V = 3$	55
29	Probe Beam Transmission for $D_S f/V = 9$	56
30	Iteration Procedure to Self-Consistently Solve for Plume Temperature as a Result of Heating by Gas Absorption	63
31	Line Half Width as a Function of Pulse Fluence for a Graphite Epoxy Target with $\tau_p = 60$ and 300 ns	65
32	Absorption Spectrum Calculated for $C_2 X(^1\Sigma_g^+)$ to $A(^1\Pi_u)$ from 0.1 to $1.10 \text{ }\mu\text{m}$	70
33	Effect of Pressure on the Absorption Spectrum Calculated for $C_2 X(^1\Sigma_g^+)$ to $A(^1\Pi_u)$ from 1.06 to $1.07 \text{ }\mu\text{m}$ at $T = 6000 \text{ K}$	72
34	Absorption Spectrum Calculated for $C_2 X(^1\Sigma_g^+)$ to $A(^1\Pi_u)$ from 1.01 to $1.10 \text{ }\mu\text{m}$	73
35	Effect of Temperature on the Absorption Spectrum Calculated for $C_2 X(^1\Sigma_g^+)$ to $A(^1\Pi_u)$ from 1.06 to $1.07 \text{ }\mu\text{m}$ at $p = 10 \text{ atm}$	74
36	Effect of Line Half Width ($\gamma_D + \gamma_L$) on the Absorption Cross Section Calculated at $1.064 \text{ }\mu\text{m}$ for $C_2 X(^1\Sigma_g^+)$ to $A(^1\Pi_u)$	75
37	Effect of Pressure on the Absorption Cross Section Calculated at $1.064 \text{ }\mu\text{m}$ for $C_2 X(^1\Sigma_g^+)$ to $A(^1\Pi_u)$	76
38	Absorption Spectrum of C_3	79
39	Absorption Spectrum of C_3	81

LIST OF ILLUSTRATIONS (CONTINUED)

<u>Figure</u>		<u>Page</u>
40	Enthalpy per Gram of the Equilibrium Gas Mixture That Has the Elemental Composition of Graphite Epoxy at Different Pressures as Functions of Temperature	83
41	Mole Fractions of Species in the Equilibrium Gas Mixture That Has the Elemental Composition of Graphite Epoxy at $p = 10$ atm as Functions of Temperature	84
42	Mole Fractions of Species in the Equilibrium Gas Mixture That Has the Elemental Composition of Graphite Epoxy at $p = 1000$ atm as Functions of Temperature	85

1. INTRODUCTION

The FELS (Free Electron Laser Simulation) program was conducted at Battelle, Columbus Division, using a modified Nd glass laser to obtain experimental data on the interaction of a FEL with composite materials. A simultaneous effort at PSI was directed toward the development of a basis for understanding the performance of these materials and the extrapolation of the data to the full scale scenario. The conclusions of this study (Simons et al., 1989) suggested continued data analysis and model development to be completed on an interim study (IFELS) prior to continued experimental work on the advanced FELS (AFELS) program. This report documents the results of the IFELS study at Physical Sciences Inc. (PSI).

Since the final report (Simons et al., 1989) on the original FELS study was organized phenomenologically, this report was organized similarly in order that we may report the progress in each area. Thus, Section 2 is organized to illustrate the accomplishments in surface/subsurface phenomena and Section 3 discusses the progress in the plume absorption and scattering issues.

2. SURFACE/SUBSURFACE

The efforts in this area of the phenomenology have concentrated on the radiometric data on black materials (Subsection 2.1), the modeling of the surface temperature and mass loss in the translucent materials (Subsection 2.2) and on extending the equilibrium thermochemistry to include larger molecules (Subsection 2.3). Each of these studies has important implications when extrapolating known results to large time and large laser spots.

2.1 Black Materials

Testing of materials under the FELS program utilized sufficiently short test times, i.e., sufficiently low fluence on target, that the residual energy left in the target significantly affected the measured value of Q^* . Hence, it was necessary to understand the residual energy measurements in order to scale the data to a true steady state. It has long been assumed that the surface temperature and residual energy are controlled by the same physics. Analysis of the FELS data (Simons, et al., 1989) revealed that the residual energy is ten times greater than that which would be consistent with the radiometry. It was concluded that residual energy is controlled by that part of the beam ($\phi=0.1$) that "leaks" between the fibers and is deposited over depth L (tens of microns) below the surface. This model was confirmed with model/data comparisons. The surface temperature, however, is controlled by that part of the beam ($1-\phi=0.9$) that is deposited on the fiber in the absorption depth λ_{vf} and diffuses into the fiber with fiber diffusivity, v_f . Surface temperature predictions were presented but the radiometry data was not yet reduced for

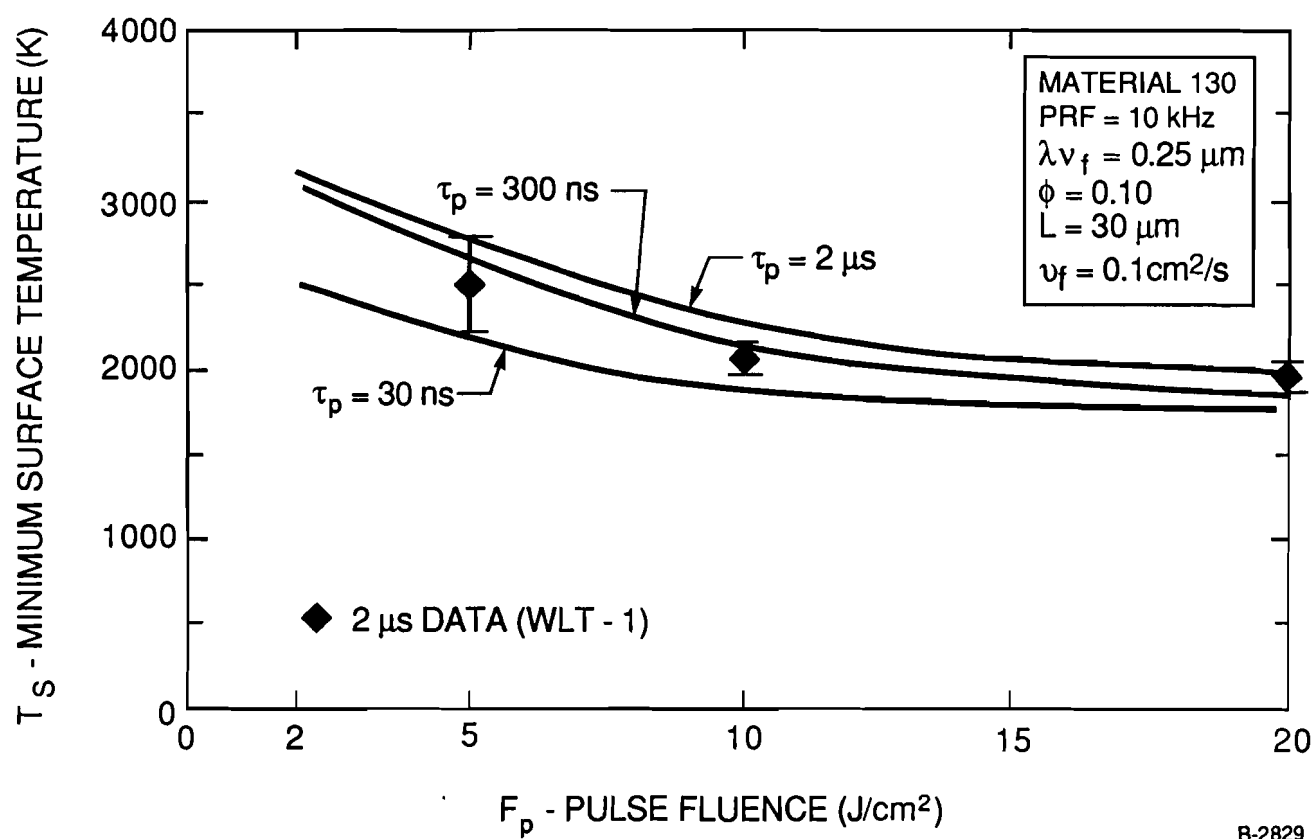
comparison. Some of this radiometry data was reduced in the IFELS program and is utilized below to confirm the physics of the model.

The predicted minimum surface temperature just before the last pulse of each pulse train (30 to 40 pulses) is illustrated in Figure 1. The temperature increases with pulse duration τ_p because there is more time for the energy to diffuse into the fiber. The temperature increases with decreasing pulse fluence because there is less fiber recession to overtake the diffusion front. The WLT-1 data (2 μ s pulses, 36 pulse trains) support the fluence dependence of the model but the pulse duration dependence is yet to be confirmed. The predicted temperatures are slightly higher than actually measured. These predictions may be reduced by reducing the assumed fiber diffusivity from 0.1 cm²/s to 0.05 cm²/s. Figure 2 illustrates the consistency of this approach in predicting the minimum temperature at the end of the train. Radiometry data (Figures 3 and 4) for the temperature between the first three pulses of the first two trains (Pulse 1, 2, 3 and 37, 38, 39) also support the predictions illustrated in Figure 2.

As short pulse radiometry data becomes available, we will compare it to our predictions. While it is not our intention to make surface temperature predictions per say, it is our goal to validate the pulse fluence and pulse duration dependence of our model against all observables in order that we may more confidently predict the corresponding dependence of Q^* on these laser parameters.

2.2 Translucent Materials

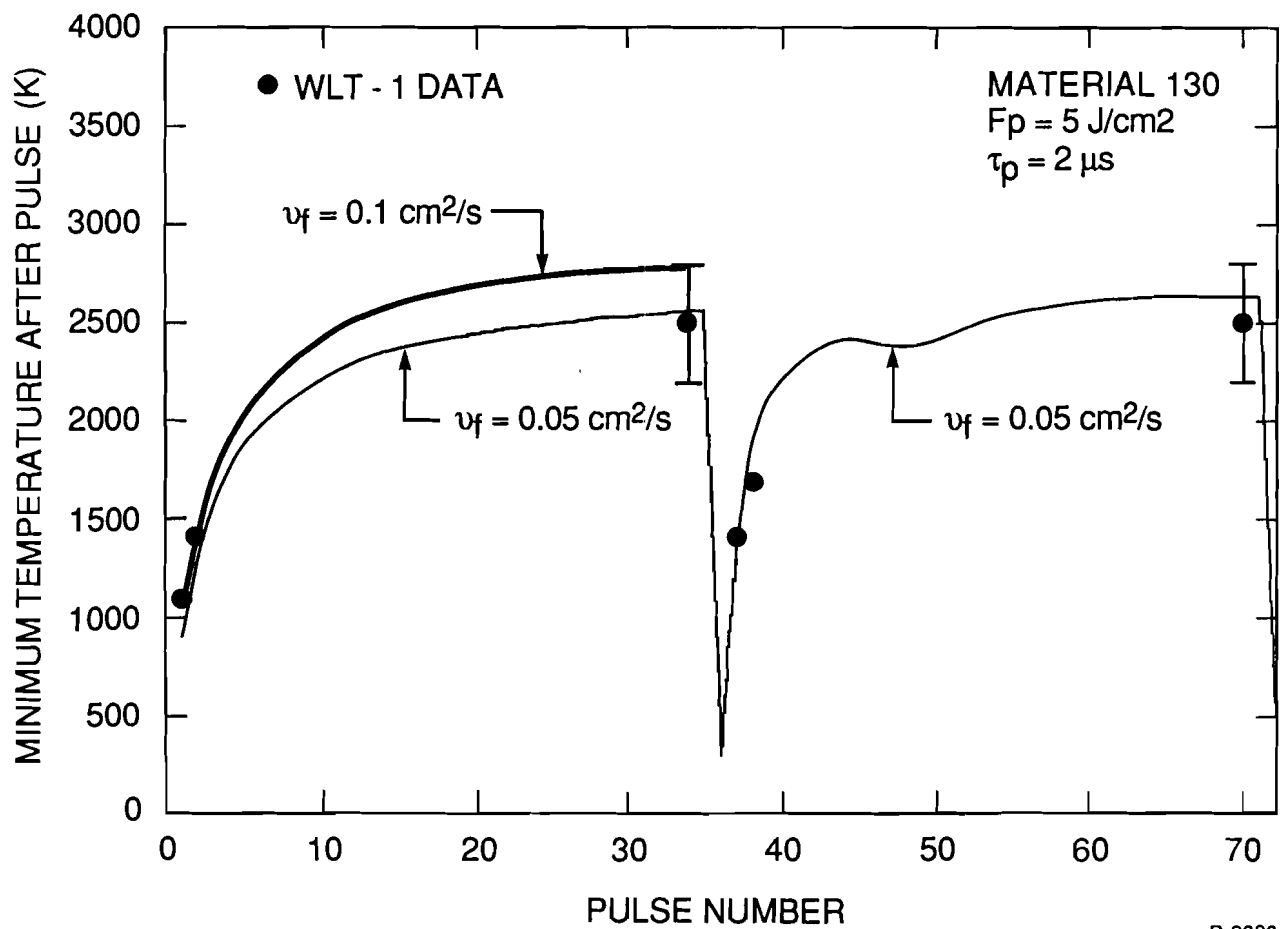
During the original FELS program, PSI (Simons, et al., 1989) developed models for time dependent charring and explosive pyrolysis of translucent



B-2829

Figure 1.

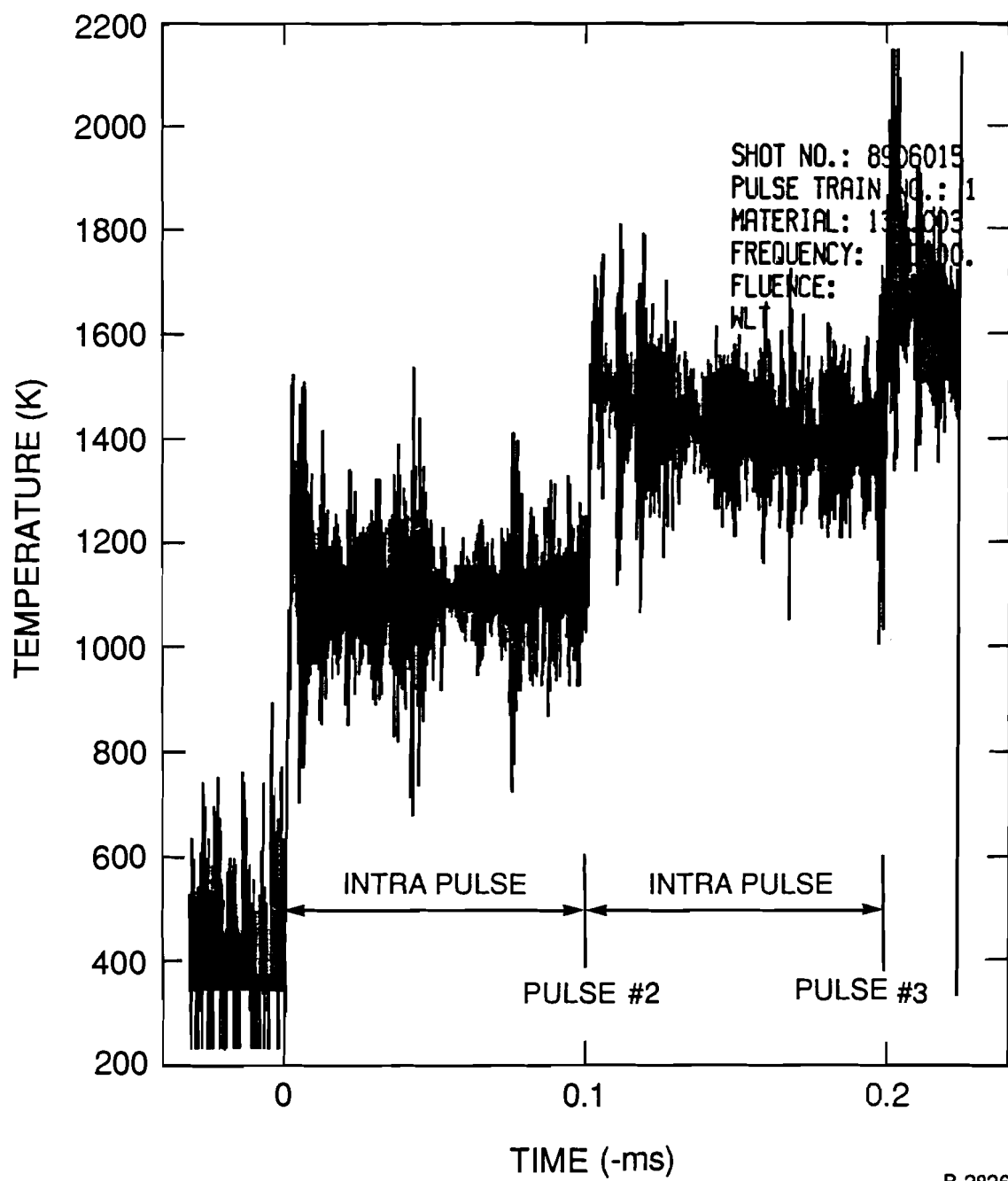
Fluence and Pulse Duration Dependence of the Minimum Surface Temperature



B-2828

Figure 2.

Minimum Surface Temperature Between Pulses



B-2826

Figure 3.

Front Surface Temperature Between Pulses One and Three

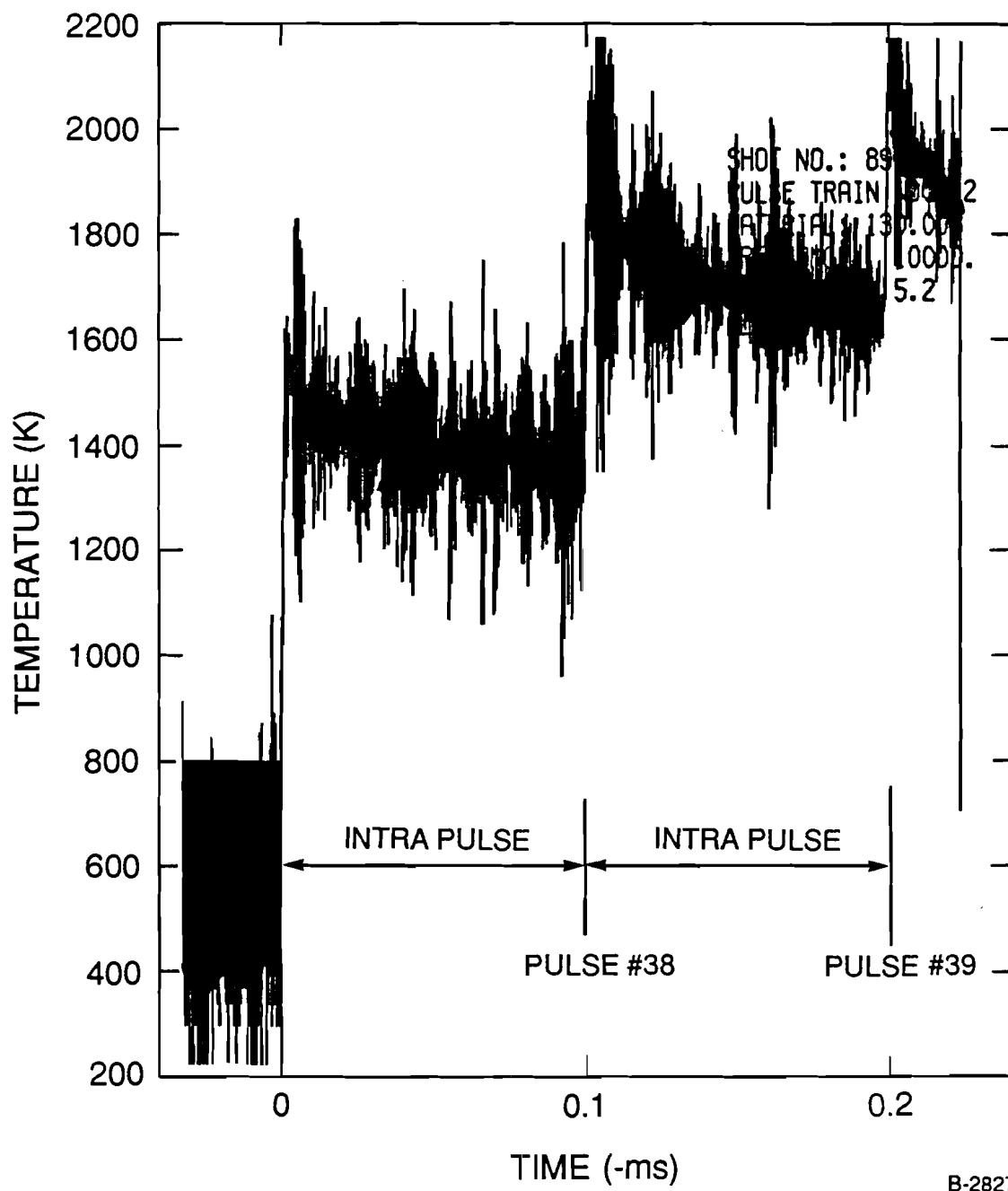


Figure 4.

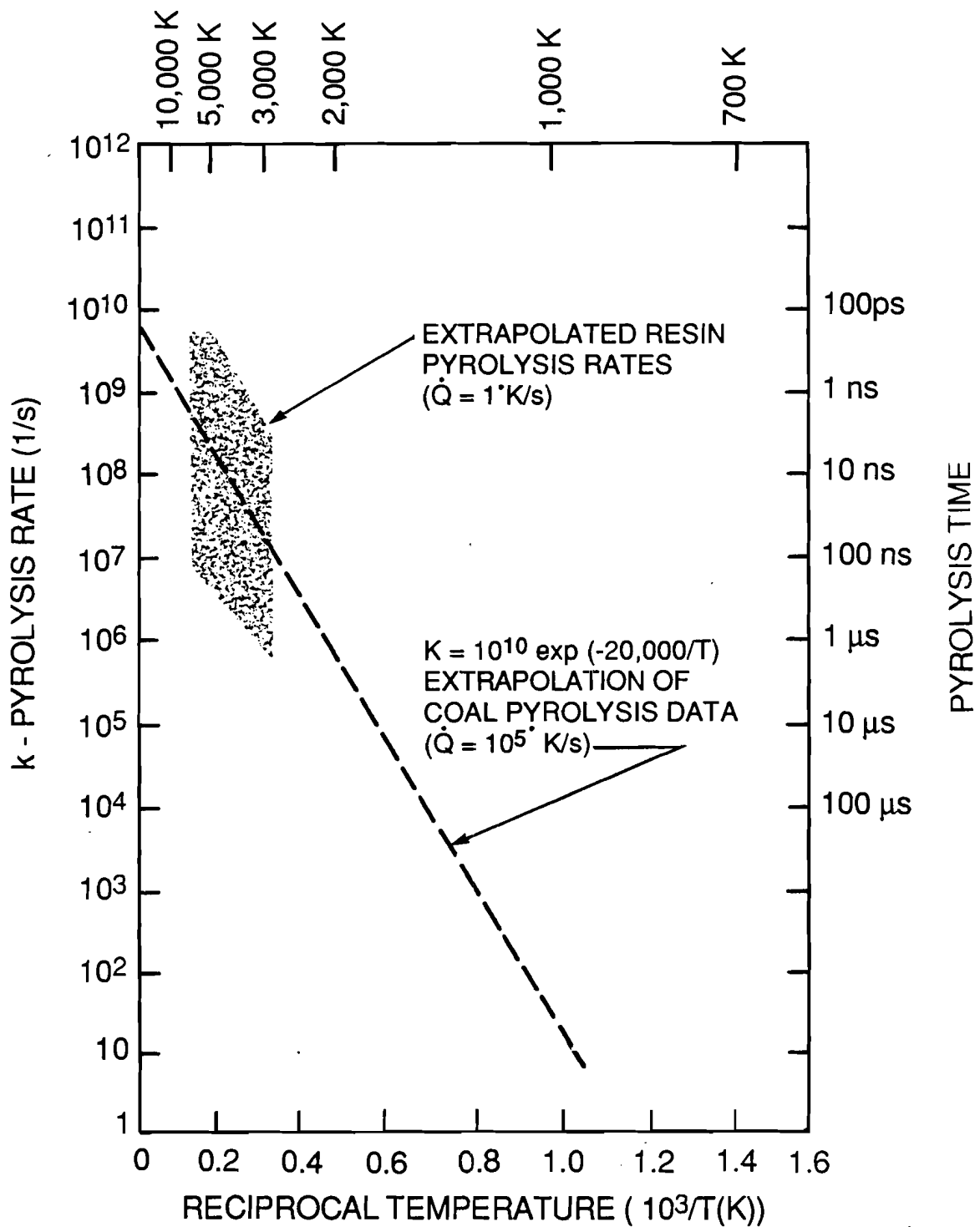
Front Surface Temperature Between Pulses 37 and 39

materials. At the conclusion of the FELS program, our efforts were directed toward combining these effects into a single computational capability for predicting observables such as mass loss, recession, surface temperature and residual energy. However, several of the model inputs are still not accurately known: the most critical are the fluence dependent absorptance of the material, the absorption depth of the fully charred material, λ_{∞} , the pyrolysis rate (k) of the resin, the temperature dependent strength $\sigma_u(T)$ of the material, and the enthalpy of the pyrolysis gas when exposed to the surface temperature T_s .

Baseline values of these parameters have been determined and sensitivity studies carried out to isolate the most important unknowns in order that we may define a test series to either directly or indirectly measure them. The baseline values of these parameters are discussed below.

The enthalpy of the pyrolysis gas when exposed to the surface temperature T_s and corresponding surface pressure have been calculated assuming equilibrium thermochemistry. To a good approximation, the pyrolysis gas behaves as though it were a gas with a C_p of approximately 5 up to a temperature of 4000 K with a constant enthalpy (~20 kJ/g) above 4000 K.

The resin pyrolysis rates were obtained by extrapolating measured values (obtained at 1000 K and heating rates of 1 K/s) to temperatures of 5000 K and heating rates of 10^{10} K/s. These extrapolations are illustrated in Figure 5 and are supported by extrapolated coal (a similar C-O-H system) pyrolysis data taken at 2000 K and heating rates of 10^5 K/s. A factor of ten uncertainty in the pyrolysis rate is evident.



A-5747a

Figure 5.

Extrapolated Pyrolysis Rates

The material strength and thermal degradation thereof are assumed to be of the form

$$\sigma_u(T) = \sigma_0 \exp(-\bar{T}/300) \exp(\bar{T}/T)$$

where σ_0 (1000 atm) is the yield stress at room temperature and $\bar{T} = 1000$ allows that to decay to 60 atm at blowoff temperatures of the order of 2000 K. Similarly, $\bar{T} = 1500$ reduces the strength to 15 atm at that same blowoff temperature.

In working with the explosive pyrolysis model, it is important to note that the gas pressure in the pores increases with \sqrt{k} . When the gas pressure exceeds the yield stress σ_u , mechanical mass loss occurs. Hence, the ratio of \sqrt{k} to σ_u is the critical parameter for establishing mechanical mass removal.

The average absorptance is yet another major variable. Measurements (Figure 6) illustrate that the absorptance is as low as 0.25 on the virgin material and as high as 0.7 on the fully charred material. The absorptance is assumed to vary linearly with the fraction (f) of the material charred.

$$\alpha = 0.25 (1-f) + 0.7 f$$

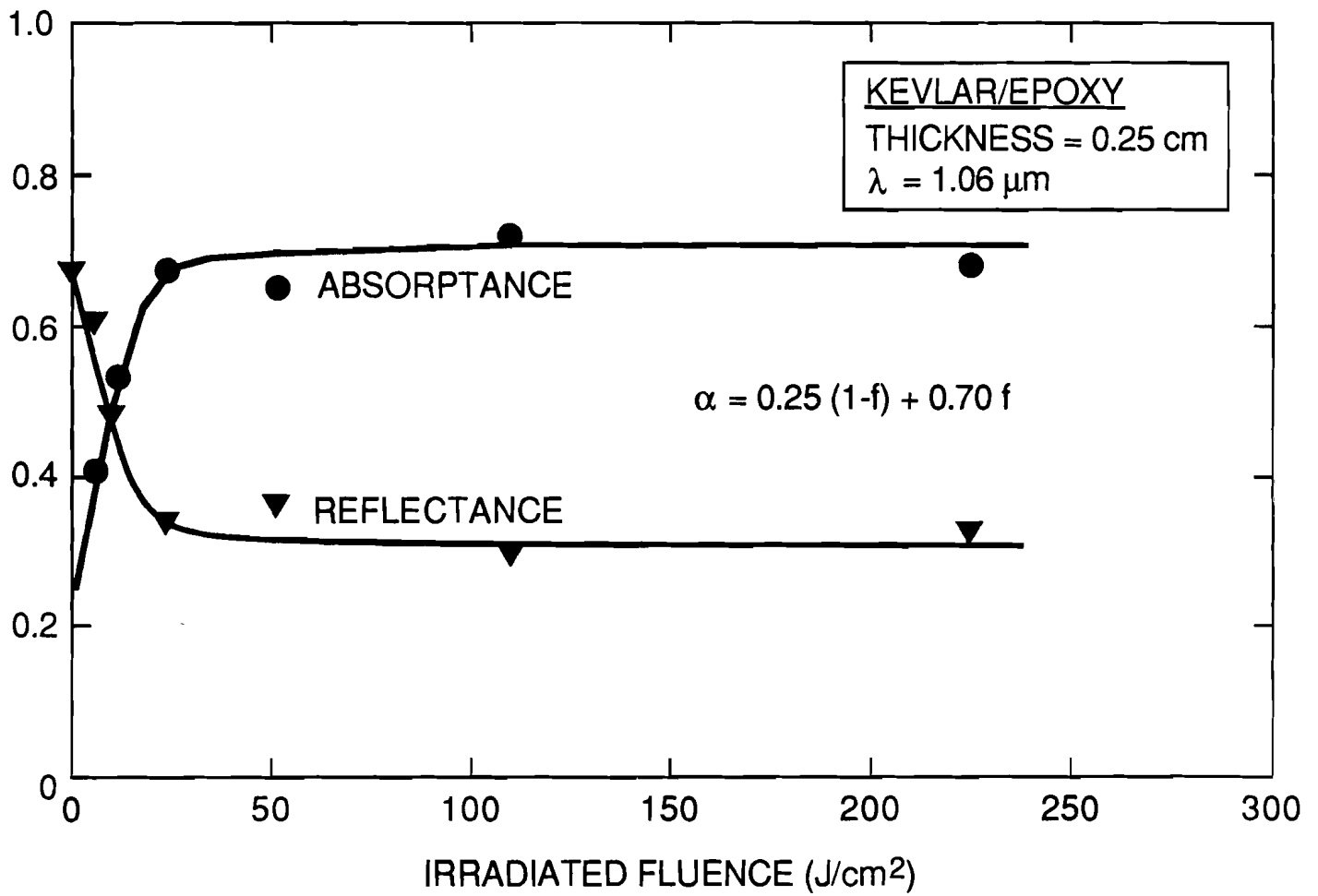
Since f varies with depth, we must determine the proper average value of α to use. Two approaches have been used: 1) the evaluation of f at the material surface, and 2) the weighting $\alpha(f)$ with the change in intensity in-depth.

$$1) \quad \alpha(0) = \alpha \text{ at } x = 0$$

$$2) \quad \bar{\alpha} = \int \alpha dI / \int dI$$

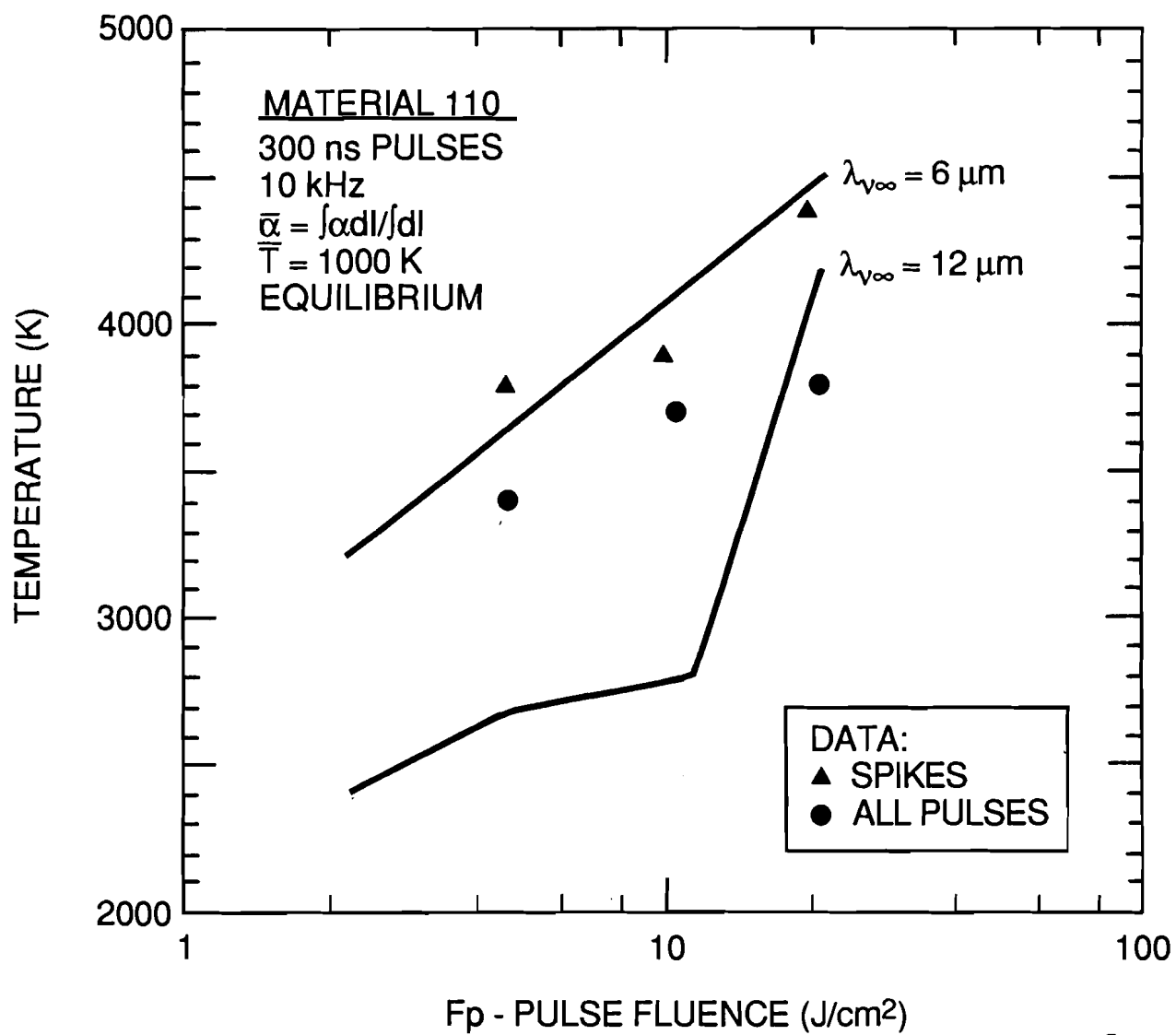
The baseline values of these parameters may be determined/confirmed through comparison of the model to FELS-7C data for material 110.

Figures 7 and 8 illustrate the effect of λ_{∞} on surface temperature and



A-8518a

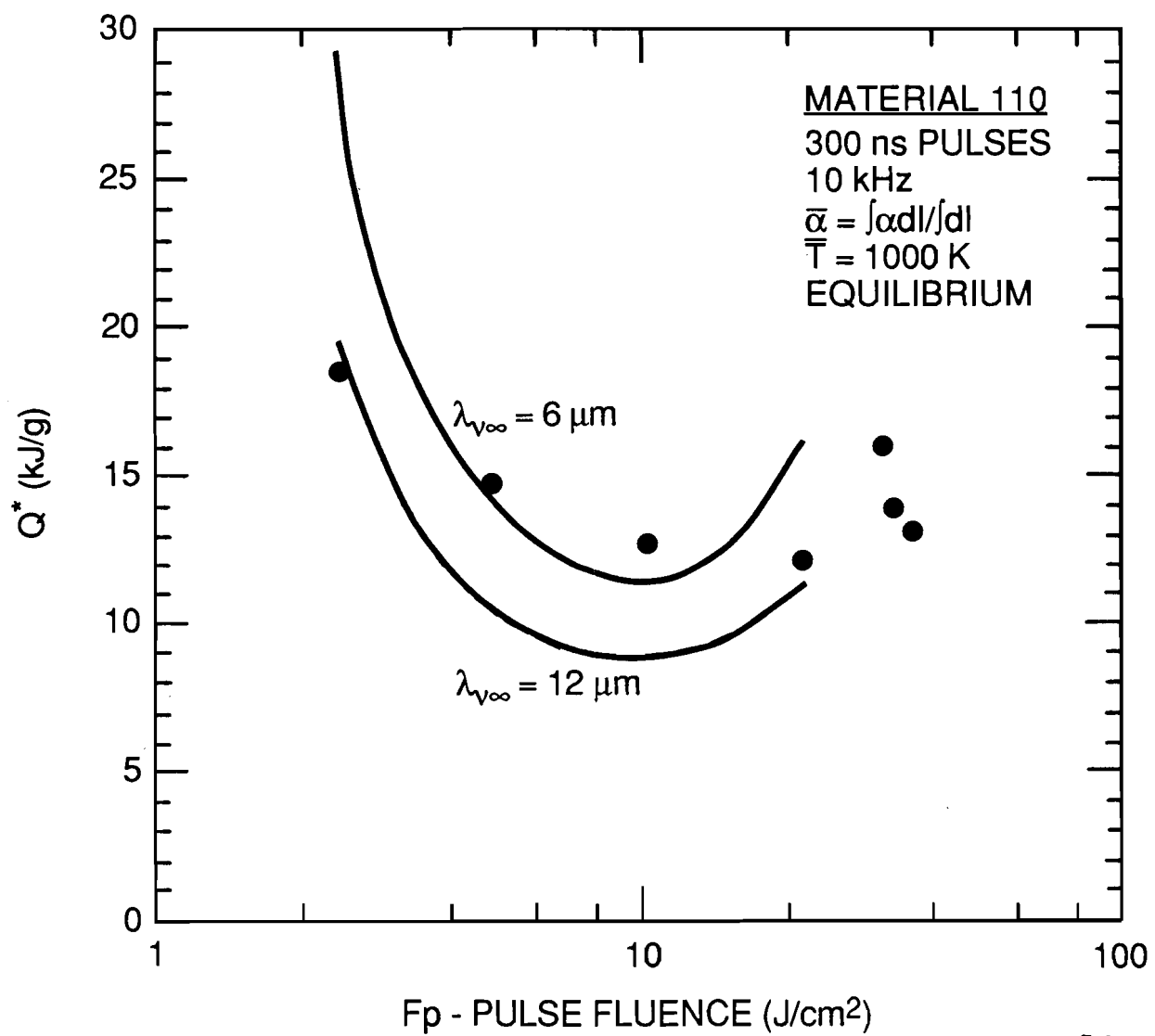
Figure 6.
Post-Irradiation Optical Properties



B-2185

Figure 7.

Determination of $\lambda_{v\infty}$ From Surface Temperature Data



B-2186

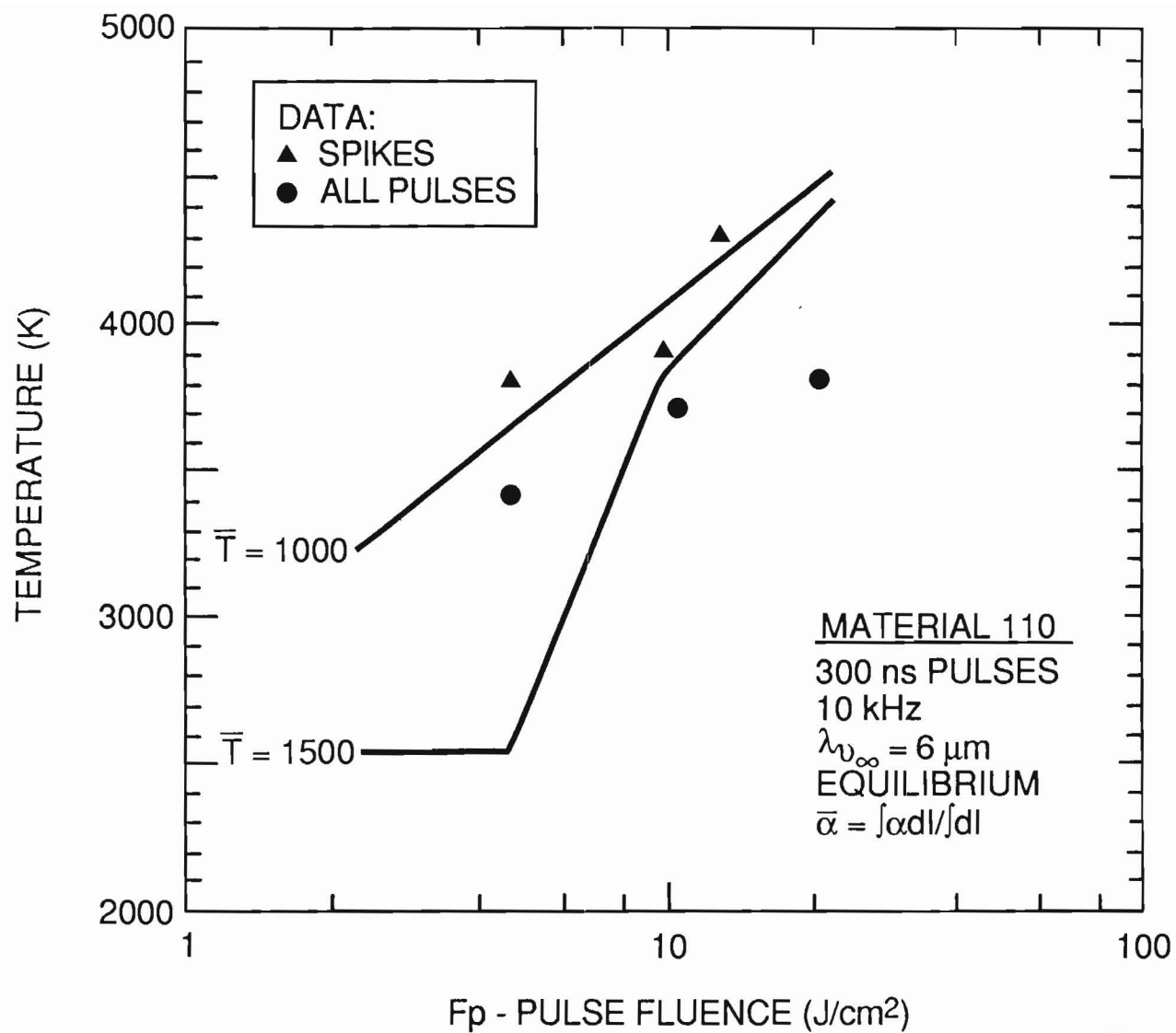
Figure 8.
 Determination of λ_{∞} From Mass Loss Data

mass loss respectively. Larger values of λ_{∞} cause more blowoff (lower Q^*) and colder surface temperatures. A value of $6 \mu\text{m}$ is consistent with data wherein the surface temperature is the more sensitive variable.

The material strength parameter \bar{T} is varied to illustrate the corresponding changes in surface temperature and mass loss in Figures 9 and 10 respectively. In these cases, blowoff occurred at 2000 K. Hence $\bar{T} = 1000$ and 1500 K correspond to ultimate strengths of 60 and 15 atm respectively. Surface temperature is again the more sensitive variable and suggests a value of \bar{T} of the order of 1000 K.

The role of pyrolysis rate is illustrated in Figures 11 and 12. Higher pyrolysis rates increase the blowoff and expose colder surfaces while lower pyrolysis rates reduce blowoff and cause the surface material to remain in tact and be heated to elevated temperatures. The extrapolated values of pyrolysis rates are consistent with both the available data and the current values of \bar{T} and λ_{∞} .

All of the calculations presented above predict a sharp increase in Q^* at fluences above 10 J/cm^2 . This is due to the enthalpy of the pyrolysis gas. The sensitivity of the calculated mass loss to this property of the target material is illustrated in Figure 13. Using equilibrium to determine the effective value of C_p , we obtained $C_p \sim 5$ whereas for a non-reacting gas, C_p is of order 2. The mass loss data support the non-reacting limit in which the pyrolysis products (large aromatic rings) do not decompose further into C, C_2 , and C_3 . Future test series which measure plume gas species will illuminate the nature of the pyrolysis gas and the corresponding value of the enthalpy.



B-2191

Figure 9.

Determination of \bar{T} from Surface Temperature Data

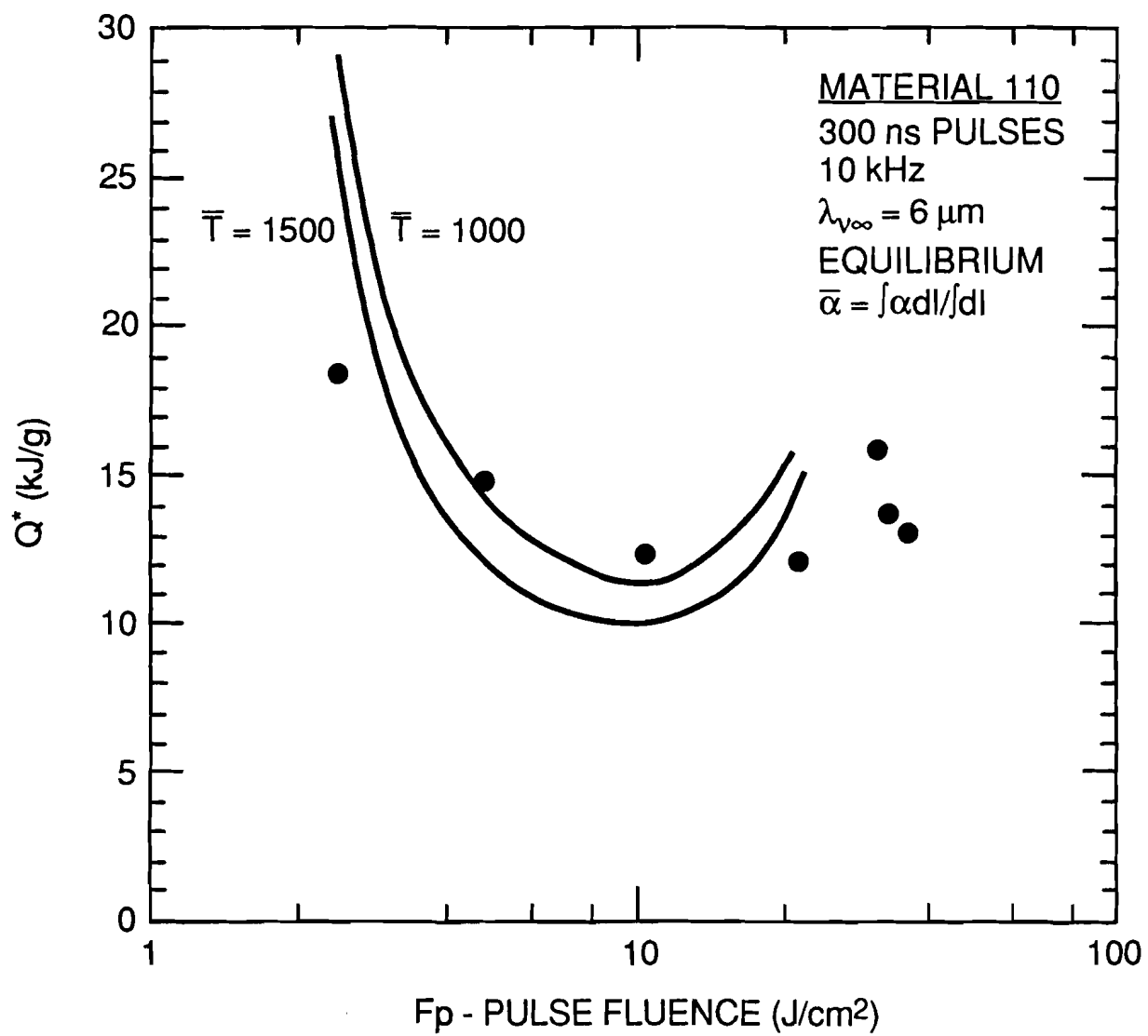
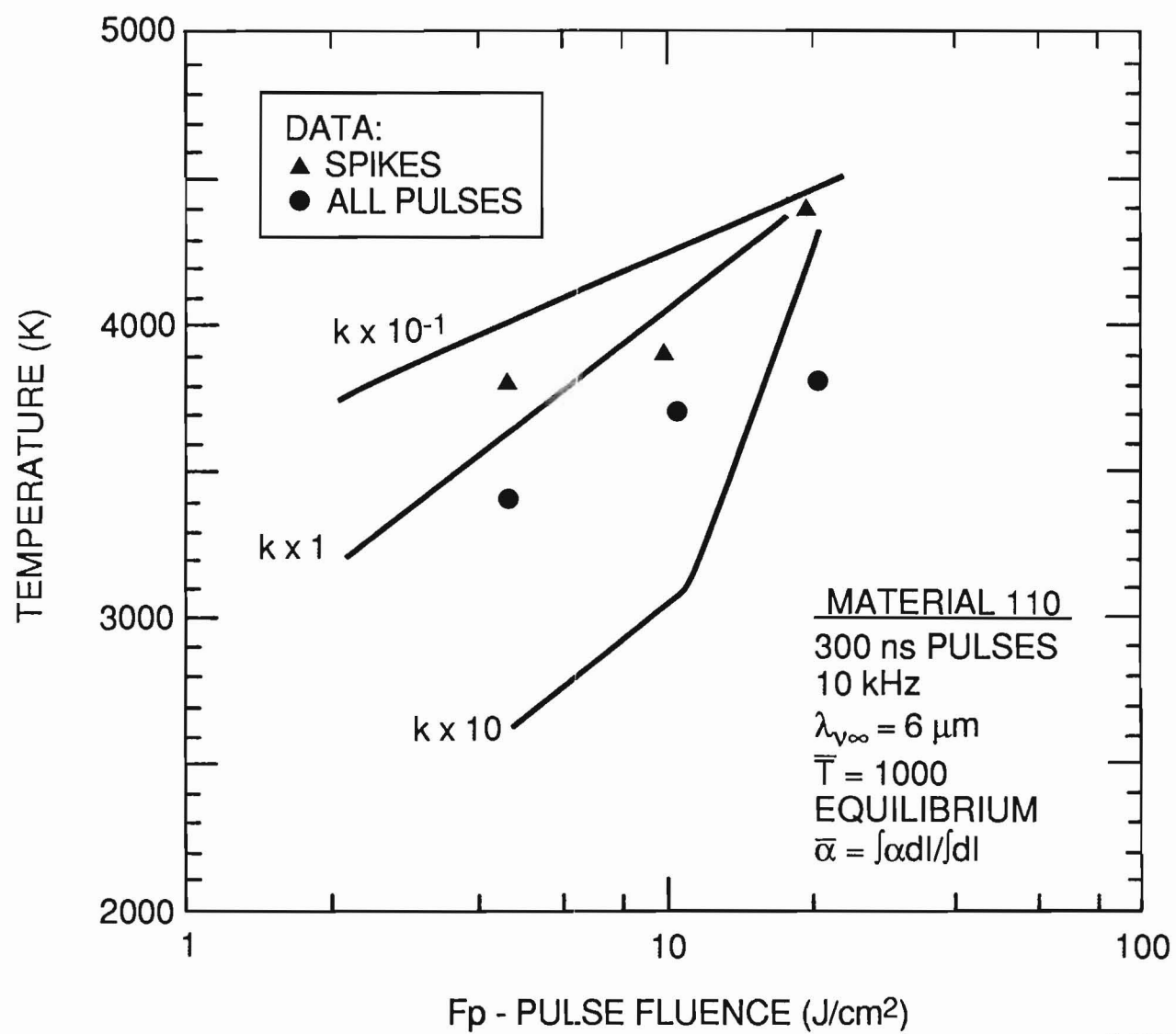


Figure 10.

Determination of \bar{T} from Mass Loss Data



B-2189

Figure 11.

Sensitivity of Surface Temperature to Pyrolysis Rate

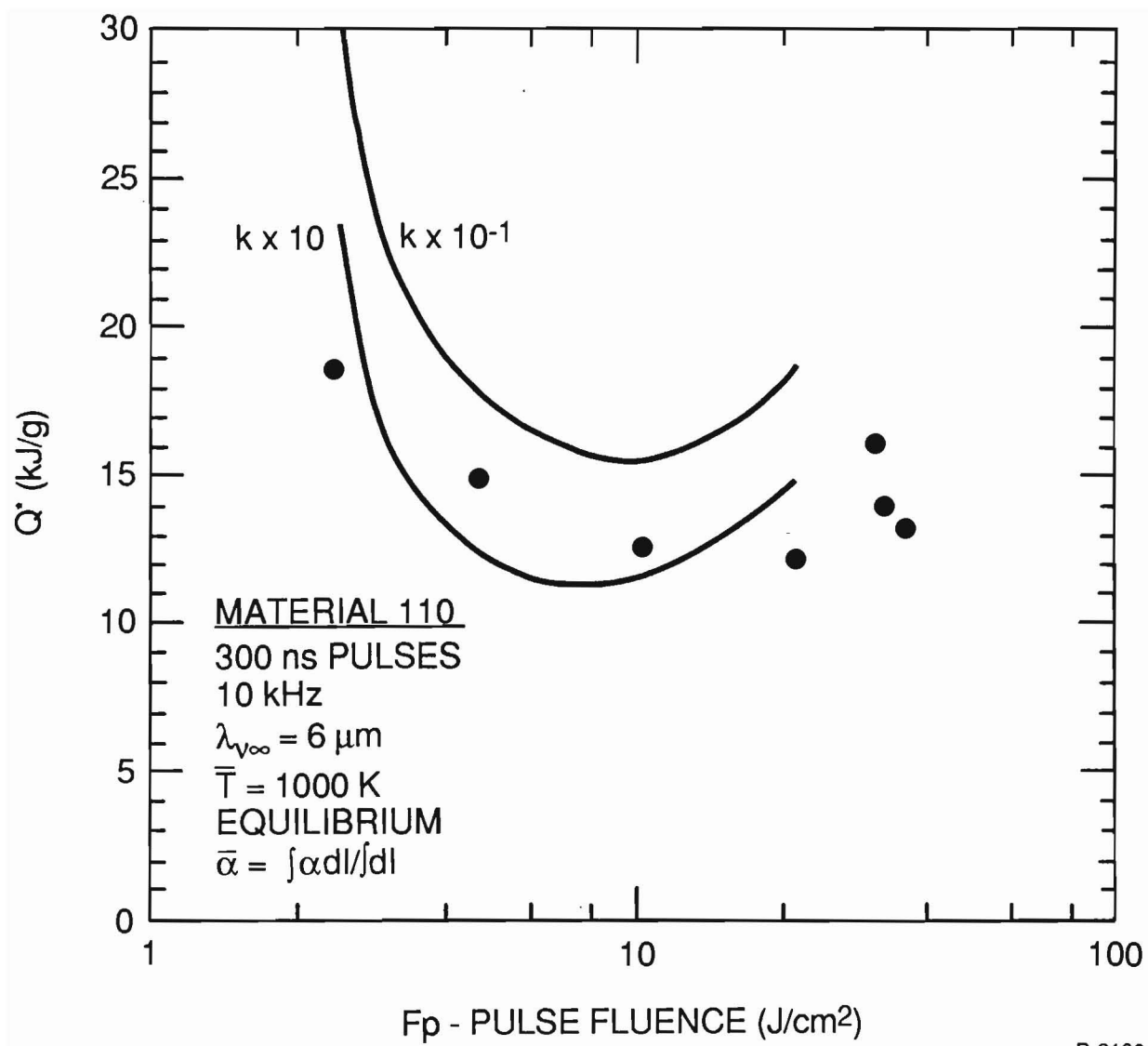
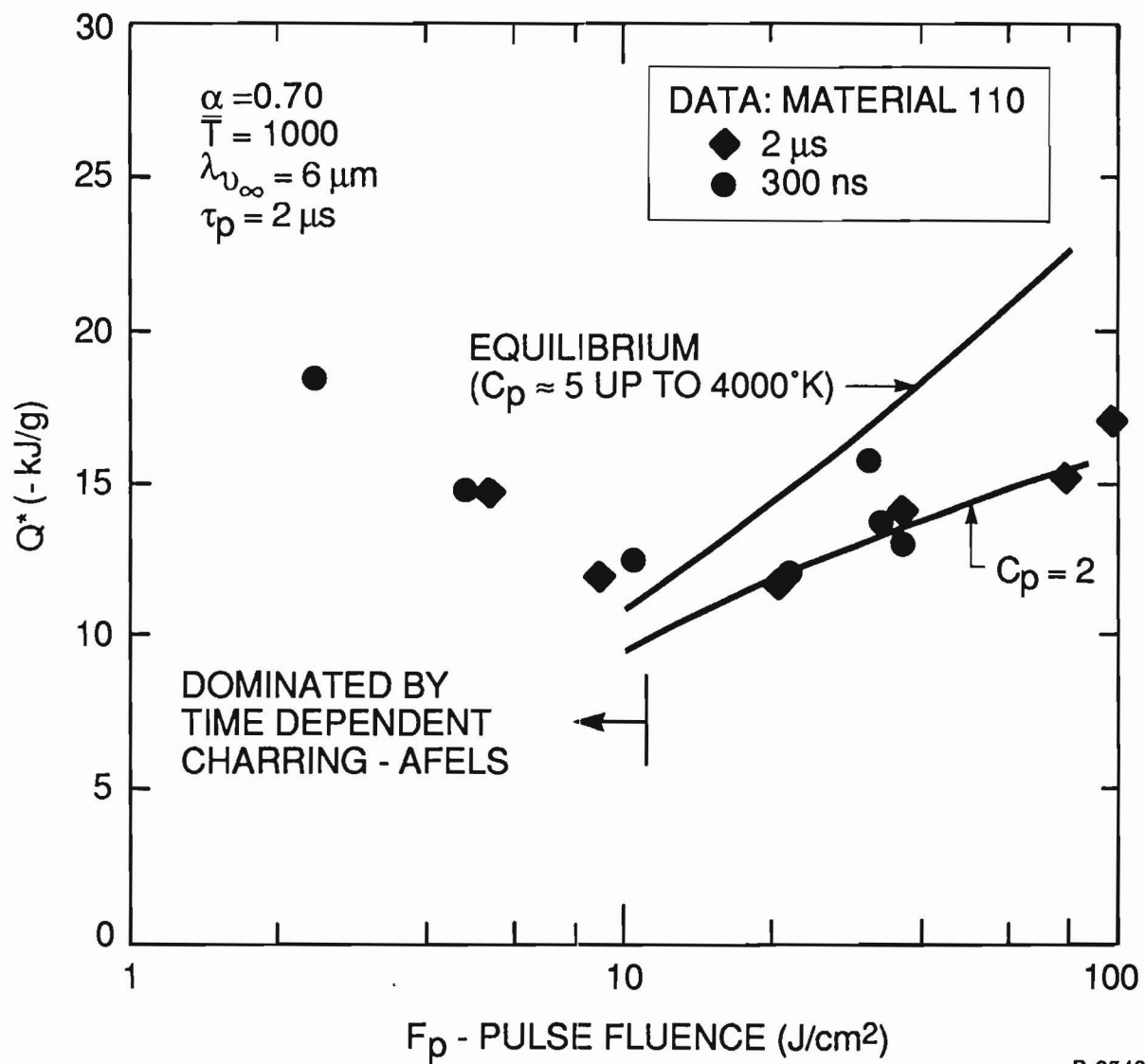


Figure 12.

Sensitivity of Mass Loss to Pyrolysis Rate



B-2548

Figure 13.

Sensitivity of Mass Loss to Pyrolysis Gas Enthalpy

The sensitivity of the surface temperature and mass loss predictions to the material absorptance is illustrated in Figures 14 and 15 respectively. Clearly the single most important parameter controlling mass loss at low fluence ($F_p < 10 \text{ J/cm}^2$) is the relationship between charring and material absorptance. A complete understanding of the data illustrated in Figure 6 will be fundamental to the understanding of this phenomena.

The parameter studies described above have indicated that the time dependent charring and absorptance are the major factors controlling mass loss in a translucent material at low fluence. The absorptance and reflectance of a translucent material are controlled by the scattering at the fiber/resin interface and a two flux model is necessary to describe this phenomena.

If the forward flux is i and the backscattered is j , then the i component is decreased due to scattering S and absorption α but enhanced due to scattering of the j component. Hence

$$\frac{di}{dx} = - Si - \alpha i + Sj$$

and

$$\frac{dj}{dy} = - Sj - \alpha j + Si$$

where $x = -y$. If S and α are constant then i and j are of the form

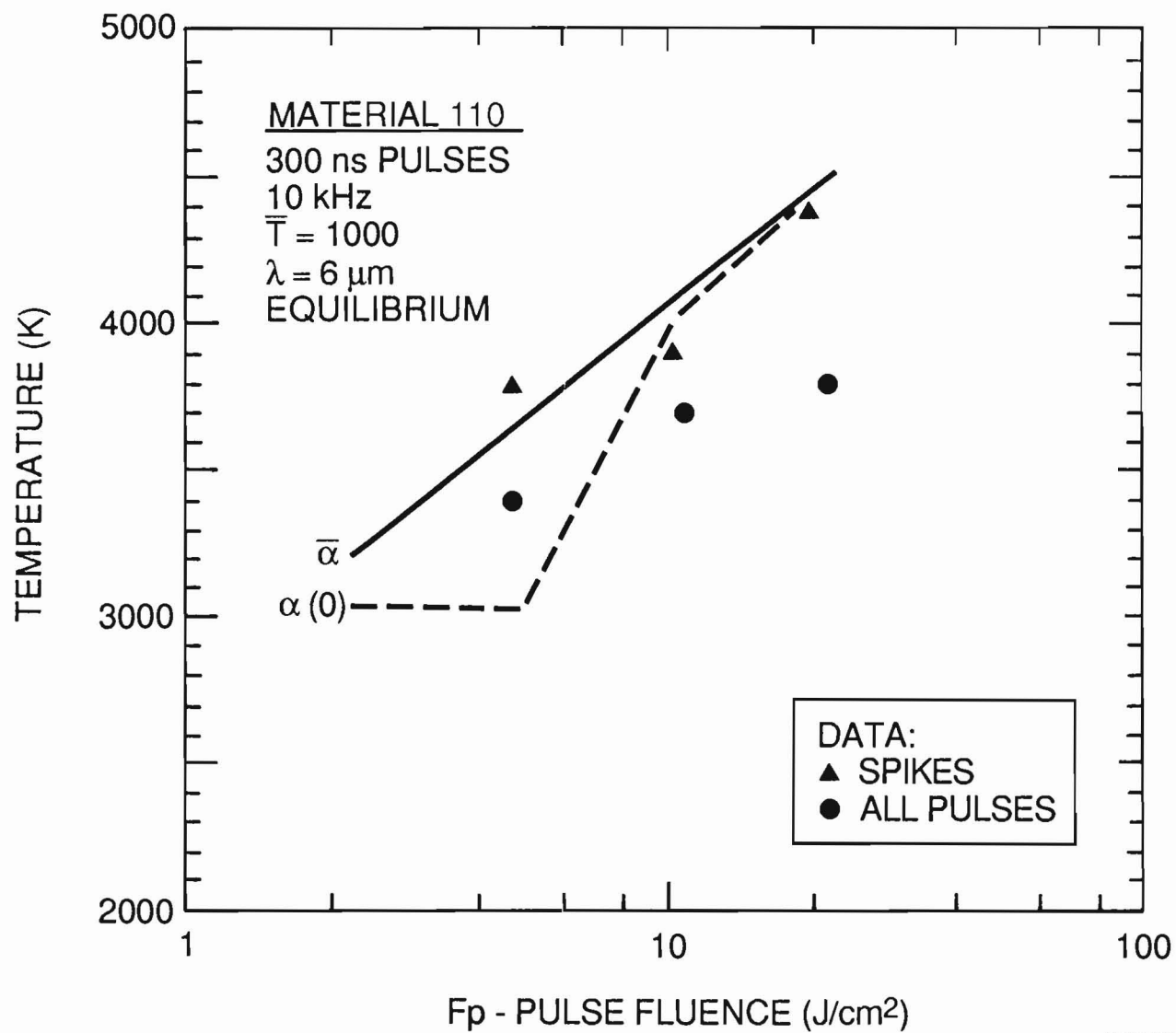
$$i = I_0 e^{-\beta x}$$

and

$$j = R I_0 e^{-\beta x}$$

where the effective absorptivity β is

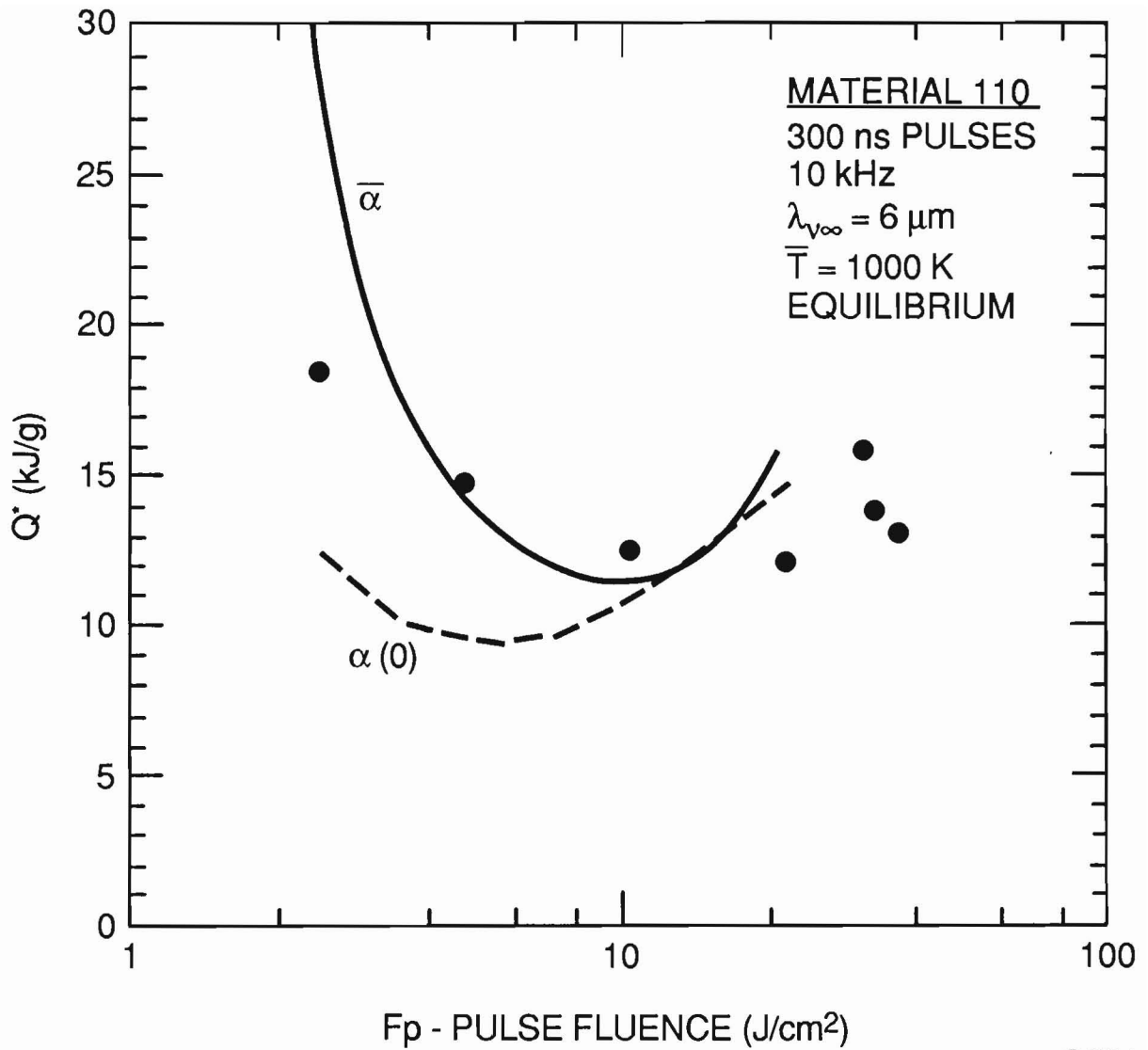
$$\beta = \alpha \left(1 + \frac{2S}{\alpha} \right)^{1/2}$$



B-2193

Figure 14.

Sensitivity of Surface Temperature to Absorptance



B-2194

Figure 15.
 Sensitivity of Mass Loss to Absorptance

and the reflection coefficient R is

$$R = \frac{\beta - \alpha}{\beta + \alpha} \quad .$$

Rewriting the relationship between S and R

$$\frac{2S}{\alpha} = \left(\frac{1 + R}{1 - R} \right)^2 - 1$$

or

$$\frac{2S_v}{\alpha_v} = 48$$

for the virgin material ($R_v = 0.75$) and

$$\frac{2S_c}{\alpha_c} = 2.45$$

for the charred ($R_c = 0.3$) material. The corresponding relationship between β_c and α_c is then

$$\beta_c = 1.86 \alpha_c$$

where β_c is identically the reciprocal of the effective absorption depth ($6 \mu\text{m}$) of the fully charred material in the single flux model used in the parameter studies above

$$\beta_c = (6 \mu\text{m})^{-1}$$

and α_c now reflects the actual absorption depth of the fully charred material

$$\lambda_{\infty} = \frac{1}{\alpha_c} = \frac{1.86}{\beta_c} \div 10 \mu\text{m} \quad .$$

Similarly, for the virgin material,

$$\beta_v = 7 \alpha_v$$

and the virgin absorptivity is approximately

$$\alpha_v = 1/\lambda_{v0} = 1 \text{ cm}^{-1}$$

which requires an effective absorption depth of

$$\lambda_v = 1/\beta_v = 1.4 \text{ mm}$$

due to the multiple passes in the scattering environment.

Assuming that scattering occurs on the interface between the resin and the fiber, we write

$$S = 2\sigma/D$$

where we have assumed that there are two surfaces per lattice spacing D

($D = 10 \text{ } \mu\text{m}$) and σ is the reflection per surface. The corresponding properties of the virgin and charred materials are:

$$R_v = 0.75$$

$$R_c = 0.30$$

$$\alpha_v = 1 \text{ cm}^{-1}$$

$$\alpha_c = 10^3 \text{ cm}^{-1}$$

$$\beta_v = 7 \text{ cm}^{-1}$$

$$\beta_c = 1860 \text{ cm}^{-1}$$

$$S_v = 24 \text{ cm}^{-1}$$

$$S_c = 1225 \text{ cm}^{-1}$$

$$\sigma_v = 0.012$$

$$\sigma_c = 0.61$$

Using the properties of the virgin and charred material, it is reasonable to assume that the absorptivity α and reflectance R scale in direct proportion to the fraction (f) of material that has charred

$$\alpha = \alpha_c f + \alpha_v(1-f)$$

$$R = R_c f + R_v(1-f)$$

where f is controlled by the growth of N sites of radius r

$$f = (4\pi/3) r^3 N$$

and each site heats and grows due to the absorption of laser irradiation.

We previously balanced the absorbed intensity I_A with the heating, growth and spherical conduction of energy

$$\pi r^2 I_A = \frac{\partial}{\partial t} \left(\frac{4}{3} \pi r^3 \rho c T \right) + k_t 4 \pi r^2 \left(\frac{T}{r} \right) .$$

If the site heats (or cools) when $T < T_{\max}$ and grows when $T = T_{\max}$ we may write

$$\frac{\partial T}{\partial t} = \frac{r I_A - 4 k_t T}{\frac{4}{3} \rho c r^2}$$

for r fixed and $T < T_{\max}$ or

$$\frac{\partial r}{\partial t} = \frac{r I_A - r k_t T_{\max}}{4 r \rho c T_{\max}}$$

for $T = T_{\max}$ and $\partial r / \partial t \geq 0$. Currently, I_A is expanded to include both the i and the j component

$$I_A = g(I_i + I_j)$$

and a geometric factor g to account for the fact that the initial site ($r = r_0$) is completely absorbing and the charred material around the site absorbs with depth λ_{∞} , i.e.,

$$\begin{aligned} \pi r^2 I_A &= \pi r_0^2 (I_i + I_j) \\ &+ \pi (r^2 - r_0^2) (I_i + I_j) (1 - e^{-r/\lambda_{\infty}}) \end{aligned}$$

or

$$g = 1 - (1 - r_0^2/r^2) e^{-r/\lambda_{\infty}}$$

The two flux deposition model has been programmed into the PSI ablation/explosive pyrolysis code. Initial de-bugging is complete and the model is undergoing initial model/data comparison with the FELS-7B, 7C and WLT-1 mass loss and radiometry data.

2.3 Extension of Equilibrium Calculations

2.3.1 Introduction

Equilibrium thermochemistry has been used to predict gas species during vaporization and the subsequent values of Q^* . However, the calculations did not include (for lack of thermodynamic data) large carbon rings as an allowable species. The presence of large amounts of aromatic rings would not only reduce Q^* , but would impact the work on beam absorption by gas species as well. Below, we extend our previous analysis to include the effect of C_8 , C_{10} , C_6H , C_8H , and $C_{10}H$ on the equilibrium properties of graphite epoxy and epoxy under pyrolysis and vaporization conditions. First we shall examine the thermodynamic properties of these large molecules and describe our method of generating approximate partition functions for them. Comparison is made with existent Sandia data. Secondly, we will examine under what conditions of temperature, pressure, and elemental composition these molecules contribute significantly to the equilibrium. The constrained equilibrium case is also examined. The relative importance of C_6H to C_6 , C_8H to C_8 and $C_{10}H$ to C_{10} is illustrated. It should be pointed out that the spirit of this work was exploratory in nature. As a result some of the approximations made can be readily and obviously improved. These potential improvements will be pointed out along the way.

2.3.2 Approximation to Free Energy and Formation Enthalpy

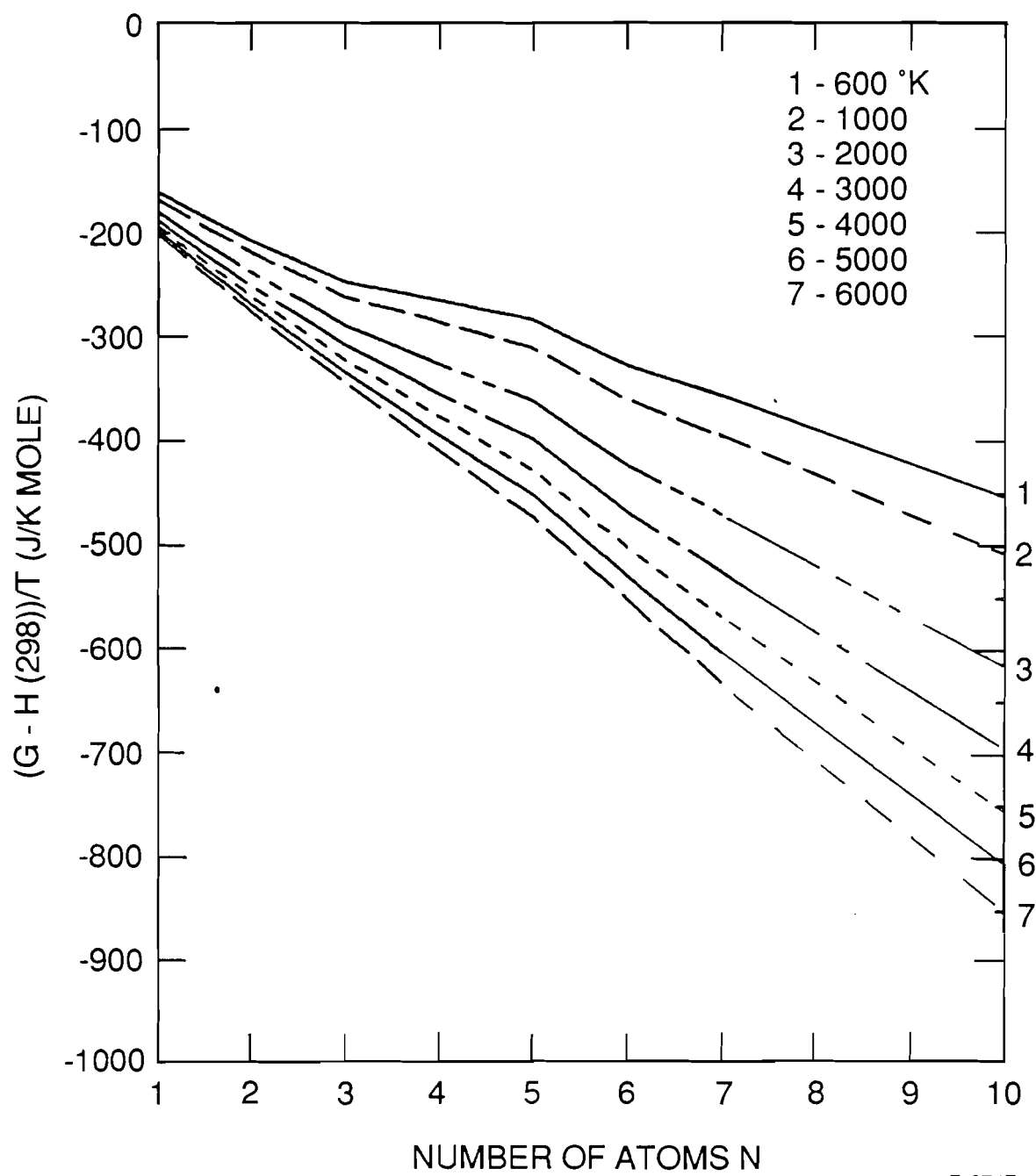
To generate curve fits for the partition functions for the molecules C_8 , C_{10} , C_8H , $C_{10}H$, and C_6H , information on free energy in the form $[G^0(T) - H^0(T_R)]/T$ and formation enthalpies at the reference temperature $T_R = 298.15$ K are required. Lacking thermodynamic data we make the approximations to both the free energy and formation enthalpy:

1. Linearly extrapolate from known data (Gustafson, 1986; Lee and Sanborn, 1973; Leider et al., 1973; Chase et al., 1985) for C_1 - C_7 to larger C-clusters.
2. Treat C_6H as C_6 and $C_{10}H$ as C_{10} , i.e., neglect the modifications introduced by the C-H bond entirely except in the composition and molecular weight; the energetics, however, remain unchanged.

The extrapolated free energy for seven different temperatures appears in Figure 16, while the extrapolated formation enthalpy at 298 K appears in Figure 17. The upper limit of 6000 K conforms to well established information. As an example, the extrapolated values for C_{10} appear in Table 1 along with thermochemical information and the curve fit for $\ln(Q)$ as a function of temperature generated by a non-linear least squares fitting routine. The chemical equilibrium code used requires enthalpies relative to absolute zero degrees not room temperature $T = 298$. This enthalpy increment which is $10.51 \text{ kJ mol}^{-1}$ and amounts to about 0.5 percent of the formation enthalpy of C_{10} at 298 K has been neglected. As can be seen the H and C_p fits have unphysical negative values. This is, however, not surprising since we have used seven values to generate a seven parameter fit. An obvious improvement can be made here.

2.3.3 Comparison with Existing Information

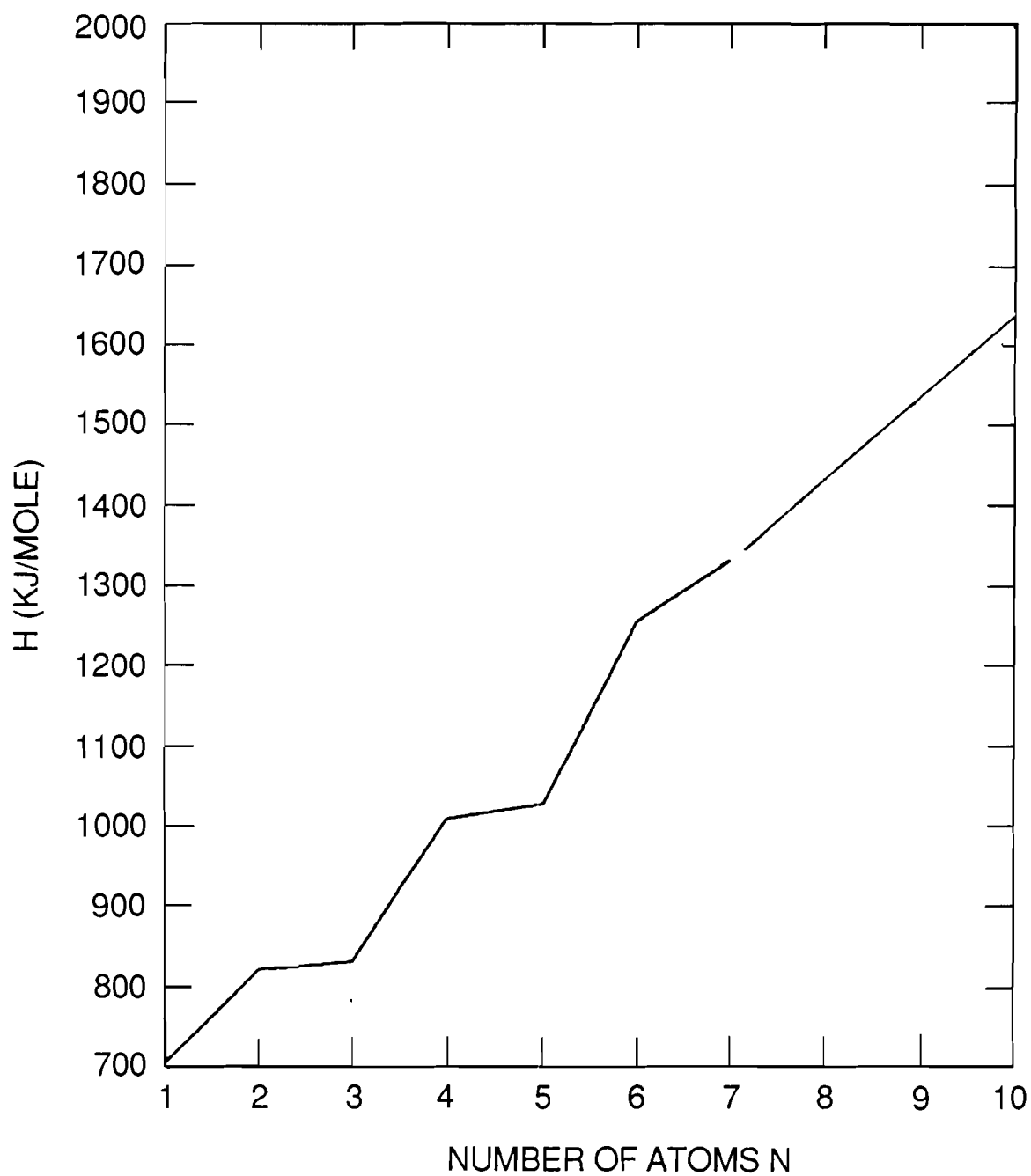
We compare the inputs to the partition function fitting routine, namely $-[G^0(T) - H^0(298)]/T$ and $\Delta H_f^0(298)$ to Sandia thermochemical fits (Burcat, 1984; Miller and Bowman, 1988). The results of our comparison appear in Tables 2 and 3. Comparing C_6H we find a 40 percent discrepancy in the formation enthalpy but the free energies are surprisingly close (Table 2). For C_8H we find an 18 percent discrepancy in the formation enthalpy and a 7.5 percent



B-2747

Figure 16.

Free Energy for C_1 - C_{10}



B-2748

Figure 17.
Formation Enthalpy at 298 K for C₁-C₁₀

Table 1. Extrapolated Thermochemical Properties of C₁₀

Molecule: C ₁₀ , mw = 120.11, Ideal Gas $\Delta H_f(298.15) = 1600.0 \text{ KJ mol}^{-1}$					
T (K)	$[G^0(T)-H^0(298)]/T$ JK ⁻¹ mol ⁻¹	ln Q Fit	C _p Fit JK ⁻¹ mol ⁻¹	$[H^0(T)-H^0(298)]\text{Fit}$ KJ mol ⁻¹	$\Delta G_f^0(T)$ KJ ⁻¹ mol ⁻¹
600.0	450.0	-2.22654E+02	-1.96492E+02	-4.18624E+02	1377.76
1000.0	510.0	-8.76575E+01	2.48971E+02	-3.69541E+02	1216.62
2000.0	620.0	2.10979E+01	1.65496E+02	-1.65293E+02	820.16
3000.0	690.0	6.11844E+01	3.06264E+02	5.48397E+01	453.31
4000.0	750.0	8.41495E+01	4.15464E+02	4.37877E+02	76.52
5000.0	805.0	1.00163E+02	7.44302E+00	7.13547E+02	-325.15
6000.0	840.0	1.10605E+02	-1.42778E+03	1.10408E+02	-658.70
Partition Function Fit $\ln Q = L_1 + L_2 \ln T - L_3/T + L_4/T^2 + L_5T + L_6T^2 + L_7T^3$ L ₁ = -1.83308E+03 L ₂ = 2.71180E+02 L ₃ = -2.03945E+04 L ₄ = -3.02675E+07 L ₅ = -1.32798E-01 L ₆ = 1.57129E-05 L ₇ = -8.65216E-10					

Table 2. Comparison of PSI and Sandia Thermochemical Data

Molecule: C_6H

$\Delta H_f(298) \text{ kJ mol}^{-1}$	
PSI	Sandia
1255.2	891.93

PSI		Sandia	
T (K)	$[G^0(T)-H^0(298)]/T$ $\text{JK}^{-1} \text{ mol}^{-1}$	T (K)	$[G^0(T)-H^0(298)]/T$ $\text{JK}^{-1} \text{ mol}^{-1}$
200	3.16600E+02	298	310.102
298	3.08780E+02	300	310.104
400	3.12420E+02	400	313.899
600	3.27650E+02	500	321.473
800	3.44510E+02	600	330.391
1000	3.60540E+02	700	339.707
1200	3.75350E+02	800	349.003
1400	3.88990E+02	900	358.085
1600	4.01580E+02	1000	366.866
1800	4.13210E+02	1500	405.910
2000	4.24010E+02	2000	438.110
2200	4.34090E+02	2500	465.306
2400	4.43500E+02	3000	488.772
2600	4.52330E+02	3500	509.364
2800	4.60620E+02	4000	527.679
3000	4.68480E+02	4500	544.157
3200	4.75930E+02		
3400	4.82960E+02		
3600	4.89700E+02		
3800	4.96100E+02		
4000	5.02210E+02		
4200	5.08060E+02		
4400	5.13670E+02		
4600	5.19070E+02		

Table 3. Comparison of PSI and Sandia Thermochemical Data

Molecule: C₈H

$\Delta H_f(298) \text{ kJ mol}^{-1}$	
PSI	Sandia
1425.02	1208.72

PSI		Sandia	
T (K)	$[G^0(T) - H^0(298)]/T$ $\text{JK}^{-1} \text{ mol}^{-1}$	T (K)	$[G^0(T) - H^0(298)]/T$ $\text{JK}^{-1} \text{ mol}^{-1}$
600	3.80000E+02	298	328.053
1000	4.30000E+02	300	328.055
2000	5.20000E+02	400	332.744
3000	5.80000E+02	500	342.186
4000	6.30000E+02	600	353.393
5000	6.70000E+02	700	365.173
6000	7.10000E+02	800	376.984
		900	388.565
		1000	399.795
		1500	450.001

discrepancy in the free energy (Table 3). We expect our extrapolated results to become better as we go to higher carbon clusters. A better comparison to the Sandia fits would be plots of $\ln Q$, C_p , $H-H(298)$, and ΔG_f as a function of temperature which are readily generated.

2.3.4 When are the Large Molecular Clusters Important?

We examine under what conditions of T , P , and composition large carbon clusters are important. For definiteness we focus on C_{10} but other clusters have the same qualitative features. We then examine how $C_{10}H$ fares against C_{10} . We shall find that, most of the time $n_{C_{10}H}/n_{C_{10}} \ll 1$, and hence is usually not an important species under equilibrium conditions. The low temperature equilibrium is dominated by the largest cluster, while at higher temperatures there is a competition between the various carbon molecular species. We shall see we can stabilize to some extent the heavier molecules by constraining the equilibrium and/or varying the composition.

The temperature dependence of the mole fraction of C_{10} at 1 atm is shown in Figure 18 (solid curve) for graphite epoxy under pyrolysis conditions. [It is of interest to make similar plots for increasing cluster size to determine the temperature at which the most stable cluster disappears.] Above 4000 K there is virtually no C_{10} at equilibrium, while below this temperature, up to 3100 K, it is the dominant pure carbon molecular species. Above 3100 K C_3 becomes more dominant and eventually other molecular carbon species compete (see Figure 19). In Figure 20 the enthalpy is displayed: $H_{C_{10}}(T=500) = 14.35$ kJ/g, $H_{C_{10}}(T=3000) = 17.96$ kJ/g, which is substantially higher than what one would get if solid carbon were condensed (the stable phase under these

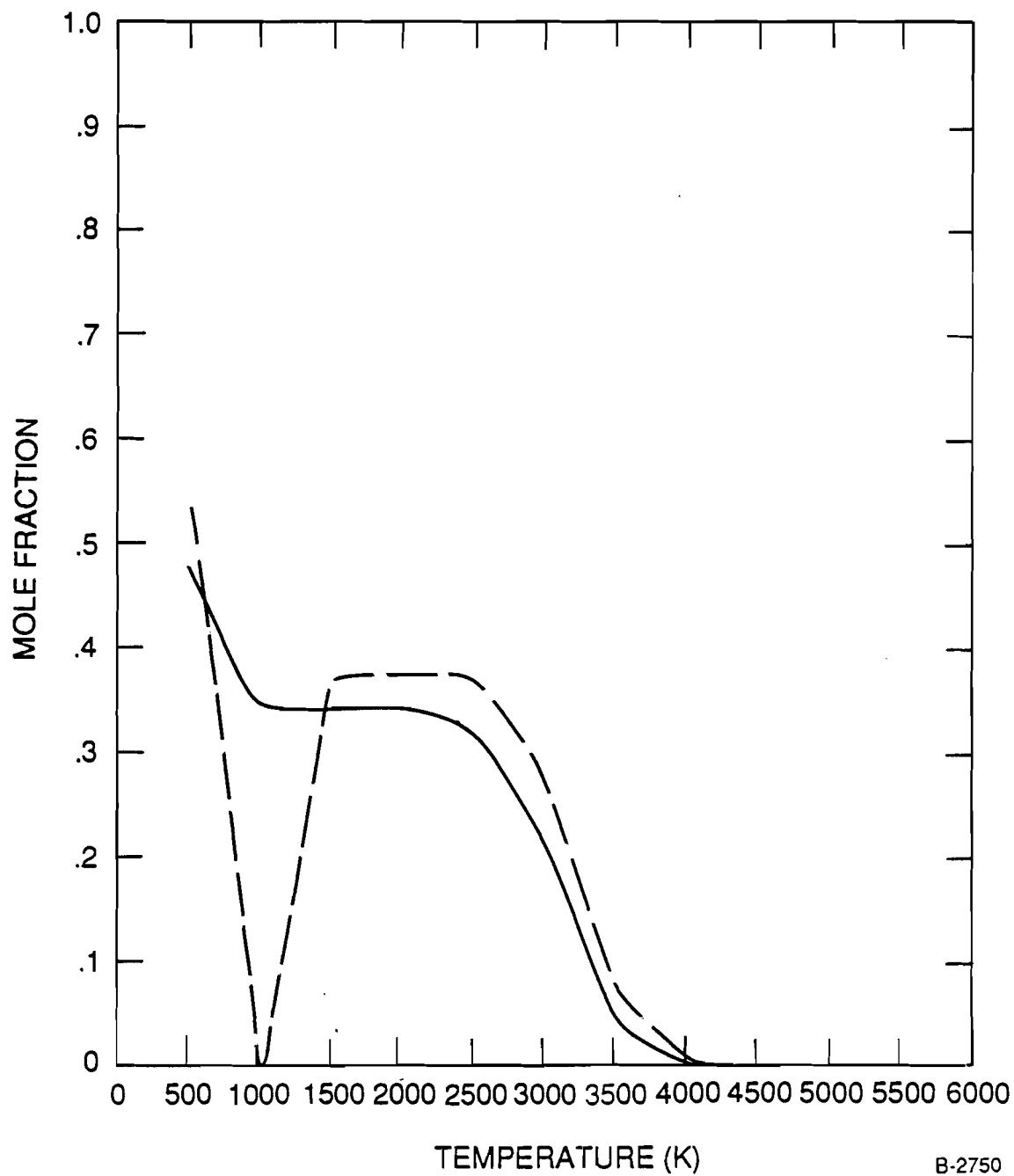
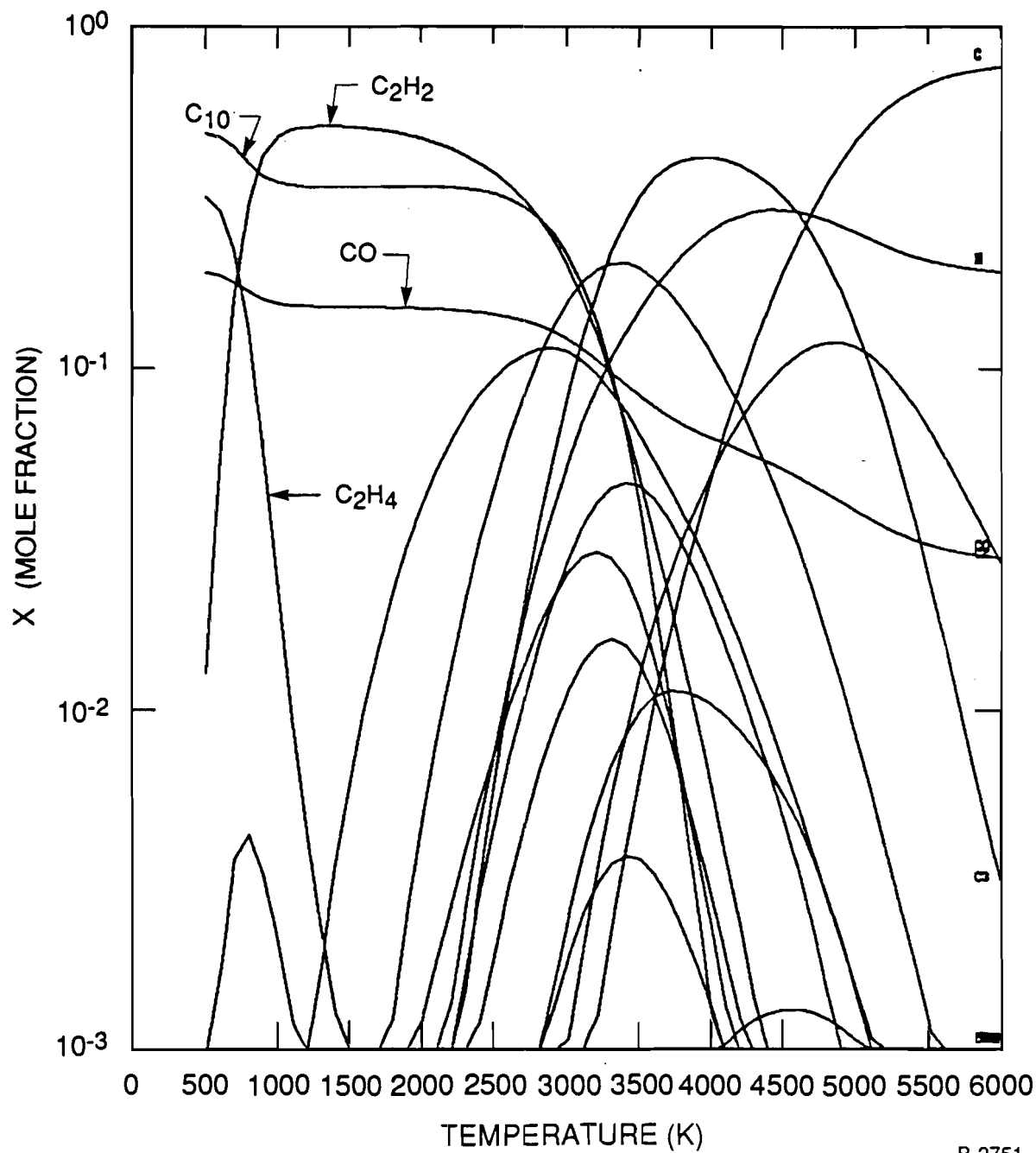


Figure 18.

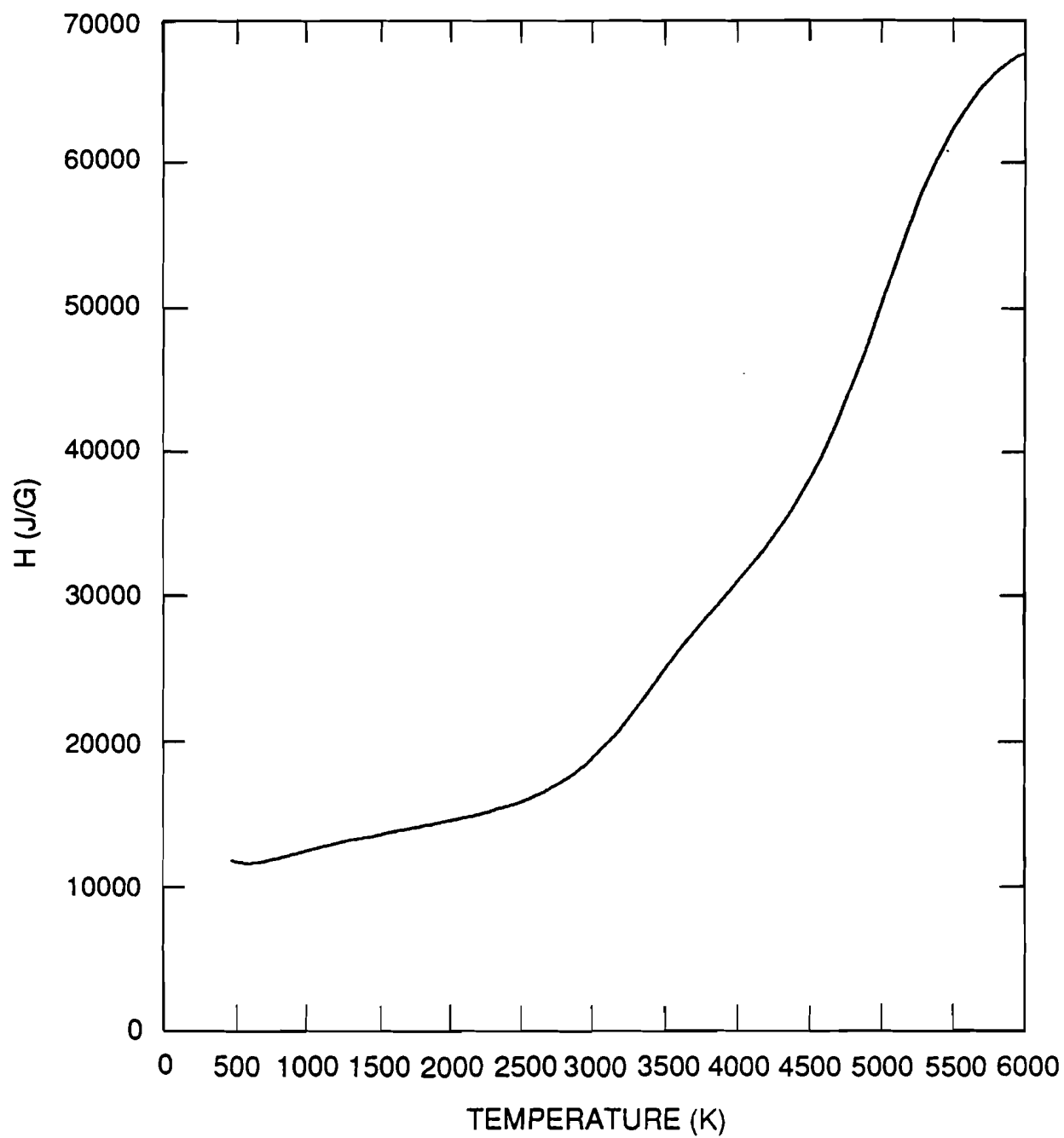
Mole Fraction of C_{10} at $P = 1$ atm in Graphite Epoxy under Equilibrium (Solid Curve) and Constrained Equilibrium (Dashed Curve)



B-2751

Figure 19.

Graphite Epoxy Equilibrium Composition (1 atm)



B-2752

Figure 20.

Graphite Epoxy Equilibrium Enthalpy (1 atm)

conditions) as is expected. Above 4000 K the enthalpy agrees with that of a previous report (Resendes, 1987).

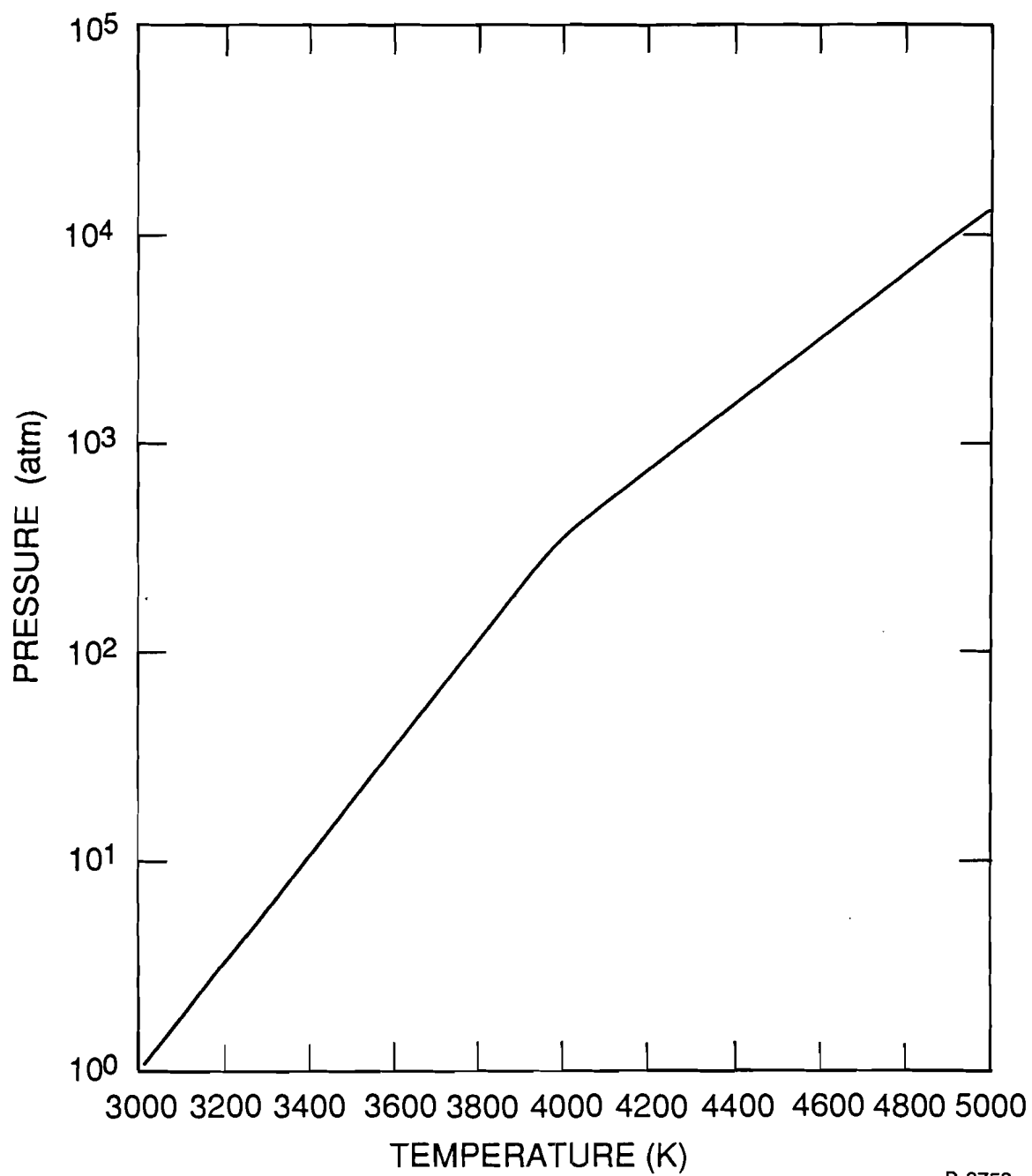
Let us now consider a fixed amount of C_{10} and study the pressure dependence of the vapor as we vary the temperature. We examine the equilibrium (any other equilibrium involving C_{10} is fine):



along with the consequent law of mass action which we write in the form:

$$\frac{n_{C_{10}}}{n_C} = \frac{P^9}{n_T} e^{-\frac{u_{C_{10}}^0(T) - 10u_C^0(T)}{RT}} \quad (2)$$

In Eq. (2) P denotes the total pressure in atms, subscripted u^0 the molar free energy and subscripted n the number of moles. Provided the total number of moles, n_T , does not change "much" with P and T any other equilibrium at a different P and T such that $n_{C_{10}}/n_C = \text{constant}$, necessarily has the same mole numbers. For the sake of calculation let us take $T = 3000$ and $P = 1$ atm where the mole fraction of C_{10} is approximately 20 percent, or $n_{C_{10}}/n_C = 632.3629$. Requiring approximately the same $n_{C_{10}}/n_C$ ratio at 4000 and 5000 K, we find the corresponding pressures using the previous equation. Note $n_T = 0.218442$ (from code output at 3000 K) and $R = 8.3144 \times 10^{-3}$ kJ/(mole K). Our results are plotted in Figure 21. Comparison of these number with the corresponding vaporization conditions of Ref. 3 shows that for $3000 < T < 5000$ there is a negligible mole fraction of C_{10} under vaporization conditions. It also indicates that if we are to see a significant amount of C_{10} (≈ 20 percent mole fraction) at these temperatures the pressures are extremely high.



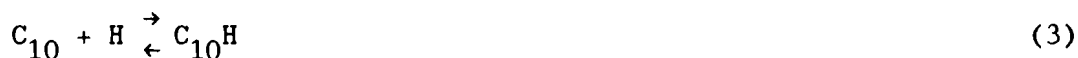
B-2753

Figure 21.

Pressure Dependence on Temperature for 20 Percent Mole Fraction of C_{10}

To see the effect of constrained equilibrium on the presence of large clusters we refer to Eq. (2) and note that the total number of moles n_T appears in the denominator raised to the ninth power. This indicates that if we constrain the equilibrium by not allowing the smaller species to appear this will reduce n_T thereby increasing $n_{C_{10}}/n_C$. To illustrate the effect we will not allow C, CH, CH₂, CO, OH, HCO, C₂H. The implication is that at the beginning of the laser pulse when the smaller species are practically non-existent due to kinetic limitations, there should be more C₁₀ present than an equilibrium calculation indicates. Figure 18 (dashed curve) gives the results of such a calculation. It is interesting to note the lack of C₁₀ (in favor of CH₄) at 1000 K. It is not clear whether this represents a real physical effect; thermodynamically CH₄ is favored over C₁₀. Note for example that at 3000 K the constrained run has an almost 30 percent increment of C₁₀ relative to the non-constrained run.

We want to compare the relative abundances of C₁₀H and C₁₀. Our starting point is the law of mass balance for the equilibrium reaction:



which we write in the form:

$$\frac{n_{C_{10}H}}{n_{C_{10}}} = P e^{\frac{u_H^0}{RT}} \left(\frac{n_H}{n_T} \right) \quad (4)$$

[We are considering here a non-constrained equilibrium.] Since our normalization is such that $n_T \leq 1$, $n_H/n_T < 1$ always. $u_H^0 > 0$ at low T when n_H is small and $u_H < 0$ at high T when n_H is large with the result that (at constant

pressure) $n_{C_{10}H}/n_{C_{10}} \ll 1$. The remaining molecules C_6H and C_6 , C_8H and C_8 follow the same trend.

Lastly, we consider the effect of modifying the C/H/O ratios on the previous results. We do this by working with an epoxy rather than a graphite epoxy. From Eq. (4), the $n_{C_{10}}/n_C$ ratio will be favored in epoxy versus graphite epoxy if n_T for the same P , T and equilibrium species is lowered in the epoxy relative to the graphite epoxy. A code calculation shows that n_T in epoxy is, in fact, higher than in graphite epoxy so that $n_{C_{10}}(\text{epoxy})/n_{C_{10}}(\text{g.e.}) < 1$. However, n_H is higher in epoxy so that $n_{C_{10}H}/n_{C_{10}}(\text{epoxy}) > n_{C_{10}H}/n_{C_{10}}(\text{g.e.})$.

2.3.5 Conclusion

In general, what we find is that at a given pressure the higher molecular C species are favored at low temperatures. If the pressure is increased they can be condensed out. Changing the composition from carbon fiber poor to fiber rich favors high molecular carbon formation. These conclusions present no surprises. Interesting effects arise from constraining the equilibrium which is a limited form of kinetics modeling. It was found that the presence of high molecular carbons could be enhanced by disallowing the formation of smaller chemical species. However, one can find regions (in P , T space) where this is not the case (recall Figure 18). Under vaporization conditions the amount of C_{10} present is negligible. Also the ratio C_nH/C_n for large n is always much less than one. All this leads to the conclusion that knowledge of the chemical distribution as well as P , T , time histories are necessary for a proper calculation of the chemical contribution to Q^* . It is also clear that extrapolation of the type that was done here for higher molecular clusters will yield the same qualitative results.

3. PLUME DEBRIS/BEAM INTERACTION

The interaction of the beam with gas and particulate phase debris is potentially important in scaling Q^* with spot size. The particulates are studied in detail in Subsection 3.1 and are potentially capable of scattering the beam and increasing Q^* by an order of magnitude. Similarly, gas phase absorption studies are discussed in Subsection 3.2 in order to assess Q^* increases and plasma ignition with spot size.

3.1 Scattering by Particulates

The previous FELS program identified that a few percent of the mass removed from a target was present in submicron particles which scattered both the 1.06 μm beam and the 6328Å HeNe probe beam. The HeNe probe beam experienced attenuation at intensities as low as 100 kW/cm² whereas the Q^* measurements suggested that scattering is not affecting the transmission of the 1.06 μm beam to the target at intensities below 1 MW/cm². An analysis of single and multiple scattering was initiated to resolve this issue. The updated results and conclusions are reported below.

The most important single scattering parameter is the opacity τ of the particulates in the plume flowfield. The opacity is calculated from the total column density M_{CW} of mass above the target

$$M_{CW} = \frac{\bar{I}_s D_s}{V Q_s^*} ,$$

where \bar{I}_s is the average intensity on the spot diameter D_s , V is the velocity of the particles (10^4 cm/s), and Q_s^* is the value of Q^* in the absence of plume absorption or scattering (30 kJ/g). If mass fraction f of M_{CW} is broken into N

resin fragments of density ρ (1.25 g/cc) and radius a , the optical opacity (τ) becomes

$$\tau = N\sigma_s = \frac{3f \bar{I}_s D_s}{4 \rho V Q_s^*} \left(\frac{\sigma_s}{\pi a^3} \right) ,$$

where σ_s is the optical cross section of a particle of radius a . The optical cross sections are obtained from Mie code calculations and are illustrated in Figure 22. The cross sections are functions of the particle size and laser wavelength. For submicron particles, the cross sections (hence the opacities) for the HeNe are three times that of the 1.06 μm beam.

$$\tau_{\text{HeNe}} \approx 3 \tau_{1.06}$$

This important distinction between the HeNe and 1.06 beams was overlooked in the FELS program and is rectified below.

Rewriting τ_{HeNe} as

$$\tau_{\text{HeNe}} = K_{\text{max}} f D_s \bar{I}_s ,$$

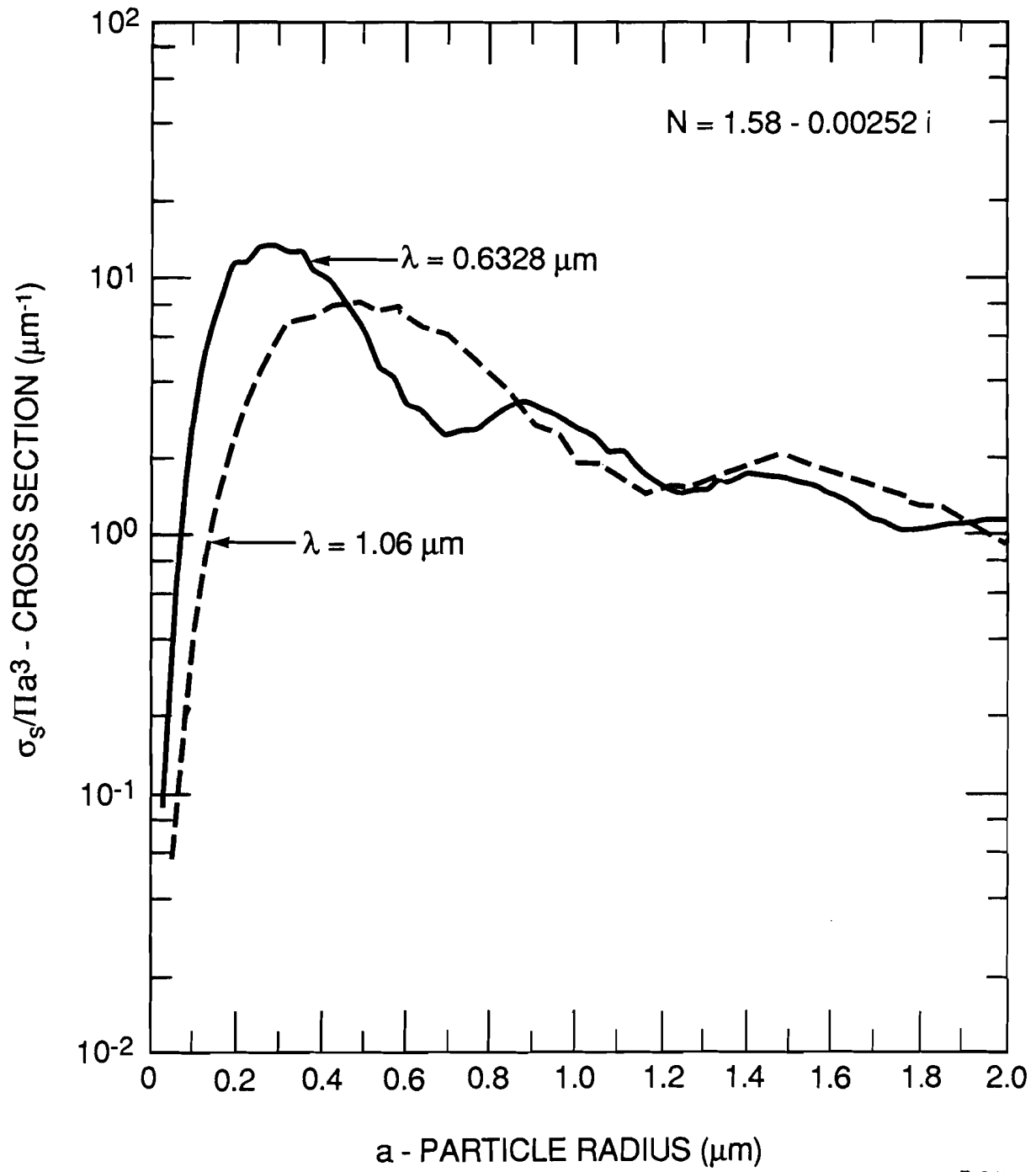
the maximum attenuation occurs when

$$K_{\text{max}} = \frac{3(\sigma_s / \pi a^3)}{4 \rho V Q_s^*} = 3 \times 10^{-4} \text{ cm/W}$$

corresponding to

$$\frac{\sigma_s}{\pi a^3} = 14 \mu\text{m}^{-1}$$

for submicron ($a = 0.3 \mu\text{m}$) particles.



B-2450

Figure 22.

Cross Section per Unit Volume

The HeNe detector has a narrow field of view and any photons scattered by particles will never be scattered back on to the detector. The HeNe transmission T_{HeNe} is therefore statistically related to the opacity by

$$T_{\text{HeNe}} = \exp(-\tau_{\text{HeNe}}) \quad .$$

A typical HeNe transmission plot is illustrated in Figure 23 for a CW pulse at 124 kW/cm² on material 130 using a 0.8 cm diameter spot. A HeNe transmission of 90 percent is consistent with the above analysis if $f = 0.03$, i.e., if 3 percent of the mass is in submicron particulates. While submicron particles have been observed, no quantitative measurement supports this requirement. It is worth noting that an 8 to 10 percent mass loading is required to explain the HeNe data for material 110.

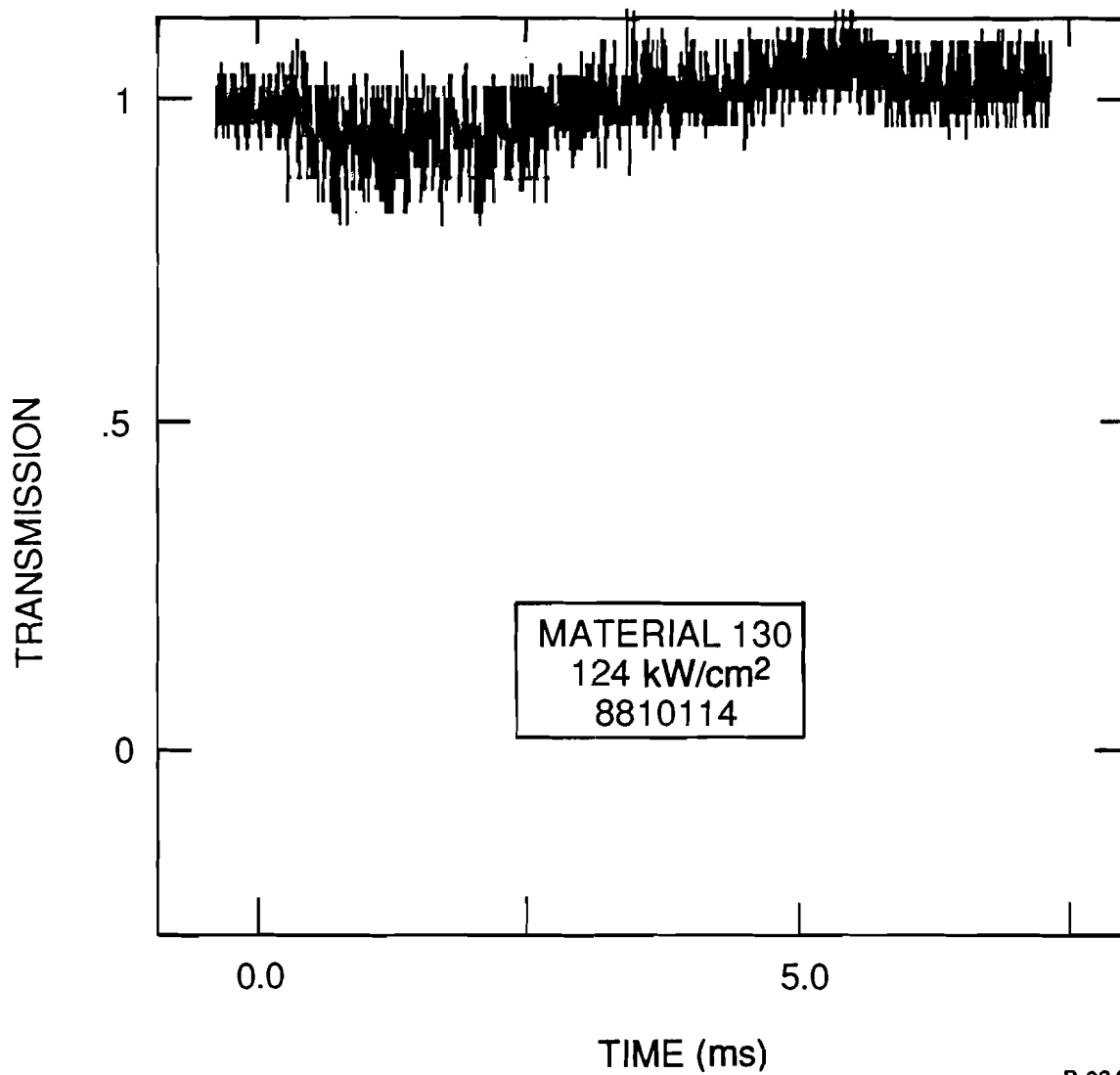
While these same particles are scattering the 1.06 μm beam, the target will have a larger "collection angle" than did the HeNe detector. A two flux (forward and reverse) model for multiple scattering (Simons et al., 1989) yields the beam transmission T_B

$$T_B = \frac{1}{1 + \sigma \tau_{1.06}} \quad (5)$$

where σ is the backscatter coefficient (fraction of intensity \bar{I} backscattered per scattering event). Since the onset of the HeNe attenuation occurs at an order of magnitude lower intensity than does the onset of the beam (Q^*) attenuation, it must follow that

$$\sigma \tau_{1.06} = \frac{1}{10} (\tau_{\text{HeNe}})$$

for all intensities \bar{I}_S . When the distinction between $\tau_{1.06}$ and τ_{HeNe} was not considered, we were led to the erroneous conclusion that $\sigma = 0.1$. However, with the knowledge that for submicron particles,



B-0849

Figure 23.

HeNe Transmission for Material 130 at 124 kW/cm²

$$\tau_{\text{HeNe}} = 3 \tau_{1.06} ,$$

it follows that the required value of σ is $\sigma = 0.3$, and is confirmed below using a Monte Carlo scattering code.

The Monte Carlo scattering code determines the fractional penetration of laser light through a cloud of scattering particles. The code is one-dimensional inasmuch as no variation in the particle density of the cloud is assumed in the directions parallel to the surface. Given this fact, the variation normal to the surface is also irrelevant; only the total density of scattering particles per unit area is significant (e.g., if the cloud is twice as thick but half as dense, the rays will travel twice as far between collisions, but the net penetration will be the same). The rays are traced using three-dimensional ray tracing techniques, converting to multi-dimensions would not be a problem.

The code works by tracing probabilistic paths of many light rays and noting the fraction that penetrate the particle cloud. The incident laser radiation is taken to be normal to the surface. A ray is assumed to move a randomly picked distance chosen such that a large number of numerical rays will statistically have the same falloff with distance as would the laser light. Since the unscattered radiation will fall off exponentially as $\exp(-x/\text{mfp})$, the travel distance is chosen to be $\text{distance} = -\text{mfp} \cdot \ln(1.0 - \text{ran})$, where ran is a random number between 0 and 1 and mfp is the mean free path.

Upon collision, the ray is scattered or absorbed. The fraction of rays absorbed will be $\Sigma_a / (\Sigma_s + \Sigma_a)$, and is played for randomly. Here Σ_s is the macroscopic scattering cross section and Σ_a is the macroscopic absorption cross

section. The scattered rays are redirected randomly in a manner consistent with the differential scattering cross sections of the scattering particles.

The cross sections are determined by calling a Mie scattering subroutine. For a given size particle with given real and imaginary refractive indices, the routine determines the absorption and scattering cross sections and the probabilities of different scattering angles. For a situation in which the cloud consists of particles of many sizes, the routine is called a number of times to compute the cross sections for particles in a number of size bins, and the overall absorption, scattering, and differential scattering cross sections per unit volume are computed.

A ray is traced until it is absorbed or leaves the cloud, either by penetrating to the surface or by scattering away. The ray is then scored as one of four categories:

- 1) Absorbed by the cloud,
- 2) Scattered away by the cloud,
- 3) Penetrating the cloud without scattering, or
- 4) Scattered but eventually penetrating the cloud.

The fraction of light in each of these categories is computed by dividing the rays in each bin by the total number of rays traced. A significant number of rays must be traced to give good statistics. The uncertainties scale as the square root of the number of rays. For example, if 1000 rays are traced and 10 percent penetrate (100 rays), then the standard deviation is 10 rays and the fraction penetration is between 9 and 11 percent to one standard deviation. No variance reduction procedure is used since for a simple problem like this the computation times are modest.

The beam transmission T_B versus the plume opacity $\tau_{1.06}$ is illustrated in Figure 24. The effect of particle size dominates the opacity $\tau_{1.06}$, but otherwise does not strongly influence the transmission. The Monte Carlo code clearly supports the two flux model (Simons et al., 1989) for $\sigma = 0.3$.

Using

$$\bar{I}_S = \bar{I} T_B ,$$

$\tau_{1.06}$ may also be rewritten as

$$\tau_{1.06} = K_O f D_S \bar{I} T_B \quad (6)$$

where K_O for submicron particles is

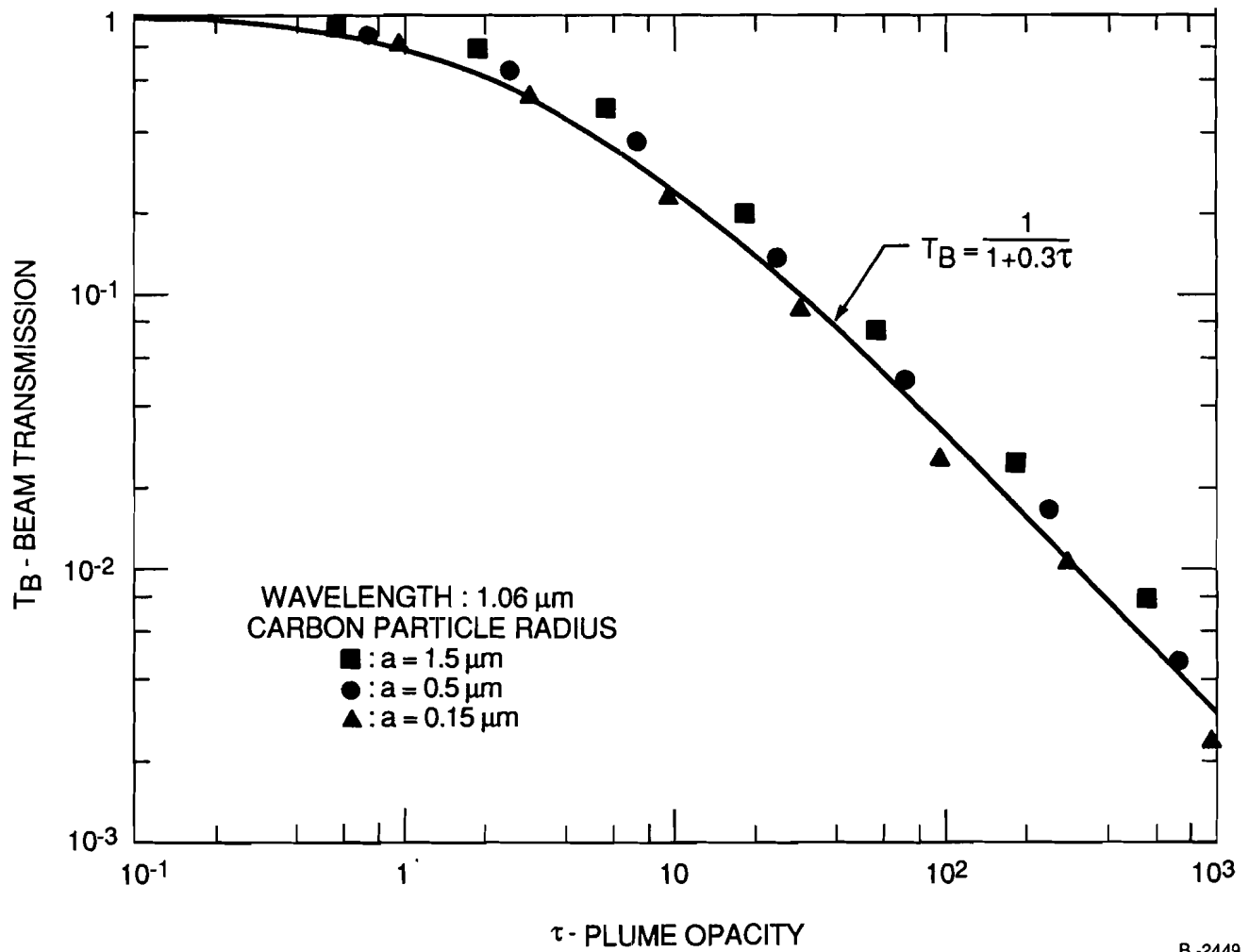
$$K_O = 10^{-4} \text{ W/cm}$$

such that $\tau_{1.06}$ remains 1/3 of τ_{HeNe} .

Solving Eqs. (5) and (6) for the beam transmission in the large attenuation limit, we obtain

$$T_B = \frac{1}{\left(\sigma K_O f D_S \bar{I} \right)^{1/2}} \leq 1 .$$

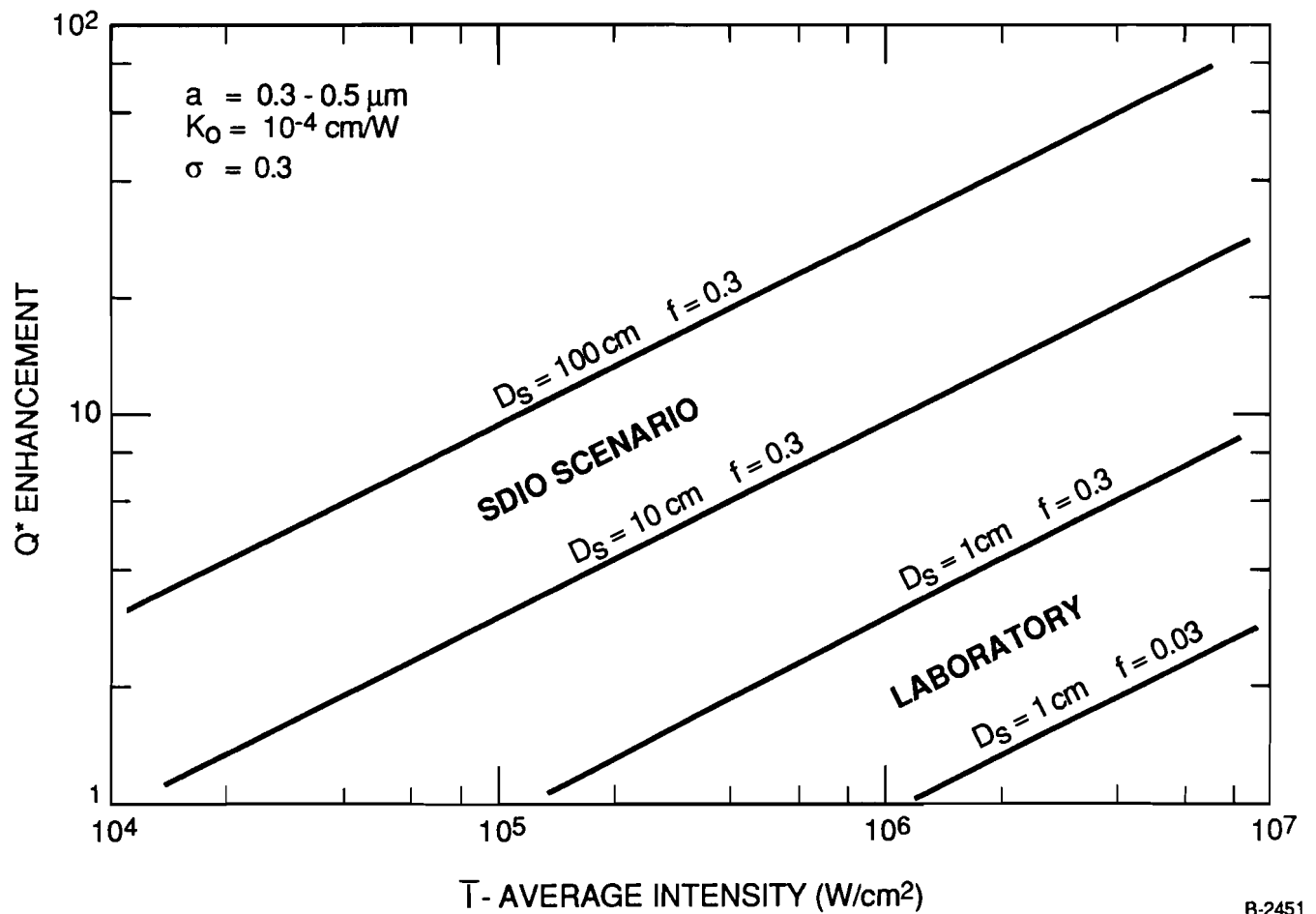
Since Q^* is Q_S^*/T_B , we illustrate the role of scattering through the enhancement of Q^*/Q_S^* . A typical composite must produce 3 percent ($f = 0.03$) of the mass loss in submicron fragments in order to explain the HeNe transmission data. Figure 25 illustrates that for $f = 0.03$ in the laboratory ($D_S = 1 \text{ cm}$), intensities of a few megawatts are required to observe an increase in Q^* due to scattering. If the composite were constructed with 30 percent of the mass in submicron scatterers, then laboratory measurements ($D_S = 1 \text{ cm}$, $f = 0.30$) would observe a significant Q^* enhancement at intensities of one megawatt. Similar materials in the robust SDIO scenario ($D_S = 10 \text{ to } 100 \text{ cm}$) would experience an order of magnitude enhancement in Q^* . Hence, the issue of scattering has an



B-2449

Figure 24.

Scattering Cloud Transmissivity



B-2451

Figure 25.

Q^* Enhancement via Scattering

important impact on the use of lasers in the robust SDIO scenario and laboratory data at a few MW/cm² is required to further support these conclusions.

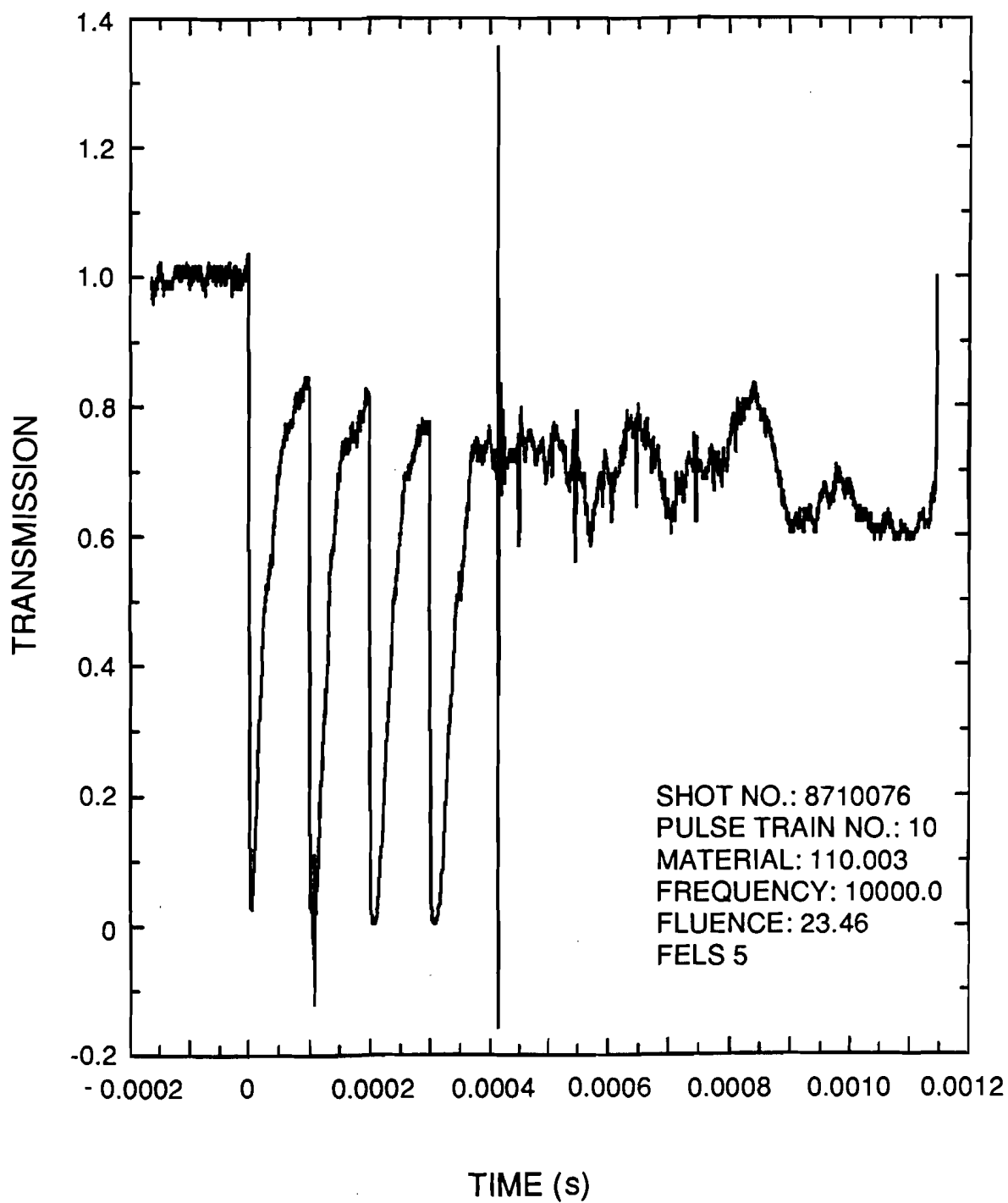
The above analysis was carried out for a CW plume. Plumes generated in the laboratory may be distinctly different in the RP and CW modes. For sufficiently short pulses, debris leaves the surface in a "shell" with velocity V ($V \sim 10^4$ cm/s). The distance the shell travels between pulses at rep rate f is V/f and the number of shells in spot size D_s is $D_s f/V$. Hence, when $D_s f/V \gg 1$, the rep pulse plume will look like a CW plume.

Typical laboratory experiments are conducted on a 1 cm spot at 10 kHz (i.e., $D_s f/V = 1$) and will clearly demonstrate a rep pulse behavior. This is demonstrated with a HeNe probe beam transmission plot illustrated in Figure 26. The transmission is unity in the absence of any debris plume. At $t = 0$, a single pulse reduces the transmission to zero. The transmission recovers in time as the flow expands and achieves a value of 0.8 when a second pulse again reduces it to zero. The process continues until a repetitive, periodic flowfield is established where transmission varies between some minimum value just after the pulse to some maximum value that will be seen by the pulse.

The time evolution of the opacity generated in the rep pulsed mode at frequency f may be expressed (Simons, et al., 1989) as

$$\tau(t) = \sum_{j=0}^M \frac{\tau_0}{\left(1 + \frac{V}{D_s} \left(t - \frac{j}{f}\right)\right)^2}$$

where $M + 1$ is the total number of laser pulses, each of which generates an identical shell of debris with initial opacity τ_0 . This expression satisfactorily explains the typical transmission versus time relationship



B-0777

Figure 26.

FELS-5 HeNe Transmission for Material 110

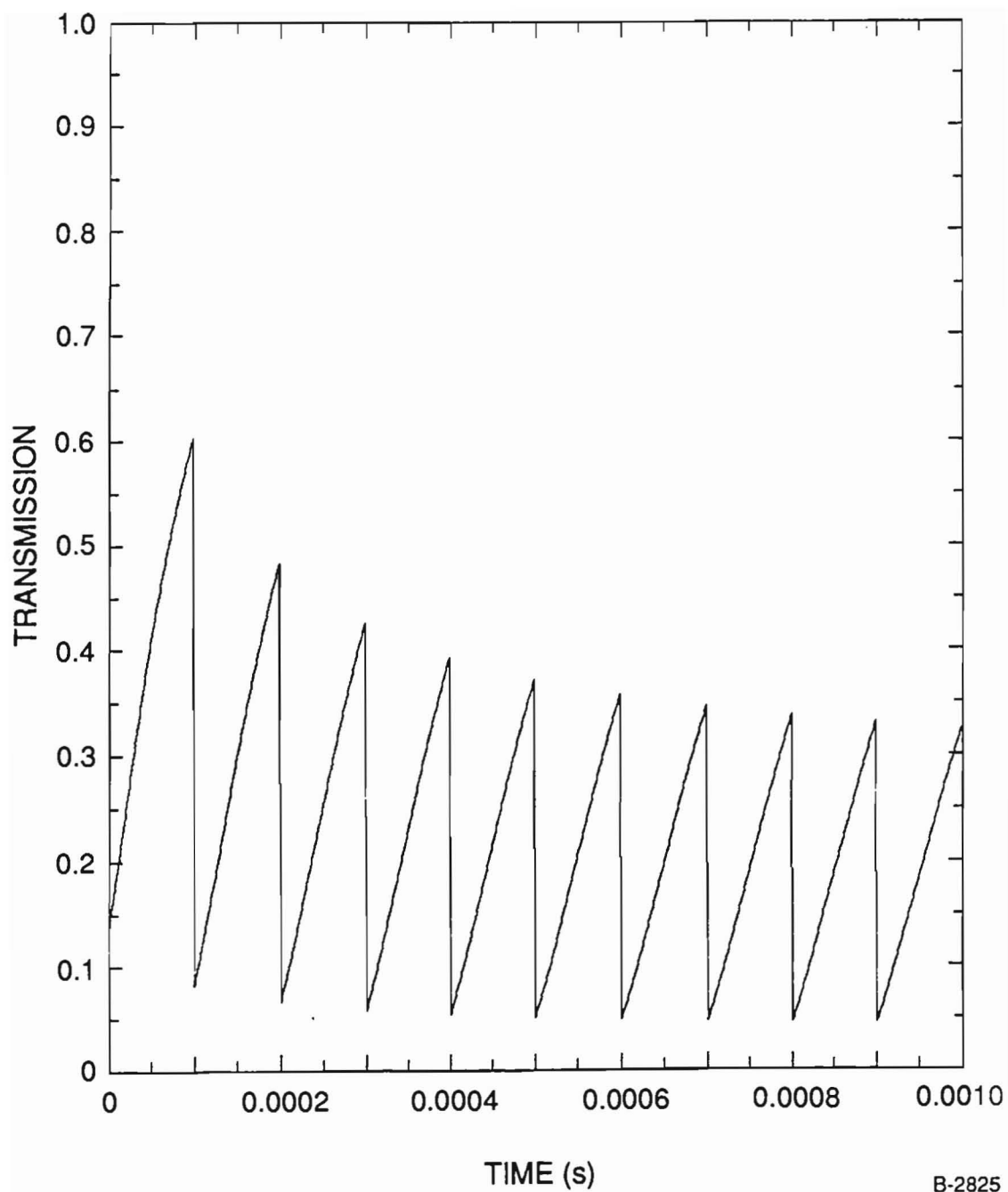
observed experimentally and is used below to assess the similarity between RP and CW plumes on large laser spots, i.e., when $D_S f/V \gg 1$.

We wish to compare the various RP modes at fixed average intensity. Hence, when f is increased by a factor of three the corresponding pulse fluence and corresponding initial opacity τ_0 must be reduced by a factor of three. Holding D_S and V fixed at 1 cm and 10^4 cm/s respectively, we compare predicted HeNe probe beam transmissions in Figures 27 to 29 for rep rates of 10, 30, and 90 kHz respectively. The corresponding values of τ_0 were chosen to be 2, 0.66667 and 0.22222. These calculations clearly demonstrate the RP behavior when $D_S f/V = 1$ and a CW like behavior for $D_S f/V = 9$. Thus, the predictions and conclusions associated with Figure 25 above apply to a RP mode as well as a CW mode provided the spot size and rep rate satisfy $D_S f/V \geq 10$.

3.2 Gas Heating from Laser Absorption

3.2.1 Introduction

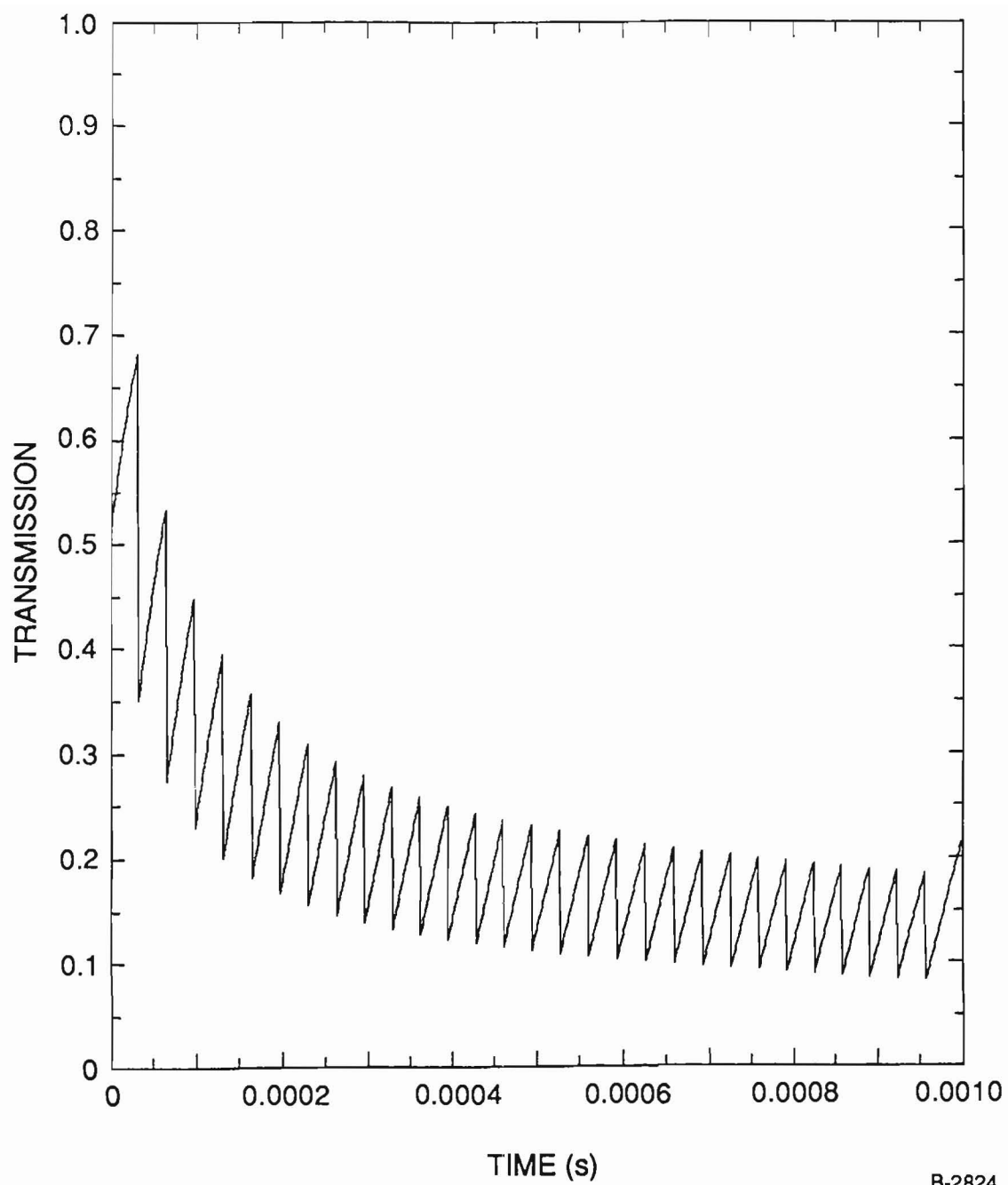
In the previous report (Simons, et al., 1989, Subsection 3.3) we pointed out the importance of gas heating when the ablation plume absorbs the laser energy, as well as showing that the rapid ablation of target material at high irradiances will produce a large density of ablation products in the plume in front of the target. In this high density plume, gas absorption will increase Q^* , the energy to ablate one gram of material. The most important consequence of the plume heating is that the increased temperature gives a higher electron concentration, and the higher electron concentration gives increased absorption via the inverse bremsstrahlung processes, which leads to a thermal runaway that produces a plasma. As plasma production causes a large increase in Q^* , we see



B-2825

Figure 27.

Probe Beam Transmission for $D_S f/V = 1$



B-2824

Figure 28.

Probe Beam Transmission for $D_S f/V = 3$

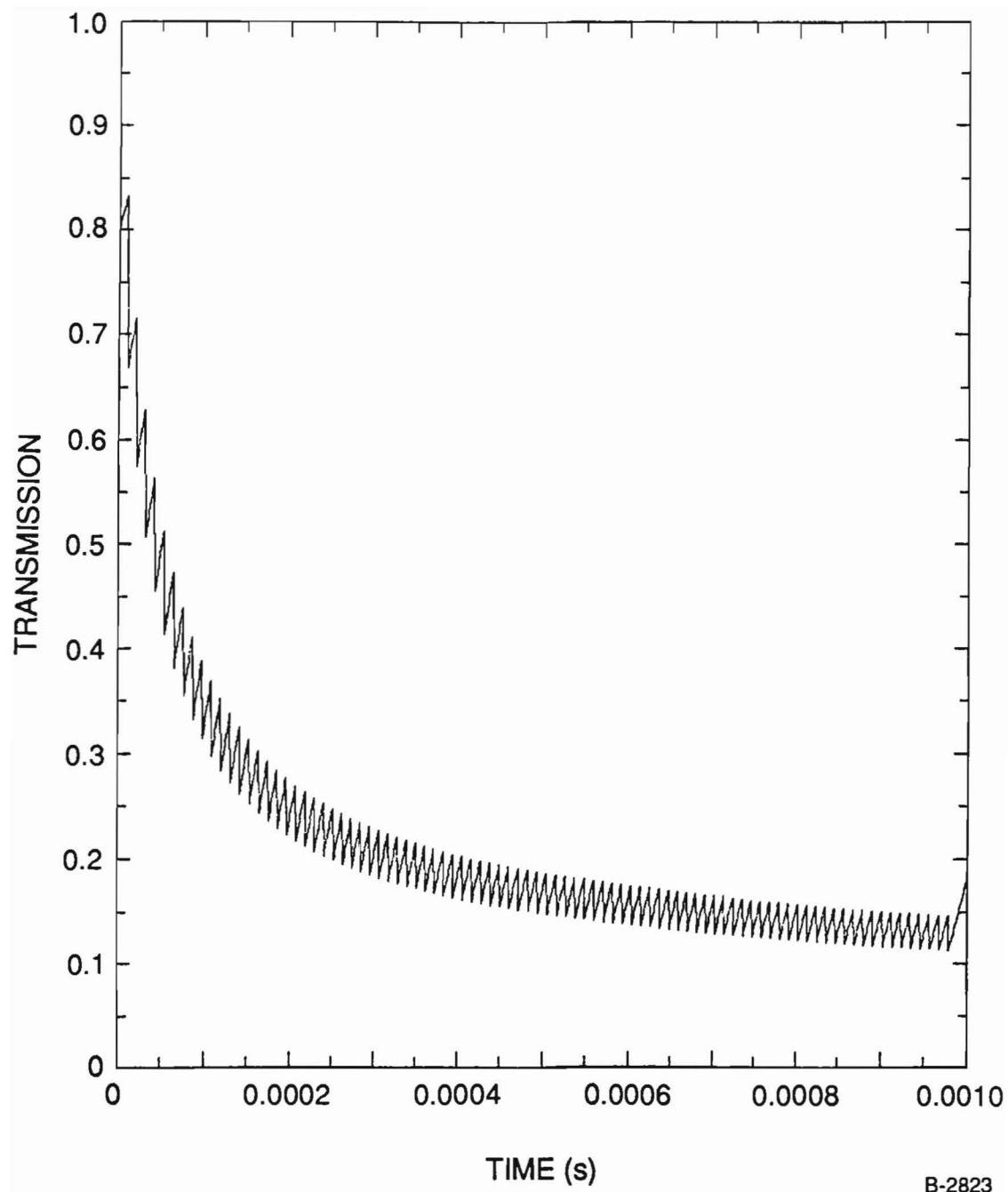


Figure 29.

Probe Beam Transmission for $D_S f/V = 9$

that it is important to understand when plume absorption leads to plasma production.

A major issue is whether the ablated species absorb the laser light. That is, do they have states with excitation energies corresponding to the energy of the laser photons. Multiple-photon effects, where multiple photons are absorbed at the same time, will be important when the I values are large enough, but we ignore these and only consider single-photon processes. Atomic species will only have a small number of transitions from low-lying states at wavelengths near $1.06\text{ }\mu\text{m}$, and thus are less likely to absorb than are molecular species, by which we mean both stable molecules and radicals. In the 0.4 to $1.06\text{ }\mu\text{m}$ region, absorption can excite electronic, vibrational, and/or rotational states. Most electronic states have higher energies that require radiation with shorter wavelengths than $1.06\text{ }\mu\text{m}$, and the large absorption cross sections for vibrational transitions are at longer wavelengths. The absorption lines have finite widths, and high pressure will broaden the lines. Absorption in the wings of broadened lines can be an important absorption mechanism. Thus the ability to propagate laser light efficiently through gaseous ablation products depends on whether the products absorb the laser radiation and on the fate of the absorbed energy.

3.2.2 Self-Consistent Calculation of Gas Heating by Laser Absorption

In the previous report we presented expressions to calculate the average number density n_t in the gaseous plume. Here we shall restate these expressions in order to explain how we have solved the several equations self-consistently to predict the temperature of the plume. This solution is an approximation where we consider the gas in the region of one-dimensional (1-D)

flow near the ablating surface. Here we solve for the pressure and temperature of a mixture of ideal gases in the approximation that the pressure and temperature are uniform over the region from the edge of the Knudsen layer to the end of the region of 1-D flow, that the thickness of the 1-D region is increasing at the sonic velocity, and that the species concentrations are always at their equilibrium values. The input parameters include the incident laser irradiance I_0 for the CW case ($I_0 = F_p/\tau_p$ for pulsed operation), and spot diameter D , as well as the elemental composition of the ablating material, the absorptivity of the surface α , and the absorption cross sections σ of the major absorbing species in the plume. The solution is iterated until the temperature and pressure in the uniform plume are consistent with the amount of energy absorbed in the plume and at the target surface.

The rate of material ablated from the target can be estimated using the heat of ablation H_A (J/g) calculated for equilibrium from the amount of energy absorbed per unit area as

$$dm/dt = \alpha I_S/H_A \quad . \quad (7)$$

Here dm/dt is the time derivative of the mass removed per unit area, evaluated after passing through the Knudsen layer where we assumed that the directed velocity is sonic after the Knudsen layer. Thus dm/dt is evaluated from the equilibrium vapor pressure calculation as described in our previous report (Simons, et al., 1989, Appendix A). In the above, α is the fraction of the surface irradiance I_S that is absorbed at the target. The density of material in the gas ρ (assuming all products are gaseous) is given by

$$\rho = (dm/dt)/u_g = \alpha I_S/(u_g H_A) , \quad (8)$$

where u_g is the flow velocity, which we take to be sonic, so that

$$u_g = (\gamma R_g T/\langle M \rangle)^{0.5} = 9.82 \times 10^5 (\gamma T/\langle M \rangle)^{0.5} \text{ cm/s} , \quad (9)$$

where R_g is the gas constant, T is the temperature (Kelvin), γ is the ratio of heat capacities c_p/c_v , and $\langle M \rangle$ is the average molecular weight.

The fraction f_A of the incident irradiance that is absorbed by the a mixture of gaseous ablation products is determined by the total absorption cross section σ_t , the total number density n_t , and the path length L_{1D} as

$$f_A = I_S/I_0 = \exp(-\sigma_t n_t L_{1D}) , \quad (10)$$

where I_0 is the incident irradiance. The σ_t is the sum of the neutral average absorption cross section $\langle \sigma \rangle$ and the cross sections from the two inverse bremsstrahlung processes of electron-neutral, with cross section σ_{ibn} , and electron-ion, with σ_{ibi} . The average $\langle \sigma \rangle$ is determined from the absorption cross sections σ_i of the different species and the mole fractions x_i as

$$\langle \sigma \rangle = \sum \sigma_i x_i , \quad (11)$$

and

$$\begin{aligned} \sigma_t = [& \langle \sigma \rangle n_t + \sigma_{ibn} (1 - x_e) x_e n_t^2 + \sigma_{ibi} x_e^2 n_t^2] \\ & \times [1 - \exp(-E_p/T_e)] , \end{aligned} \quad (12)$$

where the second term in brackets corrects for stimulated emission, E_p is the photon energy (1.165 eV), and T_e is the temperature in eV. Here, x_e is the mole fraction of electrons, which we assume to equal the mole fraction of ions, and

$$n_t = \rho N_A/\langle M \rangle , \quad (13)$$

where N_A is Avogadro's number (6.02×10^{23} molecules/mole) and

$$\langle M \rangle = \sum x_i M_i , \quad (14)$$

where M_i is the molecular weight of species i .

The effective thickness (i.e., the path length) of the one-dimensional region of the ablation plume for short pulse times τ_p can be estimated as

$$L_{1D} = u_g \tau_p , \quad \tau_p < 0.55D/u_g , \quad (15a)$$

when the pulse time is short enough that the expansion is one-dimensional. For long pulse times, the expansion become three-dimensional and the value of L_{1D} depends on the diameter of the illuminated target. As discussed in our previous report (Simons, et al., 1989), Bailey found that the true (ρL) product integrated over the distance from the target can be approximated by the ρ from Eq. (8) times a characteristic length given by

$$L_{1D} \approx 0.55D , \quad \tau_p > 0.55D/u_g , \quad (15b)$$

where D is the diameter of the laser beam at the target surface.

In order to include the absorption by inverse bremsstrahlung processes, we need the electron density, n_e , and values for the absorption cross sections.

We use the Saha equation to find the mole fraction of electrons, $x_e = n_e/n_t$, as

$$x_e = [6.04 \times 10^{21} (1 - x_e) n_t (g_1/g_0) T^{1.5} \exp(-I_{pe}/T_e)]^{0.5}/n_t , \quad (16)$$

For our calculations, we take $g_1/g_0 = 6/9$ and $I_{pe} = (11.26-1.17)$ eV, values that are appropriate for atomic carbon, although they do not change much when we consider the C_n or C_2H species. Note that we use an effective ionization potential I_{pe} that is reduced from I_p by the value of one-photon of energy. This is to account for the rapid ionization expected at high pressures for any species excited to within 1.17 eV of its ionization potential.

We find the cross section σ_{ibn} for the electron-neutral inverse bremsstrahlung process by interpolation among the results calculated for

different λ and T for atomic carbon by Geltman (1973). For example, at 5000 K, $\sigma_{ibn} = 1.23 \times 10^{-39} \text{ cm}^5$ at $\lambda = 1.0 \text{ } \mu\text{m}$ and $T = 5000 \text{ K}$. We compute the cross section σ_{ibi} for the electron-ion inverse bremsstrahlung process from the Kramers formula times the Gaunt factor $\langle g_{ff} \rangle$ as

$$\sigma_{ibi} = (4/3)[2 \pi / (3 m k_B T)]^{0.5} [z^2 e^6 / (h c m v^3)] \langle g_{ff} \rangle ,$$

or

$$\sigma_{ibi} = 1.27 \times 10^{-37} \lambda^3 z^2 \langle g_{ff} \rangle / T_e^{0.5} \text{ cm}^5 , \quad (17)$$

where z is the charge of the ion, and the constant is for λ given in μm and the temperature T_e in eV. For our case of initial plasma formation, $z = 1$. We find $\langle g_{ff} \rangle$ by interpolating between values given as a function of variables determined by λ and T at $z = 1$ (Karzas and Latter, 1961-2). As $\langle g_{ff} \rangle$ is on the order of one and σ_{ibi} is around 100 σ_{ibn} , both processes contribute when x_e is greater than 0.01 or so.

The final step in the calculation is to find the new temperature from the increase in enthalpy when the gas absorbs energy. The increase in enthalpy of the gas from absorption of a constant fraction f_A of the incident irradiance I_0 over a time Δt is $f_A I_0 \Delta t$. The mass of gas in the plume is $\alpha(1-f_A)I_0 \Delta t / H_A$, so that the enthalpy change per unit mass is

$$\Delta H_g = [f_A / (1 - f_A)] H_A / \alpha .$$

When the energy in the directed flow is subtracted, this becomes

$$\Delta H_g = [f_A / (1 - f_A)] (H_A / \alpha) - u_g^2 / 2 . \quad (18)$$

The total enthalpy of the gas is then $\Delta H_g + H_A$. We then use the results of equilibrium thermochemical calculations that give H_g as a function of T and the pressure p .

When the procedure finds self-consistent values for p , T , x_i , etc., then the amount of material ablated is consistent with the absorption in the plume,

and the temperature in the plume is consistent with the energy absorbed there. The iteration proceeds as shown in Figure 30. The procedure converges quickly when $f_A < 0.2$ or so, especially if the absorption is primarily by the neutral species. At high absorption via inverse bremsstrahlung, the procedure may not converge. Therefore, we somewhat arbitrarily declare plasma formation under conditions where the temperature is increasing and f_{Aib} is substantial.

3.2.3 Absorption Line Width Estimation

The importance of absorption by isolated lines depends on the absorption width of the lines and on the number density of the absorber. As we are primarily interested in plasma initiation, where the electron number density is low, we ignore the line broadening from the Stark effect. This leaves three sources of line broadening: natural, Doppler, and collisional. The natural width is determined by the lifetime of the upper state via the Heisenberg uncertainty principle. A lifetime of 5×10^{-10} s corresponds to a width of 0.01 cm^{-1} , which is small. Thus lifetime broadening is only important when the lifetime is shorter than 10^{-10} s. The Doppler half width is determined by the frequency of the radiation and the velocity, which is a function of the temperature and the mass,

$$\gamma_D = 3.58 \times 10^{-8} \nu (T/M)^{0.5} , \quad (19)$$

where ν is the frequency (in cm^{-1}) of the transition, T is the temperature (Kelvin), and M is the gram molecular weight. The collisional or Lorentz broadening is a function of the collision cross section and the number density. Thus the Lorentz half width is given by

Begin at Low Irradiance

Given: F_p , τ_p , I_0 , D , $\sigma_i(T,p)$

Preliminary Calculation of $H_A(\alpha I_S)$, $H_g(T,p)$,
and $x_i(T,p)$ from Elemental Composition of Target

Initially Assume: $x_e = 0$, use T and p for Target Surface at I_0

- [1] Find $\langle M \rangle$ and γ at equilibrium for given T , p from $x_i(T,p)$ tables.
Evaluate

$$\langle \sigma \rangle = \sum \sigma_i x_i, \quad (11)$$

$$\sigma_t = [\langle \sigma \rangle n_t + \sigma_{ibn} (1 - x_e) x_e n_t^2 + \sigma_{ibi} x_e^2 n_t^2] \times [1 - \exp(-E_p/T_e)] \quad (12)$$

- [2] Find n_t by iteration of

$$f_A = I_S/I_0 = \exp(-\sigma_t n_t L_{1D}), \quad (10)$$

$$n_t = \alpha I_0 (1 - f_A) N_A / (\langle M \rangle u_g H_A), \quad (7)+(8)+(13)$$

until n_t consistent with f_A .

- [3] Update the inverse bremsstrahlung absorption by finding a new x_e from

$$x_e = [6.04 \times 10^{21} (1 - x_e) n_t (g_1/g_0) T^{1.5} \exp(-I_{pe}/T_e)]^{0.5/n_t} \quad (16)$$

- [4] Loop back to [2] to update the σ_t value using the new x_e and n_t to find the new σ_t using σ_{ibn} and σ_{ibi} at the current T . Stop loop when change in f_A is small.

- [5] Use f_A and H_A to find H_g .

- [6] Find new T from $H_g(T,p)$.

- [7] If $\Delta T > 0.5$ K, loop back to [1] using the new T .

- [8] If procedure converged, increment F_p and go to [1]. Use most recent values as initial values for next point.

Figure 30.

Iteration Procedure to Self-Consistently Solve for Plume
Temperature as a Result of Heating by Gas Absorption

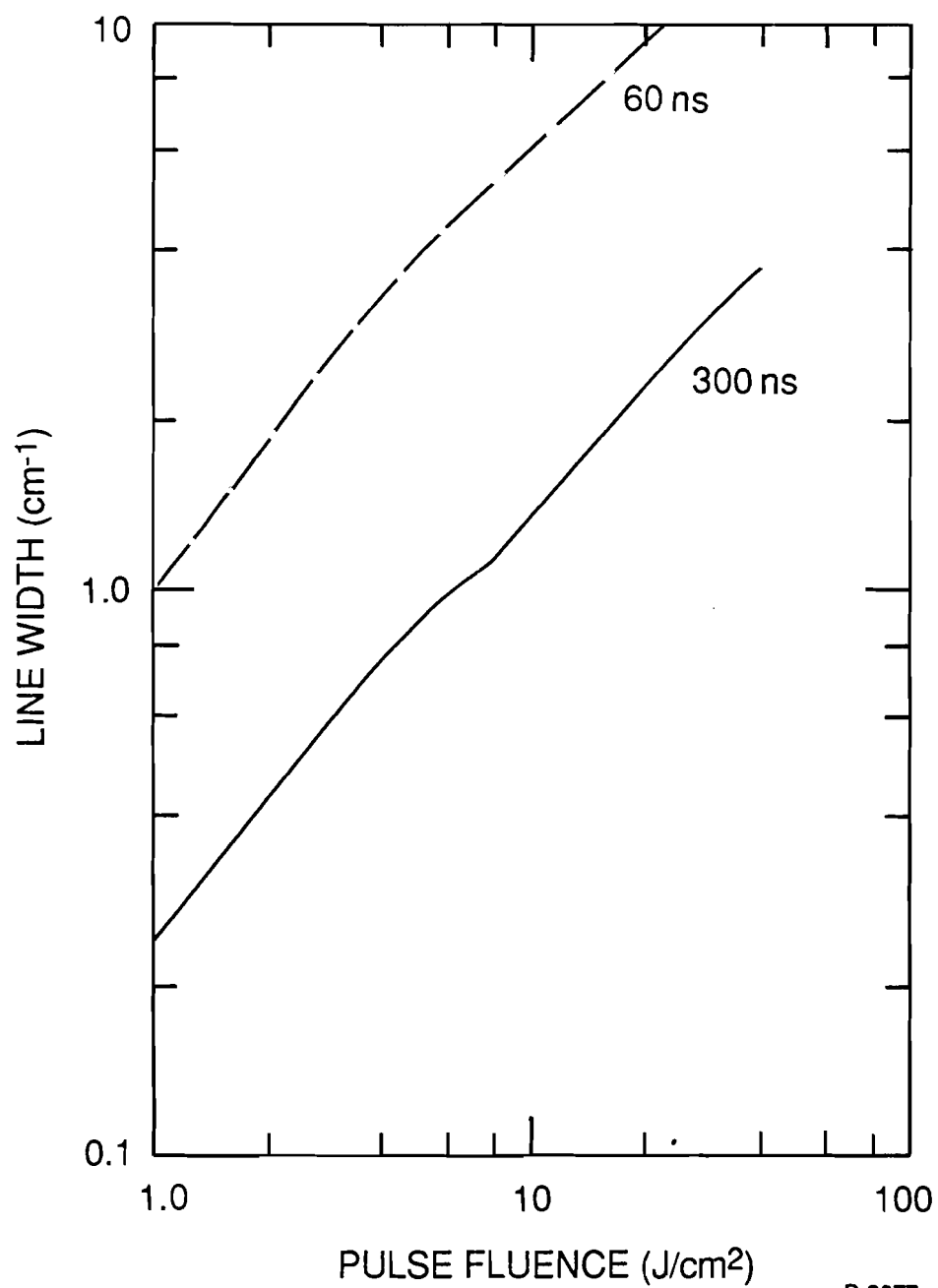
$$\gamma_L = \gamma_1 p (T/300)^{-m}, \quad (20)$$

where p is the pressure in atm and γ_1 and m depend on the collision cross section with typical values ca. $0.1 \text{ cm}^{-1} \text{ atm}^{-1}$ and 0.5 to 1.0, respectively. The number density above an ablating target surface is also a function of temperature, and Figure 31 shows combined effects of the Doppler and collisional half widths for a graphite epoxy target when $m = 0.7$ and $\gamma_1 = 0.1 \text{ cm}^{-1} \text{ atm}^{-1}$.

Molecular species have absorption bands that normally have many absorption lines to excite individual rovibrational levels in the bound, upper electronic state. These bands can also form a pseudocontinuum, and this is especially likely if the gas temperature is high so that many vibrational levels are populated. For example, the C_3 absorption from 370 to 490 nm studied at 3200 K had lines so closely spaced that they could not be resolved with a spectrograph resolution approaching the Doppler width of a single line (Brewer and Engelke, 1962). The pseudocontinua can be understood as the result of lines spaced more closely than their line width, and they can also occur in diatomic species when the pressure is high enough, as we show in the next subsection.

3.2.4 Calculation of C_2 Phillips Band System Spectrum

The C_2 radical has a number of electronic transitions that can be excited with photon energies near the 1.165 eV laser photon energy. For this diatomic radical, the absorption spectrum in the IR at low pressures will consist of a series of a lines representing transitions between specific states specified by their rotational, vibrational, and electronic quantum numbers. Therefore, the σ value at the laser wavelength will depend very strongly on the laser wavelength, as the σ will be large if the absorption line happens to overlap



B-2877

Figure 31.

Line Half Width as a Function of Pulse Fluence for a Graphite Epoxy Target with $\tau_p = 60$ and 300 ns

the laser line. As the pressure increases the linewidth, the absorption lines will overlap, and the dependence of σ on λ will be reduced. As we discussed previously (Simons et al., 1989, Subsection 3.3.8), the potential energy curves of C_2 show a ground state $X(^1\Sigma_g^+)$, which has an allowed transition with an excitation energy of 1.025 eV to the $A(^1\Pi_u)$ state. This transition is called the Phillips band system. In addition, there is another IR system, the Ballik-Ramsay system, with transitions from the lowest triplet states, the $a(^3\Pi_u)$ level at an excitation energy of 0.0756 eV relative to the ground state to the $b(^3\Sigma_g^-)$ level at an excitation energy (relative to the $a(^3\Pi_u)$ state) of 0.698 eV. There is another triplet system between the $c(^3\Sigma_u^+)$ level with a total excitation energy of 1.657 eV, which should have allowed transitions to the $d(^3\Pi_g)$ level located 0.821 eV higher. The possibility of several electronic transitions from states at energies of 0.076 to 1.66 eV gives a reasonable expectation that C_2 absorption can be important, especially when the pressure is high.

In this subsection we describe calculations of the C_2 absorption spectrum for one of the IR transitions, the Phillips band system ($X(^1\Sigma_g^+)$ to $A(^1\Pi_u)$). The calculation used a modification of the first part of the PSI spectral-fitting code. The input parameters for the code are the spectral constants for the upper and lower states, the Einstein A coefficients for the transitions between the various vibrational levels in the two electronic states, the temperature, and a specification of the line shape to be used. The calculations are for the $^{12}C_2$ isotopic molecule. We calculated the Einstein A coefficients for transitions between the vibrational quantum levels of $v'=0$ to 15 in the upper electronic state going to vibrational levels of $v''=0$ to 19 in the lower state.

This calculation requires values for the Franck-Condon factors $q_{v',v''}$ between the different vibrational wave functions, as well as the electronic transition moment R_e , because

$$A = \Sigma \langle R_e \rangle^2 [64\pi^4 / (3h\lambda^3)] [(2 - \delta_0, \Lambda' + \Lambda'') / (2 - \delta_0, \Lambda')] , \quad (21)$$

where h is the Planck constant and the second term in brackets is 2 for $\Sigma - \Sigma$ transitions, and 1 for other cases, as Λ' and Λ'' are the angular momenta of two electronic states (Whiting, et al., 1980; Schadee, 1978).

The calculation of the r -centroids and Franck-Condon factors necessary to evaluate the A coefficients used a modification of the PSI code that Marinelli used to calculate A factors for N_2 , which has been described previously (Marinelli and Piper, 1985). Rydberg-Klein-Rees (RKR) potentials were first calculated for both electronic states using the spectroscopic constants of Huber and Herzberg (1979), and the approach of Tellinghuisen (1974). This code was modified to fit the portion of the potential between the internuclear separations r at the classical turning points of the lowest vibrational state with a modified Morse potential. The potential used was that of Hulbert and Hirschfelder, as described in Herzberg (1950), which has the form

$$U(r) = D_e [(1 - e^{-\beta x})^2 + c\beta^3 x^3 e^{-2\beta x} (1 + b\beta x)] , \quad (22)$$

with

$$x = r - r_e$$

$$\beta = [2\pi^2 c\mu / (D_e h)]^{0.5} \omega_e$$

$$c = 1 - [1 + \alpha_e \omega_e / (6 B_e^2)] / (\beta r_e)$$

$$b = 2 - \{ (7/12) - [(5/4) + 5\alpha_e \omega_e / (12 B_e^2) + 5\alpha_e^2 \omega_e^2 / (144 B_e^4) - 2\omega_e x_e / (3 B_e)] / (\beta^2 r_e^2) \} / c . \quad (23)$$

Note the corrected sign for the second term of the expression for b in Eq. (23), which is discussed in Hulbert and Hirschfelder (1961). In the above,

r_e is the equilibrium internuclear separation, μ is the reduced mass, and B_e , α_e , ω_e , and $\omega_e x_e$ are spectroscopic constants. We did the fit of the negative and positive x values separately by adjusting the dissociation energy D_e so that U at the x -value of the classical turning point agrees with the potential from the RKR calculation.

The numerical eigenfunctions resulting from this procedure were then evaluated using the Numerov-Cooley procedure (Eccles and Malik, 1981) to solve the radial schrodinger equation. The overlap integrals in the r -centroid and Franck-Condon factor calculations were evaluated using simpson's rule. The results, which cover the range of v' and v'' from 0 to 19, are more extensive than other calculations (e.g., Cooper and Nicholls, 1976). We take the $\Sigma \langle R_e \rangle^2$ value to be $0.38(ea_0)^2$, where e is the electronic charge and a_0 is the Bohr radius, or $R_e = 1.567$ Debye. Cooper and Nicholls (1976) determined that $\Sigma \langle R_e / (ea_0) \rangle^2 = 0.36$ and 0.40 for the $\Delta v = 0$ and $+2$ sequences, respectively, while Brewer and Hagen (1979) quote two other sources as 0.48 and 0.50 for the $\Delta v = 0$ sequence. Our calculated $q_{v',v''}$ values agree rather well with those of Cooper and Nicholls in the region of overlap, e.g. for the 64 transitions they reported, 40 agree within 1 percent, only 11 have differences > 4 percent, and only 6 of these are > 10 percent.

Using the calculated A coefficients in the PSI spectral synthesis code, along with the spectral constants and the temperature, gives line strengths for the various rotational lines of each vibrational transition. Each contribution was summed over the line shape, which is assumed to be a Voigt profile. This line shape is the combination of the effects of Doppler and pressure broadening. The code calculates the power emitted in Watts per steradian per micron

value of the rotational temperature T_r . The power from each vibrational level is summed after weighting by the fractional population at T_r (i.e., the electronic and vibrational temperatures are assumed to be the same as the rotational temperature). The total power spectrum is then smeared over the finite linewidth of the Voigt profile. The result is the spectral radiance W_λ , the power radiated per wavelength interval at each wavelength by each molecule of C_2 at an equilibrium temperature of T_r . The absorption cross section per molecule is then obtained by noting that the absorptivity is related to the emissivity, and the emissivity for one molecule of C_2 is the ratio of the calculated spectral radiance to that radiated by a blackbody at the same temperature and wavelength, which is

$$W_{bb} = 3.745 \times 10^4 \lambda^{-5} \{ \exp[1.4388 \times 10^4 / (\lambda T)] - 1 \}^{-1} , \quad (24)$$

when λ is expressed in μm , T is in Kelvin, and W_{bb} is in $W/(cm^2 \mu m)$. That is, the absorption is related to the emissivity ϵ by

$$\epsilon = W_\lambda / W_{bb} . \quad (25)$$

and

$$\epsilon = 1 - \exp(-\sigma n L) = \sigma , \quad (26)$$

where the second equality in Eq. (26) considers that $\exp(-\sigma n L)$ is given by $1 - \sigma$ when we consider one molecule of C_2 .

Figure 32 shows the spectrum from 1.01 to 1.10 μm at $T = 5000$ K, which is a forest of closely spaced lines when the line width is small. This figure is for a pressure of 1 atm, and the line shape was calculated using Eqs. (19) and (20) with $m = 0.7$ and $\gamma_1 = 0.19 \text{ cm}^{-1} \text{ atm}^{-1}$. This value of γ_1 results from assuming that the appropriate collision cross section for the line broadening is the same as the cross section from viscosity studies. We take the cross

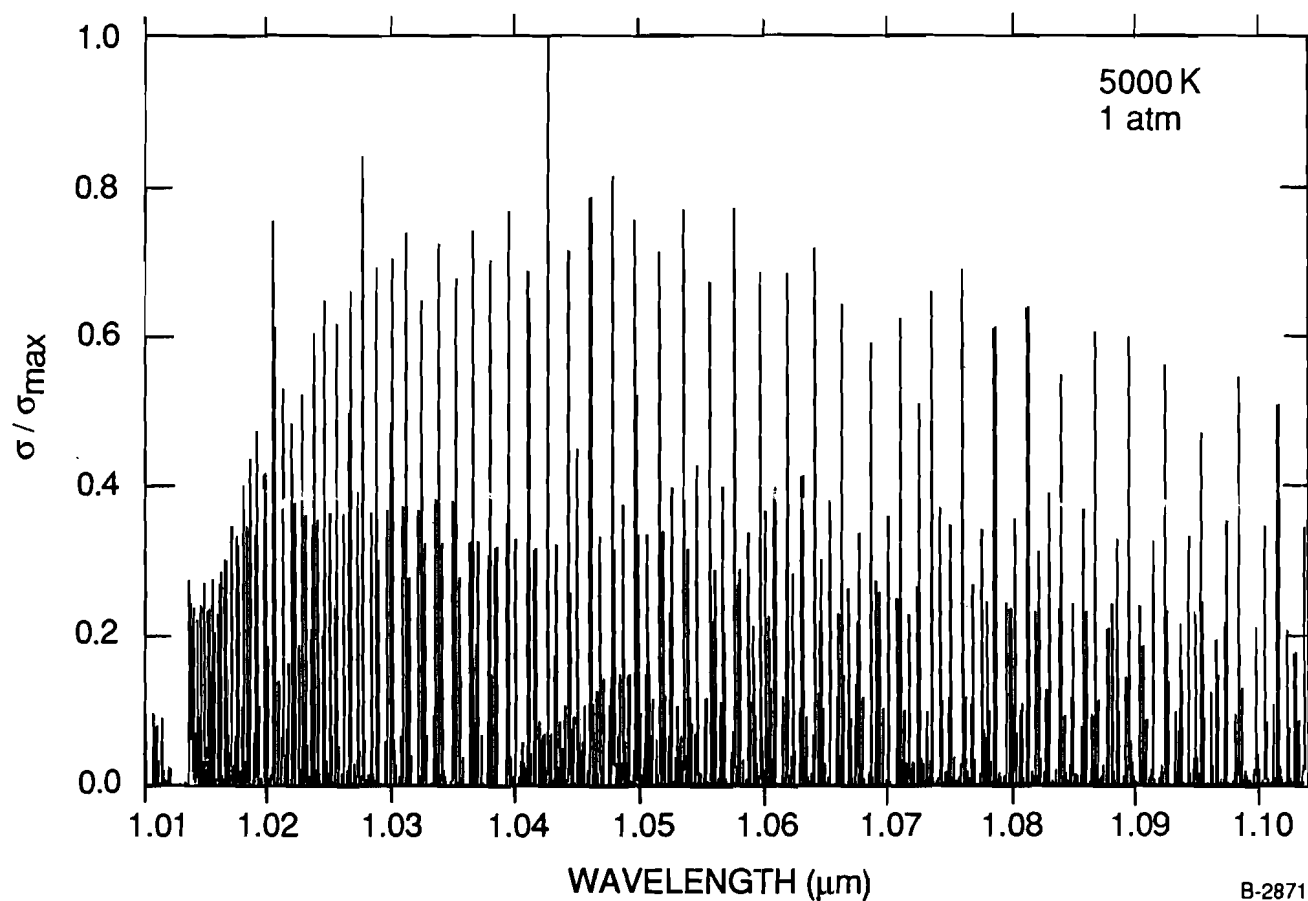


Figure 32.

Absorption Spectrum Calculated for $\text{C}_2 \text{X}(^1\Sigma_g^+)$ to $\text{A}(^1\Pi_u)$ from 1.01 to 1.10 μm . The calculation is for $T = 5000 \text{ K}$ and $p = 1 \text{ atm}$, and $\sigma_{\max} = 5.06 \times 10^{-16} \text{ cm}^2$

section as $(\pi/4)(\sigma_C + \sigma_{C_2})^2$, where σ_C and σ_{C_2} are the radii given by the Lennard-Jones parameters for C and C_2 (Svehla, 1962). The spectrum includes contributions from $v'' = 0$ to 19, going to $v' = 1$ to 15 in the upper state. Figure 33 shows the region from 1.06 to 1.07 μm on an expanded scale. This figure shows how increasing the pressure at $T = 6000$ K changes the spectrum from one of isolated lines at 1 atm, to lines that are slightly overlapping at 10 atm, to lines that are strongly overlapped at 100 atm, with the structure nearly gone at 300 atm. Figure 34 shows how increasing the pressure to 100 atm changes Figure 32. Thus, the modulation of the spectrum depends on the pressure. The structure of the spectrum does not depend very strongly on the temperature, as shown in Figure 35. This shows the spectra at $p = 10$ atm for $T = 4000$ and 7000 K, which have nearly the same structure in this region. The magnitude of σ at the particular value of $\lambda = 1.064$ μm is weakly dependent on temperature, and it does depend on the line width. This dependence is strong when the line half width is < 0.7 cm^{-1} , as shown in Figure 36. Here the different symbols represent T values from 4000 to 7000 K. The line width is primarily determined by the pressure, and 30 atm corresponds the half widths of 0.7 to 1 cm^{-1} . Figure 37 shows the data of Figure 36 plotted versus pressure. In summary, this calculation for σ ($\lambda = 1.064$ μm) gives values that are large and approximately independent of pressure for $p > 30$ atm, and σ increases with pressure at lower pressures.

3.2.5 Estimation of C_3 Absorption Spectrum

The C_3 radical is a major species in the equilibrium vapor above carbon-rich targets, as shown later in Figure 42. In our previous report (Simons, et al., 1989) we showed an extrapolation of the data of Brewer and Engelke (1962)

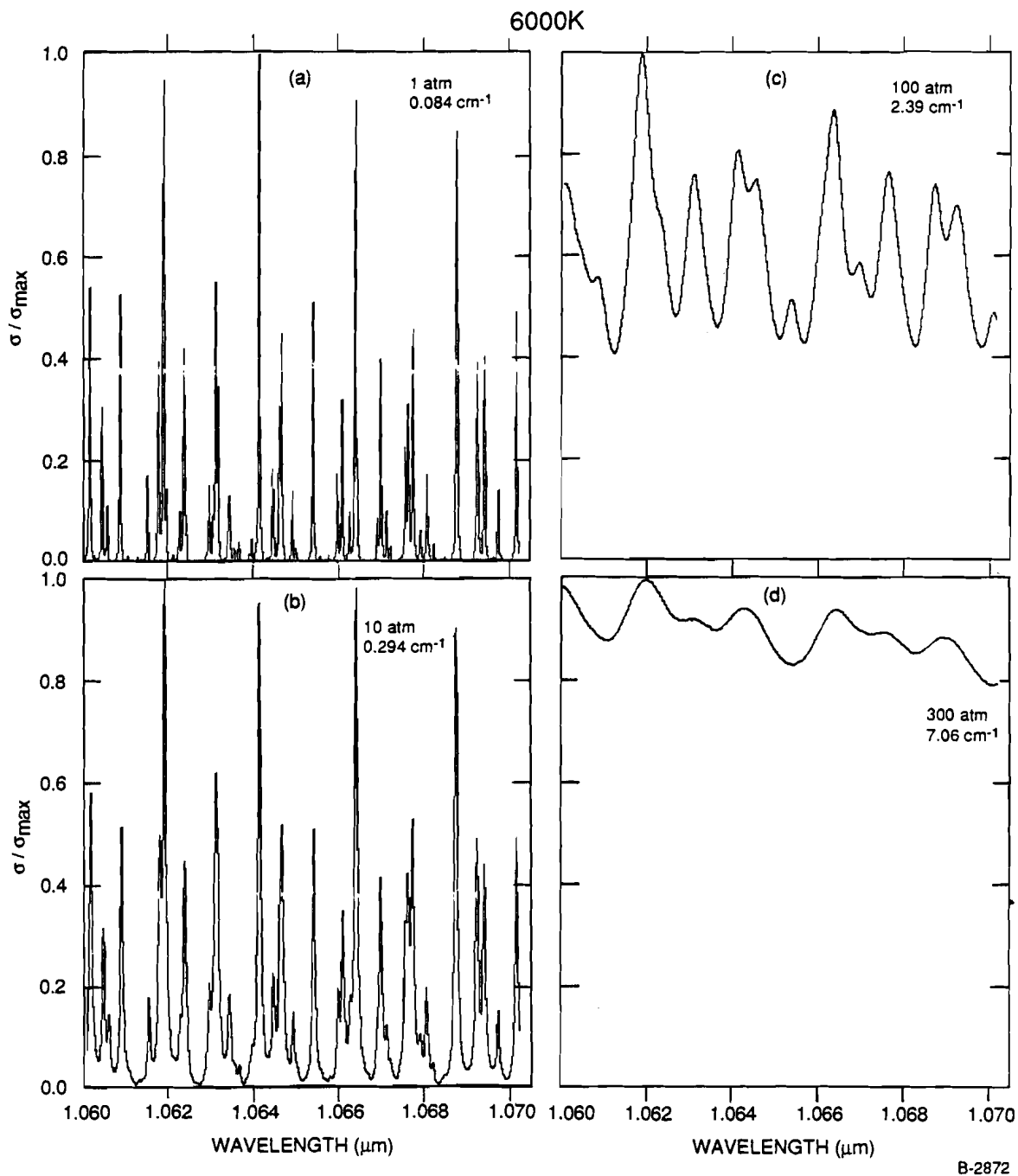


Figure 33.

Effect of Pressure on the Absorption Spectrum Calculated for $C_2 X(^1\Sigma_g^+)$ to $A(^1\Pi_u)$ from 1.06 to 1.07 μm at $T = 6000$ K. In parts (a) through (d), the pressure is 1, 10, 100, and 300 atm, $\nu_D + \nu_L$ is 0.0836, 0.294, 2.39, and 7.06 cm^{-1} , and σ_{max} is 33.2, 13.1, 3.09, and 2.10×10^{-17} cm^2 , respectively.

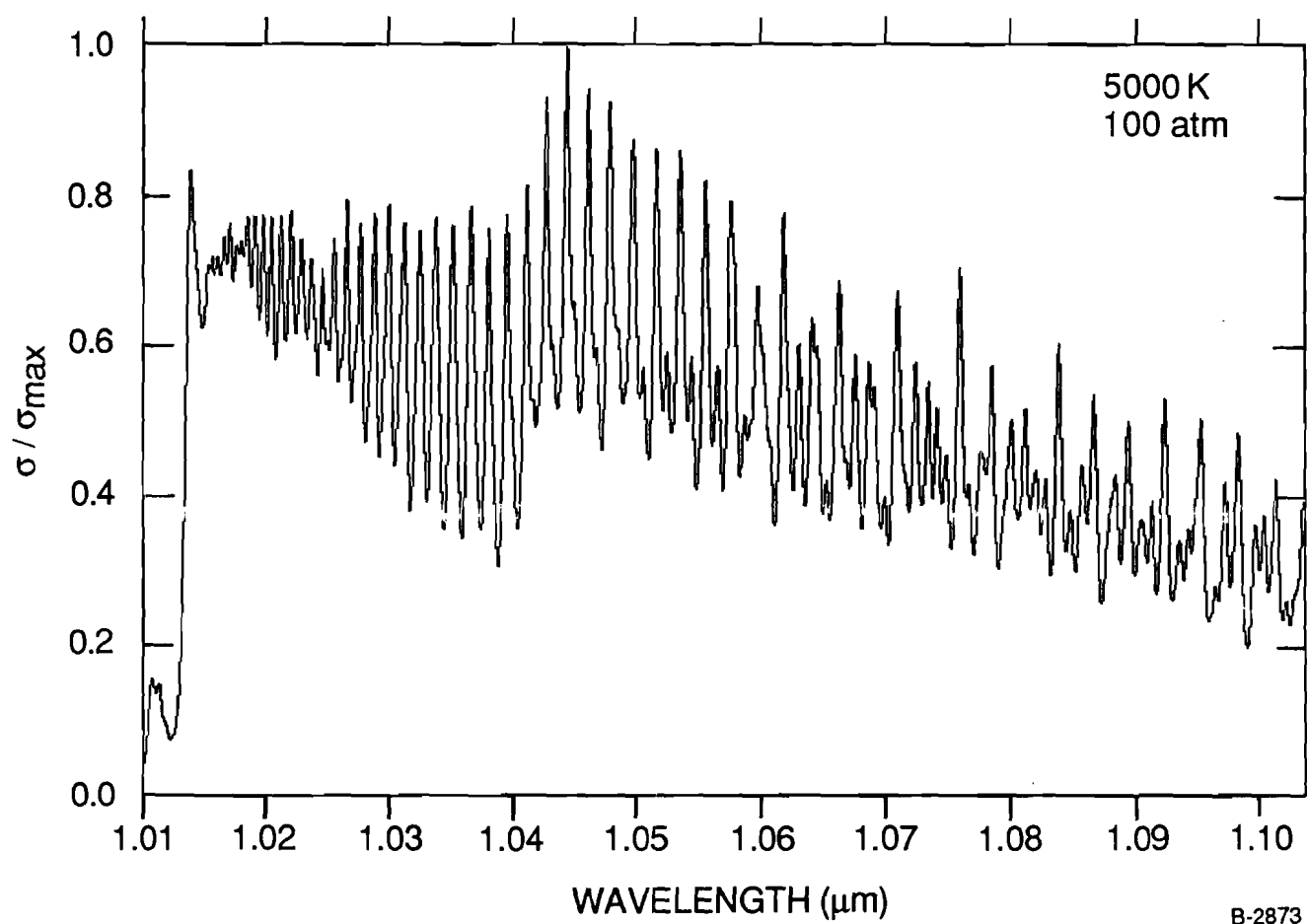


Figure 34.

Absorption Spectrum Calculated for $\text{C}_2 \text{X}(^1\Sigma_g^+)$ to $\text{A}(^1\Pi_u)$ from 1.01 to 1.10 μm .
 The calculation is for $T = 5000 \text{ K}$ and $p = 100 \text{ atm}$, and
 $\sigma_{\text{max}} = 3.74 \times 10^{-17} \text{ cm}^2$.

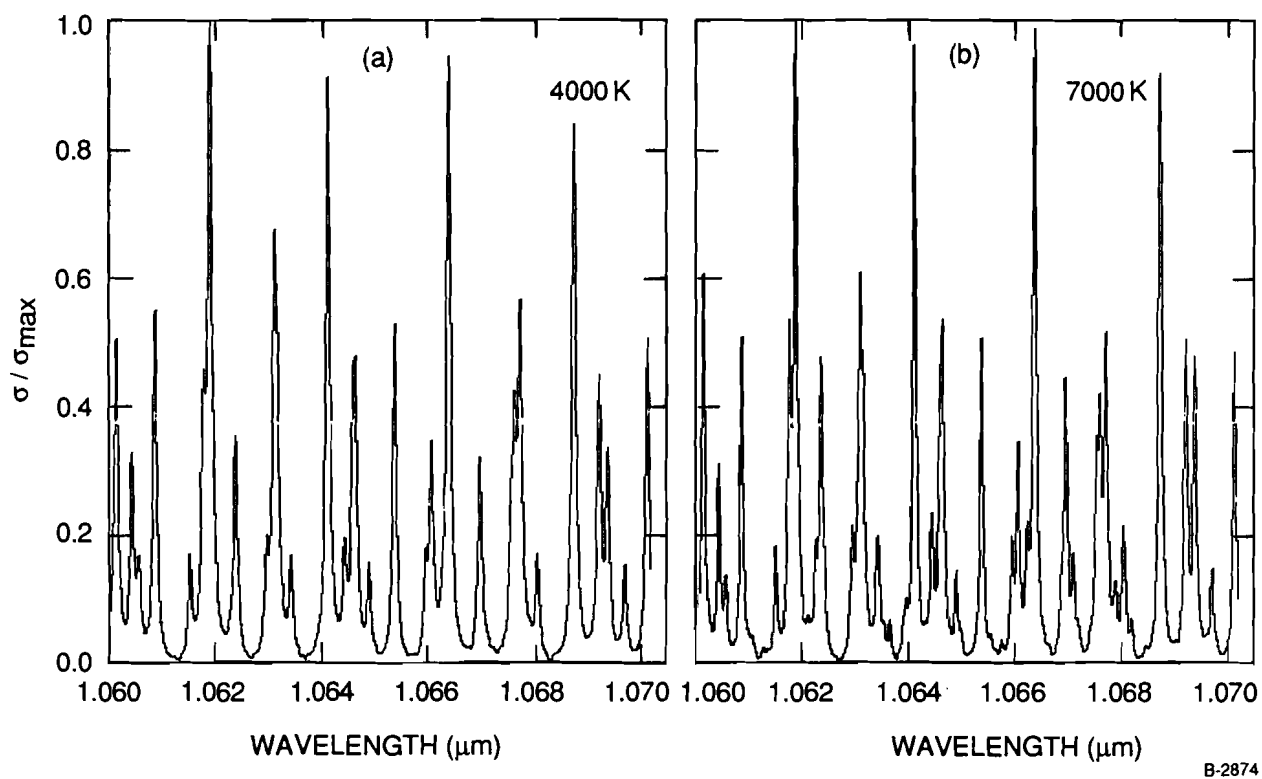
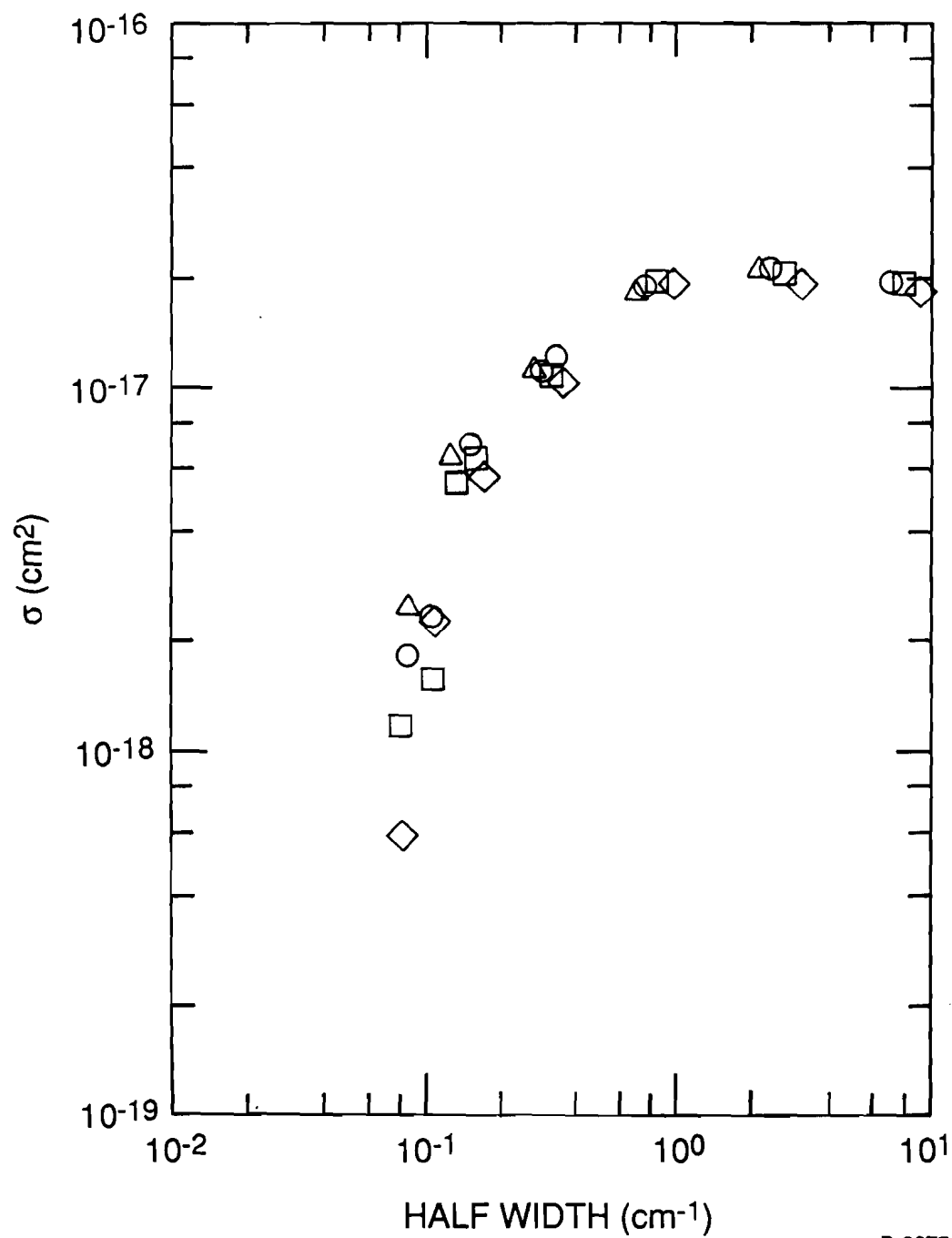


Figure 35.

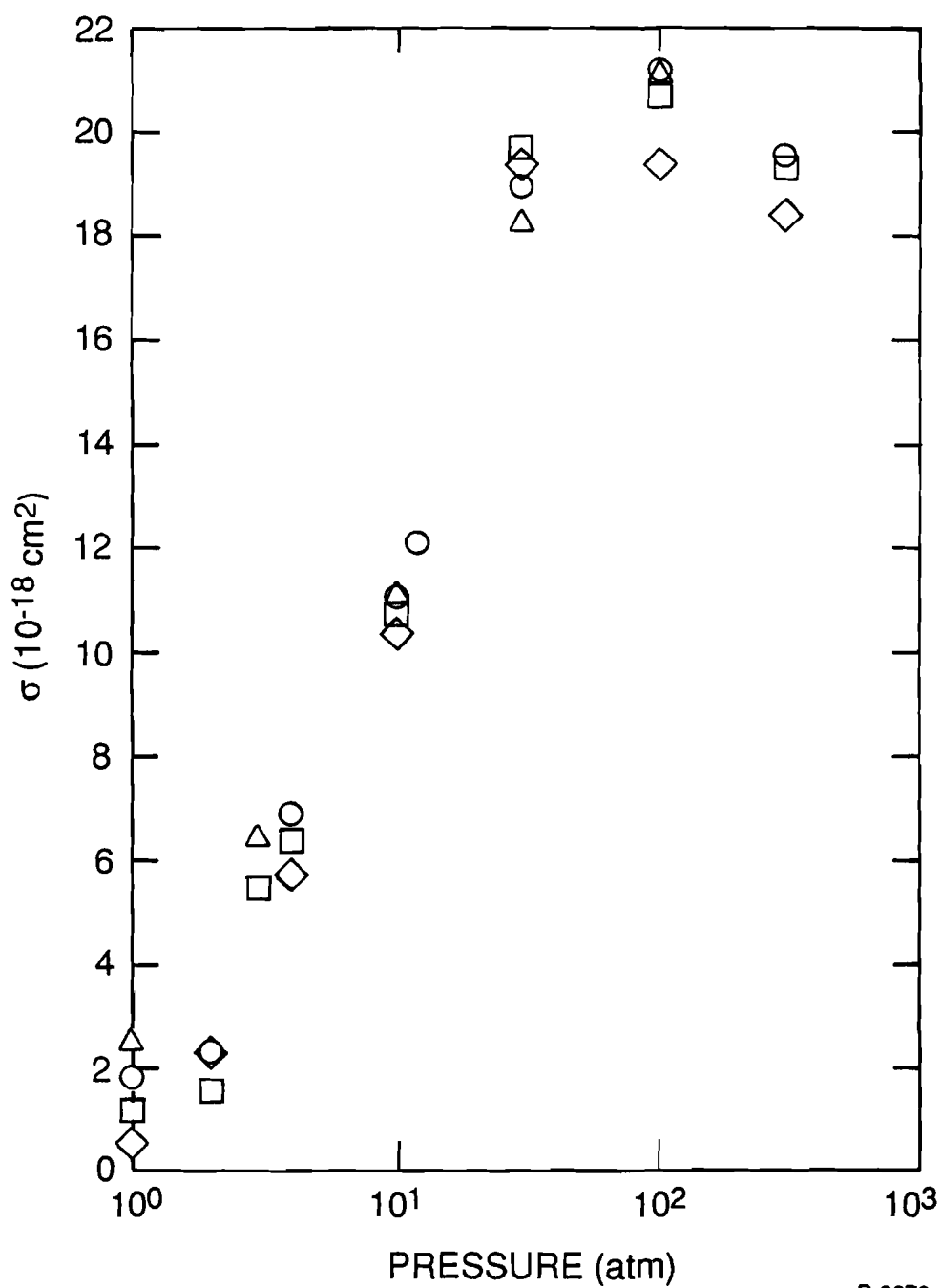
Effect of Temperature on the Absorption Spectrum Calculated for $C_2 X(^1\Sigma_g^+)$ to $A(^1\Pi_u)$ from 1.06 to 1.07 μm at $p = 10$ atm. In parts (a) and (b), the temperature is 4000 and 7000 K, $\gamma_D + \gamma_L$ is 0.359 and 0.275 cm^{-1} , and σ_{max} is 1.19 and 1.28×10^{-16} cm^2 , respectively.



B-2875

Figure 36.

Effect of Line Half Width ($\gamma_D + \gamma_L$) on the Absorption Cross Section Calculated at $1.064 \mu\text{m}$ for $\text{C}_2 \text{ X}(^1\Sigma_g^+)$ to $\text{A}(^1\Pi_u)$. The diamonds, squares, ovals, and triangles represent $T \approx 4000, 5000, 6000,$ and 7000 K, respectively.



B-2876

Figure 37.

Effect of Pressure on the Absorption Cross Section Calculated at 1.064 μm for $\text{C}_2 \text{ X}(^1\text{E}_g^+) \text{ to } \text{A}(^1\Pi_u)$. The diamonds, squares, ovals, and triangles represent $T = 4000, 5000, 6000, \text{ and } 7000 \text{ K}$, respectively.

for absorption to the lowest excited singlet state $A(^1\Pi_u)$, whose excitation energy from the ground state, $v''=0$ level, is $24,676\text{ cm}^{-1}$ (3.06 eV, or $0.405\text{ }\mu\text{m}$). This comparison failed to include the absorption data of Cooper and Jones (1979), who show that the transition extends out to at least $0.53\text{ }\mu\text{m}$ when the temperature is 3238 K. Figure 38 compares the data of Cooper and Jones at three temperatures with the Brewer and Engelke data that we converted to σ values by using the vapor pressure data of Leider and coworkers (1973). The comparison shows good agreement between the two experiments at the maximum of the absorption, and the Cooper and Jones data falls off faster at low energies. Note that the Cooper and Jones data at different temperatures show a higher maximum at lower temperatures, and higher low-energy wings at higher T. This is consistent with the expectation that the absorption will spread over a greater energy range as T increases and that the total oscillator strength for the transition is conserved. Thus a constant area under the σ -E curve is spread over a larger energy range as T increases.

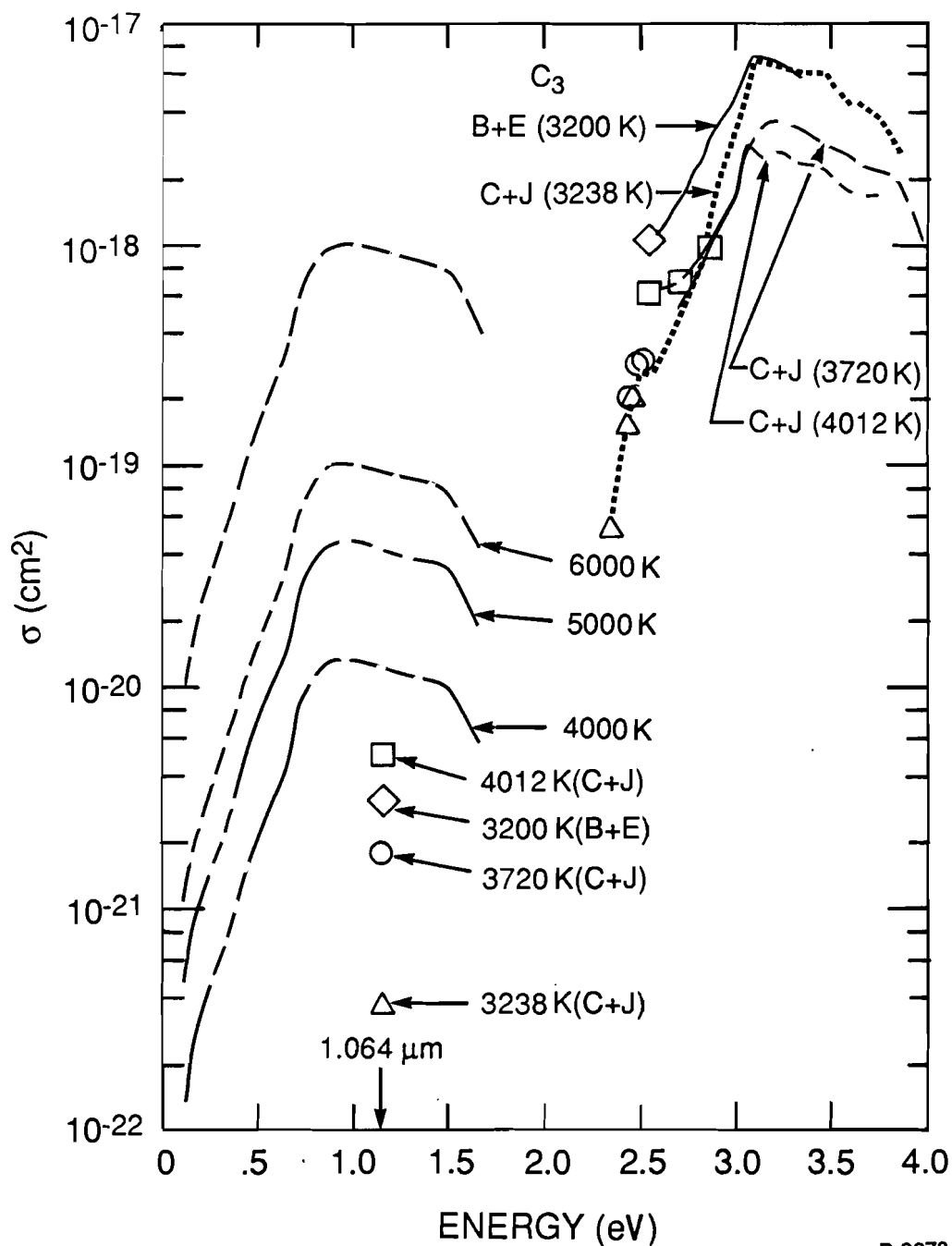
Figure 38 also shows extrapolations of the data to $1.064\text{ }\mu\text{m}$ (1.165 eV) under the assumptions that the transition moment R_e and the Franck-Condon factors are all constant, so that the dependence on photon energy E is simply

$$\sigma(E) = \sigma(E_0) (E/E_0) \exp[-(E_0 - E)/(k_B T)] \quad , \quad (27)$$

where E_0 is the photon energy at the last measured value, k_B is the Boltzmann constant, and T is the temperature. The figure shows symbols plotted at the lowest reported energies, and the same symbol at 1.165 eV represents the extrapolation based on the lowest-energy experimental point at that temperature. The figure shows that the measured fall-offs have similar slopes from the maxima to the lower energy points as the slope between the last

measured point and 1.165 eV, which is given by Eq. (27). This means that the Franck-Condon factors are roughly constant over the energy range from about 2.4 to 3.1 eV. However, we have no evidence that the factors remain constant for the remainder of the extrapolation to 1.165 eV. As discussed previously (Simons et al., 1989), it is quite possible that the vertical transitions between the potential curves have a larger separation than 1.165 eV, which would mean that the absorption would have to be a non-vertical transition with a small Franck-Condon factor. Thus the extrapolations should be considered to give upper limits to the σ value at 1.064 μm .

Figure 38 also shows an estimate for the absorption resulting from transitions between the two lowest triplet states. The first electronically excited state of C_3 is a triplet state, $a(^3\Pi_u)$, which is observed at 2.12 eV in a Ne matrix (Jacox, 1988), a value that would correspond to about 2.10 eV in the gas. This state can be thermally populated at high temperatures in the plume. For example, the degeneracy times the Boltzmann factor is 0.013, 0.044, and 0.10 at $T = 4000, 5000, \text{ and } 6000 \text{ K}$, respectively. The next excited triplet state is the $^3\Pi_g$ level that has an excitation energy relative to the lowest triplet predicted to be 0.71 to 0.81 eV (Römel't, et al., 1978), 0.93 eV (Williams, 1975), or 0.74 eV (Jones, 1985). Thus, there is an allowed transition predicted to be accessible from the lowest triplet state. The oscillator strengths for the triplet transitions are not available, but we would expect the maximum σ values to be in the range of 10^{-19} to 10^{-17} cm^{-2} . In the figure, we have estimated σ at $T = 4000, 5000, \text{ and } 6000 \text{ K}$ by assuming that the square of the transition moment R_e^2 and the Franck-Condon factors are the same as they are for the $X(^1\Sigma_g^+) \text{ to } A(^1\Pi_u)$ transition. What we plot is the



B-2878

Figure 38.

Absorption Spectrum of C_3 . The high energy region shows data at 3200 K (Brewer and Engelke, 1962), adjusted to use vapor pressures of Leider et al. (1973), and data at $T = 3238, 3720$, and 4012 K (Cooper and Jones, 1979). These measurements are extrapolated to give the points shown at 1.165 eV (see text). Also shown is an estimate of the low-energy triplet transition, $a(^3\Pi_u)$ to $b(^3\Pi_g)$ for $T = 4000, 5000$, and 6000 K. The top curve shows the corresponding σ values if the $a(^3\Pi_u)$ state were the ground state.

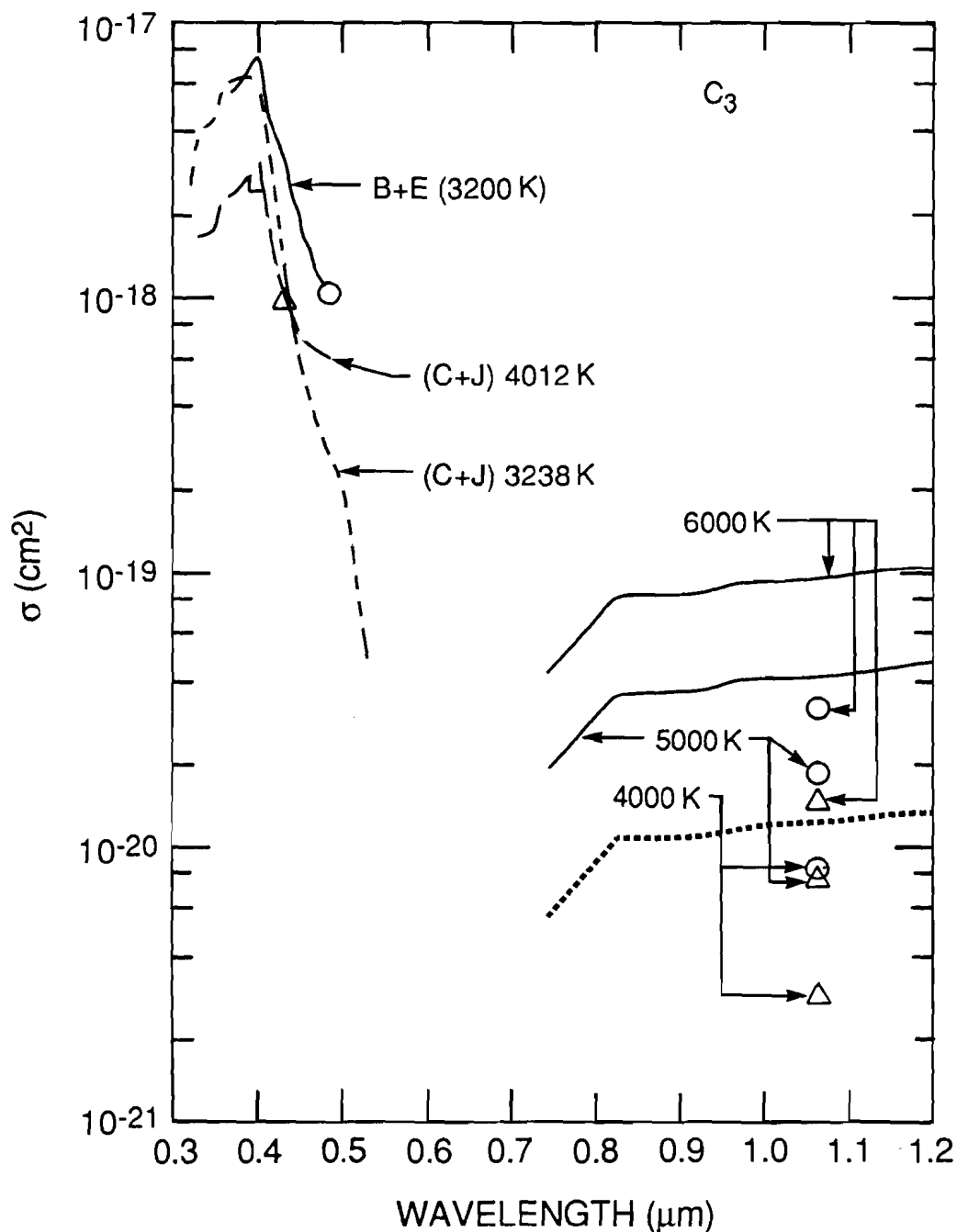
Cooper and Jones (1979) σ_{CJ} data at 3720 K adjusted using Eq. (27) and the thermal population of the $a(^3\Pi_u)$ state to give

$$\sigma_3(E) = \sigma_{CJ}(E + 0.74)[E/(E + 0.74)]g_3 \exp(-2.12/Te) \quad , \quad (28)$$

where g_3 is the degeneracy factor of six. The upper curve shows what σ would be if the $a(^3\Pi_u)$ state were the ground state (i.e., the $g_3 \exp(-2.12/Te)$ term is set to unity). This shows a maximum σ of 10^{-18} cm^2 , which is a reasonable value. It is possible that the the a to b transition will have sharp structure, so that σ at the laser line could be a small value between the transitions. The fact that the lowest singlet transition is a pseudocontinuum at $T = 3200 \text{ K}$, argues that the triplet excitation will also be pseudocontinua at high T , although the lowest frequency vibration for the a state is predicted to be larger than that for the ground state, which will spread the line spacing. At higher pressures, the absorption will become a pseudocontinuum in the same way as we saw above for C_2 . Figure 39 shows data from Figure 38 in a plot versus wavelength. Here the X to A $\sigma(1.064 \text{ }\mu\text{m})$ values using Eq. (27) to extrapolate the data from the two experimental groups are shown at $T = 4000$, 5000 , and 6000 K , with the experimental point used in the extrapolation shown with the same symbol as the extrapolated points.

3.2.6 Absorption Spectra of Other Plume Species

In graphite epoxy and Kevlar epoxy targets, the C_2H radical is an important species in absorbing $1.06\text{-}\mu\text{m}$ radiation. It has a low-energy electronic transition from the $X(^2\Sigma^+)$ to the $A(^2\Pi)$ state, with a transition energy predicted to be around 0.5 eV (Shih, et al., 1977, 1979), and the band at 0.446 eV has been tentatively identified as the origin (Yan, et al., 1987). This is a triatomic radical with a low-frequency bend, which leads to the



B-2879

Figure 39.

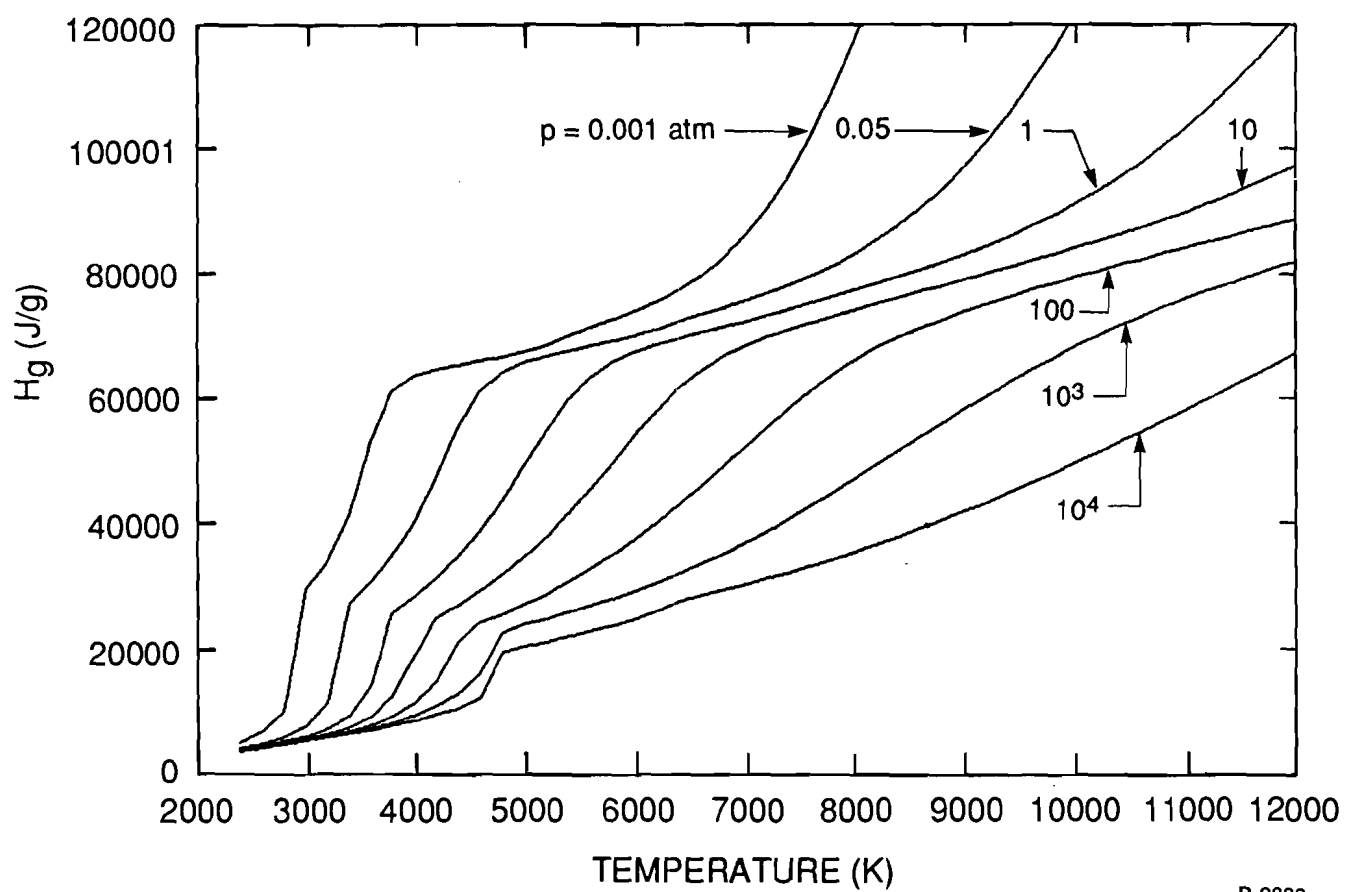
Absorption Spectrum of C_3 . The high energy region shows data from Brewer and Engelke (1962) at 3200 K and the $T = 3238$ and 4012 K data of Cooper and Jones (1979). The ovals and the triangles represent extrapolations from the measured data (at the λ shown by the point) to the points shown at 1.064 μm for $T = 4000$, 5000, and 6000 K (see text). Also shown is an estimate of the lowest triplet transition, $a(^3\Pi_u)$ to $b(^3\Pi_g)$ for $T = 4000$, 5000, and 6000 K.

expectation that absorption will be a pseudocontinuum at higher temperatures, especially when the pressure is large enough to substantially broaden the lines. Reimers and coworkers (1985) have calculated the absorption spectrum at 3000 K. The maximum absorption of $\sigma = 3 \times 10^{-19} \text{ cm}^2$ is near $1.064 \text{ }\mu\text{m}$.

The C_3H and C_4H radicals are also important species in the plume from graphite epoxy targets. It is reasonable that these will also have sizable σ values at $1.06 \text{ }\mu\text{m}$, as these will have at least one low frequency vibration, which implies the absorption spectrum will contain pseudocontinua at high temperatures. In addition, there are several diatomic species that are important in ablation plumes, and the absorption spectra for these should be calculated in the manner described above for C_2 .

3.2.7 Equilibrium Calculation of Significant Species in the Ablation Plume

At the high gas pressures that exist near the surface of a target that is rapidly ablating, it is reasonable to assume that the reaction rates are fast enough that the species are at chemical equilibrium, especially when we consider the high temperatures in the region. The equilibrium values we use are calculated in the same way as earlier calculations at PSI (Simons, et al., 1989, Appendix A), except that we have included more species. In particular, we have included ionic species, so that the enthalpy continues to increase with T , even when there are essentially no molecular species left. This is shown in Figure 40, which gives H_g as a function of T for pressures from 10^{-3} to 10^4 atm for a graphite epoxy target. The relative species concentrations for this material are shown as a function of the temperature in Figures 41 and 42 for pressures of 10 and 1000 atm, respectively. These show that molecular species are important up to higher temperatures when the pressure is higher. At high



B-2880

Figure 40.

Enthalpy per Gram of the Equilibrium Gas Mixture That Has the Elemental Composition of Graphite Epoxy at Different Pressures as Functions of Temperature

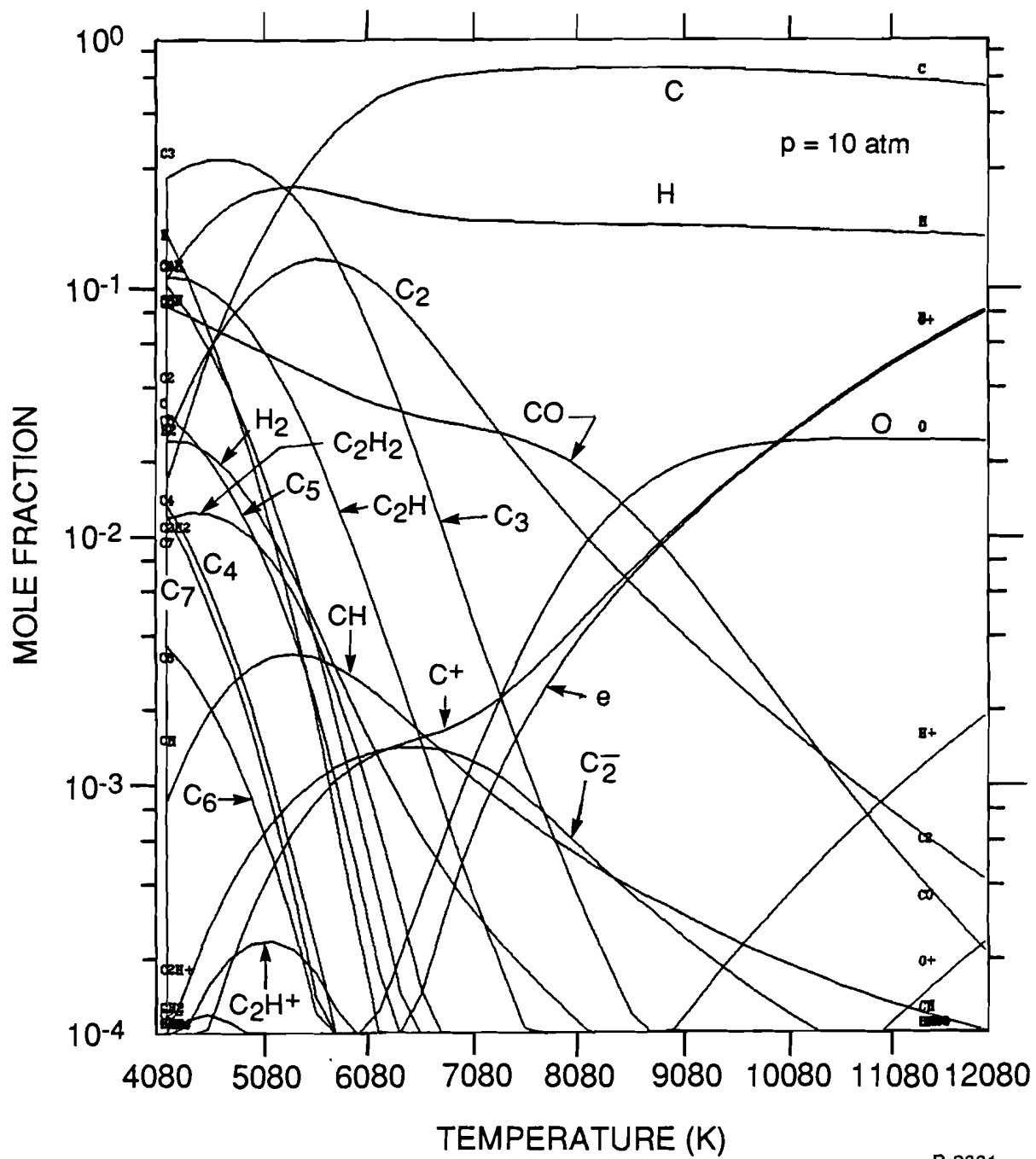
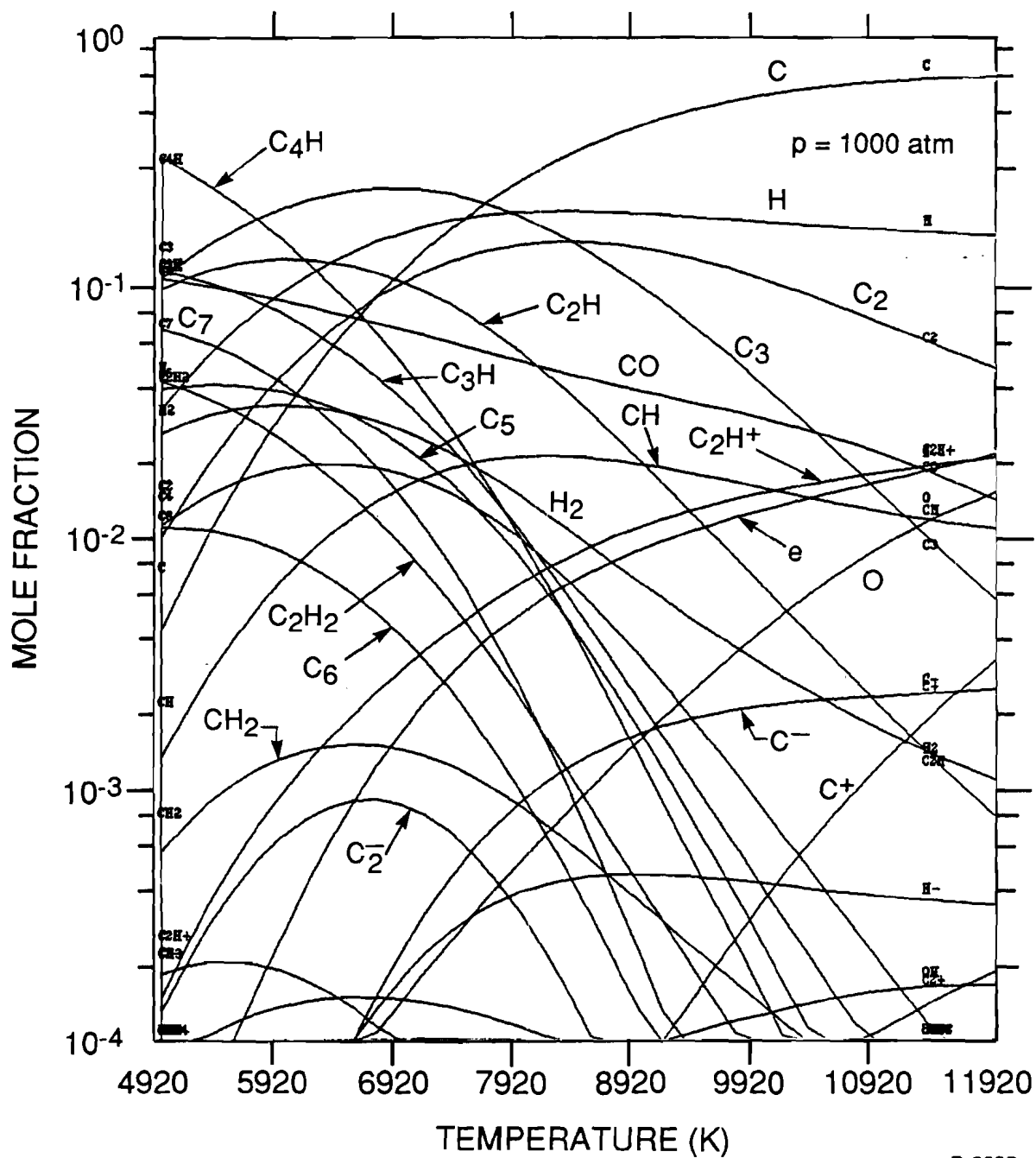


Figure 41.

Mole Fractions of Species in the Equilibrium Gas Mixture That Has the Elemental Composition of Graphite Epoxy at $p = 10 \text{ atm}$ as Functions of Temperature



B-2882

Figure 42.

Mole Fractions of Species in the Equilibrium Gas Mixture That Has the Elemental Composition of Graphite Epoxy at $p = 1000 \text{ atm}$ as Functions of Temperature

pressures the important molecular species are C_4H , C_3 , C_2H , and C_2 ; also, CO , C_3H , C_4 , C_5 , C_6 , C_7 , CH , H_2 , C_2H^+ , and C_2H_2 are present with $x_i > 0.01$ for some temperature region. The equilibrium calculations depend on the thermochemical values used as input. The results presented here use values that are primarily from the JANAF tables (Chase et al., 1985), as discussed previously (Simons, et al., 1989, Appendix A). The major features of the results are similar when we use a thermochemical data set developed for combustion studies at Sandia National Laboratory (Miller and Bowman, 1988). This data set is a revision of one developed by NASA workers (see Burcat, 1984).

4. REFERENCES

- Brewer, L. and Engelke, J.L. (1962), "Spectrum of C_3 ," J. Chem. Phys., 36, 992-8.
- Brewer, L. and Hagen, L. (1979), High Temp. Sci., 11, 233.
- Burcat, A. (1984), "Thermochemical Data for Combustion Calculations," Chapter 8 in Combustion Chemistry (Springer-Verlag, New York), edited by W.C. Gardiner, pp. 455-504.
- Chase, Davies, Downey, Frurip, McDonald, and Syverud (1985), Thermochemical Tables (National Bureau of Standards, Third Edition).
- Cooper, D.M. and Jones, J.J. (1979), J. Quant. Spectrosc. Radiat. Transfer, 22, 201.
- Cooper, D.M., and Nicholls, R.W. (1976), Spectrosc. Lett., 9, 139.
- Eccles, J., and Malik, R. (1981), Quantum Chem. Prog. Exch. Bull., 13, 407.
- Geltman, S. (1973), J. Quant. Spectrosc. Radiat. Transfer, 13, 601.
- Gustafson, P.R. (1986), "An Evaluation of the Thermodynamic Properties and the P, T Phase Diagram of Carbon," Carbon, 24, 169-176.
- Herzberg, G. (1950), Molecular Spectra and Molecular Structure I. Spectra of Diatomic Molecules (Van Nostrand, Princeton).
- Huber, K.P., and Herzberg, G. (1979), Molecular Spectra and Molecular Structure IV. Constants of Diatomic Molecules (Van Nostrand Reinhold, New York).
- Hulbert, H.M., and Hirschfelder, J.O. (1961), J. Chem. Phys., 35, 1901.
- Jacox, M.E. (1988), "Electronic Energy Levels of Small Polyatomic Transient Molecules," J. Phys. Chem. Ref. Data, 17, 269-511.

- Jones, R.O. (1985), "Energy Surfaces of Low-Lying States of C_3 ," J. Chem. Phys., 82, 5078-82.
- Karzas, W.J. and Latter, R. (1961-62), Astrophys. J. Suppl. Ser., 6, 167.
- Lee, E.L. and Sanborn, R.H. (1973), "Extended and Improved Thermal Functions for the Gaseous Carbon Species C_1 - C_7 from 298 to 10,000°K," High Temp. Sci., 5, 438-453.
- Leider, H.R., Krikorian, O.H., and Young, D.A. (1973), "Thermodynamic Properties of Carbon Up to the Critical Point," Carbon, 11, 555-563.
- Marinelli, W.J., and Piper, L.G. (1985), J. Quant. Spectrosc. Radiat. Transfer, 34, 121.
- Miller, J.A., and Bowman, C.T. (1988), "Mechanism and Modeling of Nitrogen Chemistry in Combustion," Sandia Report WSS/CI88-63, Sandia National Laboratory, Livermore, CA.
- Peric-Radic, J., Römelt, J., Peyerimhoff, S.D., and Buenker, R.J. (1977), "Configuration Interaction Calculation of the Potential Curves for the C_3 Molecule in Its Ground and Lowest-Lying Π_u States," Chem. Phys. Lett., 50, 344-50.
- Reimers, J.R., Wilson, K.R., Heller, E.J., and Langhoff, S.R. (1985), "CASSCF-Wave Packet Ab Initio Prediction of Electronic and Vibrational Spectra: Application to the $A(^2\Pi) \leftarrow X(^2\Sigma^+)$ Absorption of C_2H at 3000 K," J. Chem. Phys., 82, 5064-77.
- Resendes, D. (1987), Thermochemical Properties of Ablative Composites, Physical Sciences Inc., PSI-TR-791.

- Römel't, J., Peyerimhoff, S.D., and Buenker, R.J. (1978), "Ab Initio MRD CI Calculations for the Electron Spectrum of the C_3 Radical," Chem. Phys. Lett., 58, 1-7.
- Schadee, A. (1978), J. Quant. Spectrosc. Radiat. Transfer, 19, 451.
- Shih, S., Peyerimhoff, S.D. and Buenker, R.J. (1977), "Theoretical Prediction of the Vertical Electronic Spectrum of the C_2H Radical," J. Mol. Spec., 64, 167-79.
- Shih, S., Peyerimhoff, S.D., and Buenker, R.J. (1979), "Calculated Potential Surfaces for the Description of the Emission Spectrum of the C_2H Radical," J. Mol. Spec., 74, 124-35.
- Simons, G.A., Nebolsine, P.E., Chen, J., Person, J.C., Weyl, G., Resendes, D., Bailey, A., and Humer, N.D., Free Electron Laser Simulation Program, PSI-TR-900, April 1989.
- Svehla, R.A. (1962), "Estimated Viscosities and Thermal Conductivities of Gases at High Temperatures," NASA TR R-132, Lewis Research Center.
- Tellinghuisen, J. (1974), Comput. Phys. Commun., 6, 221.
- Whiting, E.E., Schadee, A., Tatum, J.B., Hougen, J.T., and Nicholls, R.W. (1980), J. Molec. Spectrosc., 80, 249.
- Williams, G.R.J. (1975), "The C_3 Radical: A Theoretical Study of the Electronic Spectrum of C_3 via the Equations of Motion Method," Chem. Phys. Lett., 33, 582-4.
- Yan, W.-B., Dane, C.B., Zietz, D., Hall, J.L., and Curl, R.F. (1987), "Color Center Laser Spectroscopy of C_2H and C_2D ," J. Mol. Spec., 123, 486-95.